RADIATION-INDUCED CONDENSATIONAL GROWTH OF CLOUD-SIZED MIST DROPLETS

BY

XINCHANG LI

THESIS

Submitted in partial fulfillment of the requirements
for the degree of Master of Science in Civil Engineering
in the Graduate College of the
University of Illinois at Urbana-Champaign, 2019

Urbana, Illinois

Advisers:

Professor M. Quinn Brewster
Professor Mark J. Rood

ABSTRACT

Many uncertainties still exist regarding cloud droplet evolution and the production of precipitation from clouds, including the effects of both shortwave and longwave (infrared) thermal radiation. The potential importance of infrared thermal radiation on cloud droplet evolution, particularly at cloud top, has been known in theory for over a century. Yet, despite Osborne Reynolds' pioneering 1877 conceptual observation in this regard, very little laboratory experimental investigation of the phenomenon has been reported. A few theoretical studies in recent decades have followed up on Reynolds' idea and shown with detailed model calculations that net radiative cooling can induce rapid condensational growth of larger droplets at the expense of evaporating smaller ones. However, a gap still exists in the literature between model predictions and experimental evidence.

In this study, both laboratory experiments and computational modeling were done to investigate the effect of radiative cooling on cloud-sized water mist droplet evolution. The experiments were a continuation from two earlier students' graduate research projects. Improvements were made on the experimental apparatus from this previous work to solve issues regarding unrepresentative droplet sizes and gravitation settling, and thereby better satisfy modeling assumptions. Experimental measurements were then conducted under both isothermal wall and conductively-adiabatic wall conditions. The results showed that with the mist initially at 20 ℃ and 3.5 ppm volume concentration being cooled by a -20 ℃ radiative sink, the D_{43} mean droplet diameter grew from 6.0 to 7.3 μm and from 5.5 to 8.4 μm after 80 s of radiative cooling under isothermal and conductively-adiabatic wall conditions, respectively. This represents a larger relative amount of growth in the adiabatic-wall case (52%) than in the isothermal-wall

case (21%) for the same radiative sink temperature due to an absence of heat conduction from the wall that was mitigating the radiative cooling effect in the isothermal case.

Two computational models were also developed to study the conductively-adiabatic wall experiments. One model solves the fully coupled mass and energy balance equations with unsteady water vapor mass balance using Engineering Equation Solver (i.e., the exact model), and the other invokes the quasi-steady water vapor mass assumption to reduce system complexity and uses MATLAB (i.e., the approximate model). Results from the two models showed less than 0.03% differences between each other in predicting mist droplet size distributions, temperature and supersaturation profiles, thus confirming the validity of the quasi-steady water vapor assumption used in the approximate model. A parametric study was done with the approximate model to investigate mist droplet evolution without and with external thermal effects. It was demonstrated that droplets go through a process of internal equilibration even when no thermal radiation is exchanged between the mist and the surroundings, which causes the droplets to become more monodispersed towards larger diameters. Higher temperatures enhance the rate of this equilibration process through increased water vapor pressure that increases overall rate of condensation and evaporation. When an external factor such as radiative cooling is imposed, the droplets go through both internal and external equilibrations. Radiative cooling markedly promotes the growth rate of larger droplets during external equilibration, which process continues until the mist is cooled close to the radiative sink temperature, and internal equilibration begins to dominate. The mist droplet volume concentration can play an important role in regulating the mist's sensitivity to external equilibration. Thinner mist (smaller droplet volume concentration) with stronger radiative heat

loss would experience more effective external equilibration and more radiative-augmented growth in large droplets.

In comparing model predictions with experimental measurements, the models predicted the mist temperature to drop from 20 to 2.9°C after 80 s of radiative cooling, matching measurements from the experiments. In terms of droplet size distribution, the models predicted the D_{43} mean diameter to grow from 5.5 to 10.6 μm as compared with the measured 8.4 μm after cooling. This difference in D_{43} corresponds to differences in the distribution that appear primarily in the smallest and largest droplets. Measurements showed that droplets smaller than 2.5 μm in diameter were being preserved after radiative cooling, which were shown to have evaporated in the models. The experiments also indicated more growth in larger droplets than was predicted by the models. These discrepancies are consistent with room aerosol activation and droplet growth by coagulation, which were not included in the models.

In conclusion, this study has shown through laboratory experimental measurements and computational modeling that radiative cooling under realistic conditions can augment cloud-sized mist droplet growth. This result is important as it helps explain aspects of cloud physics that are still uncertain such as how cloud droplets pass through the condensation-coalescence bottleneck.

ACKNOWLEDGEMENTS

I would like to express my profound gratitude to my advisers, Professor M. Quinn Brewster and Professor Mark J. Rood, for their patient guidance, generous support and valuable critiques throughout the completion of my thesis project. In particular, I wish to thank Professor Brewster for always having faith in me and helping me through hard times, and Professor Rood for motivating me to stay on schedule and keep up the quality of my work. My gratitude also extends to Dr. Nicole Riemer in Atmospheric Sciences who helped troubleshoot my experiments, to Ezra O. McNichols and Kibria. K. Roman, the two previous students for their contributions to this research, and to my groupmate Jong Woo Kim for his kind help in my times of need.

My appreciation also goes to CEE staff Ms. Joan E. Christian, Ms. Marvis A. Orzek and Dr. Shaoying Qi for their managerial support in completing this project, and MechSE staff Ms. Laurie Macadam, Ms. Kathy Smith and their colleagues for their help in assistantship and business administration, and many technicians from MechSE laboratory and IT Help Desk for their technical assistance.

I also wish to thank my parents for their constant support and encouragement without which I would not have been here, and Rajeev for bringing so much joy to my life.

Finally, I gratefully acknowledge the following funding sources for their support in my research and conference attendance: U.S. National Science Foundation (Grant Number 1062361, PI: M. Q. Brewster), H. G. Soo Professorship (M. Q. Brewster), Racheff Student Travel Award from CEE and Graduate Student Travel Award from the Graduate College.

To Mom and Dad

To Obstacles, Persistence, Courage and Friendship

TABLE OF CONTENTS

CHAPTER 1: INTRODUCTION

Radiation from the sun drives the climate of the Earth. Solar energy mobilizes the water cycle by evaporating surface water into the atmosphere, which cools and condenses to form clouds and eventually returns to the earth in the form of precipitation [1]. As qualitatively described in the Fifth Assessment Report (AR5) of the Intergovernmental Panel on Climate Change (IPCC) [2], radiative forcing involving cloud and radiation interactions are of medium to low confidence level, therefore, understanding cloud processes and their interactions with radiation will benefit our understanding towards climate. Clouds regulate the incoming shortwave (SW) and the outgoing longwave (LW) radiation resulting in positive or negative forcing on Earth's climate [3]. On the other hand, radiation as a heat transfer mechanism affects the microphysical processes in clouds. SW solar radiation can supply heat and evaporate cloud droplets, while LW cooling can counteract the effect by promoting condensational droplet growth [4]–[6]. This study explores the effect of net radiative cooling on droplet growth in producing large droplets that could initiate the collision-coalescence process in clouds [7] which will be the emphasis of the following discussion.

1.1 Literature review

The effect of thermal radiation on cloud droplets have been noticed for over a century. Reynolds [8] was the first to point out in 1877 that the temperature difference induced by radiation is of the same magnitude as that induced by conduction or condensation, especially for top-of-cloud droplets where the effective environmental radiating temperature could be much lower than the cloud temperature. Albeit an important observation, which has been referred to as

the Reynolds effect by some, it was largely ignored for decades. Fuchs [9] appears to be the first to include the radiation term in the vapor growth equation. He focused his discussion on the interior of the clouds where the water droplet was considered as a blackbody with a correction constant α, which he deemed slightly smaller than unity but did not give an exact value. He concluded that since the temperature difference between the droplet and the surrounding is negligible, the radiative effect for droplet growth from vapor could also be neglected for droplets with diameter on the order of a few 100's μm or less. Roach [10] and Barkstrom [11] rediscovered the fact that droplets residing at cloud top may experience a much larger radiative heat flux than cloud droplets residing in the interior of the cloud and studied the radiation effect on an isolated top-of-cloud (or top-of-fog) droplet. Both showed through model calculations that radiation can speed up the droplet growth rate by as much as 20 times that of condensation without radiation, and larger droplets (on the order of 10's of μm in diameter) could grow through radiative cooling even under subsaturation.

In the meantime, the atmospheric science community has been puzzled by the unexplained fast growth of rain drop embryos (typically droplets of 100's-μm diameter). Observations show that this process can take only 15 - 20 min, while existing theories predict that the duration of the time interval required for droplets to grow up to 100 μm in diameter is of the order of hours [12]. The phenomenon is known as the "condensation-coalescence bottleneck", which describes the absence of a mechanism to explain liquid droplet growth between stable cloud size, roughly 20 μm diameter, where growth by condensation dies down, and the size where growth by coalescence can take over, at roughly 80 μm [13]. Different mechanisms have been postulated, such as turbulent mixing and radiation-assisted growth. While the former has been well studied [12], limited attention has been given to radiative enhancement

of droplet growth. Guzzi and Rizzi [14] showed that longwave cooling allows large droplets to grow while suppressing the growth of smaller droplets. Such differentiating effect on the droplet size spectrum could potentially augment the collision-coalescence among droplets. Austin et al. [15] investigated with a one-dimensioned model the combined effect of radiation and collision-coalescence, and demonstrated that the time required for the onset of precipitation may be reduced by as much as a factor of 4. Harrington et al. [7] expanded on the dimension and complexity of modeling, and showed when droplets reside near the top of fogs, stratus or stratocumulus clouds for 12 minutes or longer, larger droplets are favored by radiative enhancement and can grow rapidly at the expense of evaporating smaller droplets. They showed that the radiative effect reduces the time required for the onset of drizzle by up to one half hour. Hartman and Harrington [4], [5] continued the work by including SW heating into the radiative transfer analysis. The results showed that SW heating partially offsets cloud-top LW cooling, which naturally reduces the influence of LW cooling on drop growth, but SW heating dominates over LW cooling only at larger droplet sizes (diameter $\gtrsim 400$ μm).

Despite these theoretical studies, there are no peer-reviewed publications comparing experimental with theoretical results describing the process of radiative cooling of cloud/mist droplets. Before the author worked on this project, two other students had completed their thesis/dissertation making progress on the study. Their work is discussed in detail in the following section.

1.2 Precedent work

Roman [16] and McNichols [17] worked on the project in sequence and set ground for the experimental work of this study. Roman first developed the original apparatus as shown in

Figure 1. Mist from a commercial ultrasonic humidifier is supplied from the left and is diluted with air flow. W1, W2 and W3 are three sets of optical windows where droplet size distribution data could be obtained using a laser diffraction system (which will be introduced in section 2.3). The mist flows through the precooling section (between W1 and W2), where it was assumed to be straightened to laminar flow by two sets of flow straighteners, and enters the radiative cooling section (between W2 and W3). The components in the radiative cooling section are mostly preserved by the author in her experiments and will be discussed in section 2.2.

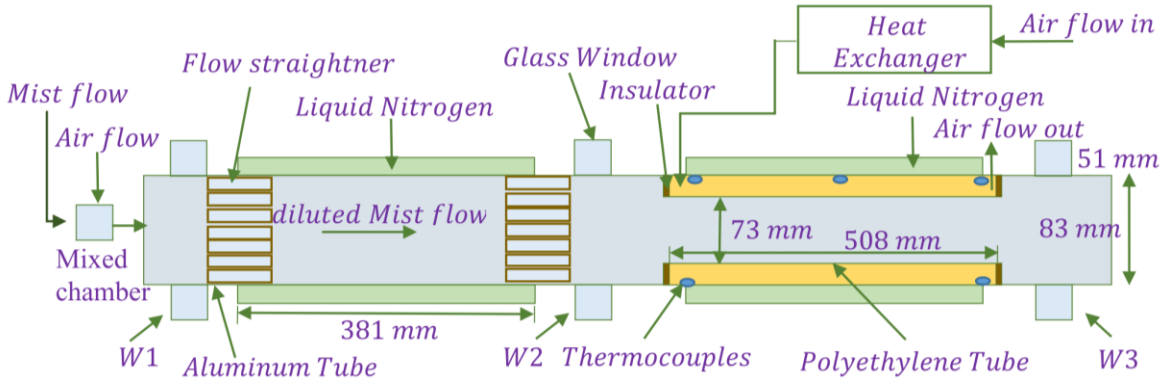

Figure 1. Original apparatus developed by Roman (Fig. 3.1 in [16]).

The precooling section was deemed necessary because of the size of the droplets produced by the ultrasonic humidifiers. The operating principle of an ultrasonic humidifier is illustrated in Figure 2 [18]. A piezoelectric ceramic transducer is submerged under water. When in operation, high frequency oscillating current is fed into the transducer causing it to vibrate. The water surface is shattered by the input energy into fine droplets, which are carried to the outlet by the air stream from a small fan. The size of the droplets decreases as the frequency of the transducer increases [18]. The ultrasonic frequency for the humidifiers used was 1.6 MHz, and the droplet size distribution as reported by Roman is shown in Figure 3a, with the majority of droplets having diameters < 5 μm. However, the diameters were thought to be too small (not

having long enough pathlength, i.e. not opaque enough) for effective radiative cooling, and to better represent droplet sizes in clouds the diameter of mist droplets needs to be bigger, about 10's of μm. To produce droplets of this size, Roman employed the precooling zone to cool and grow the droplets to the desired size by primarily convective cooling to promote condensational growth on the droplets. The droplet size distribution after the precooling section is shown in Figure 3b.

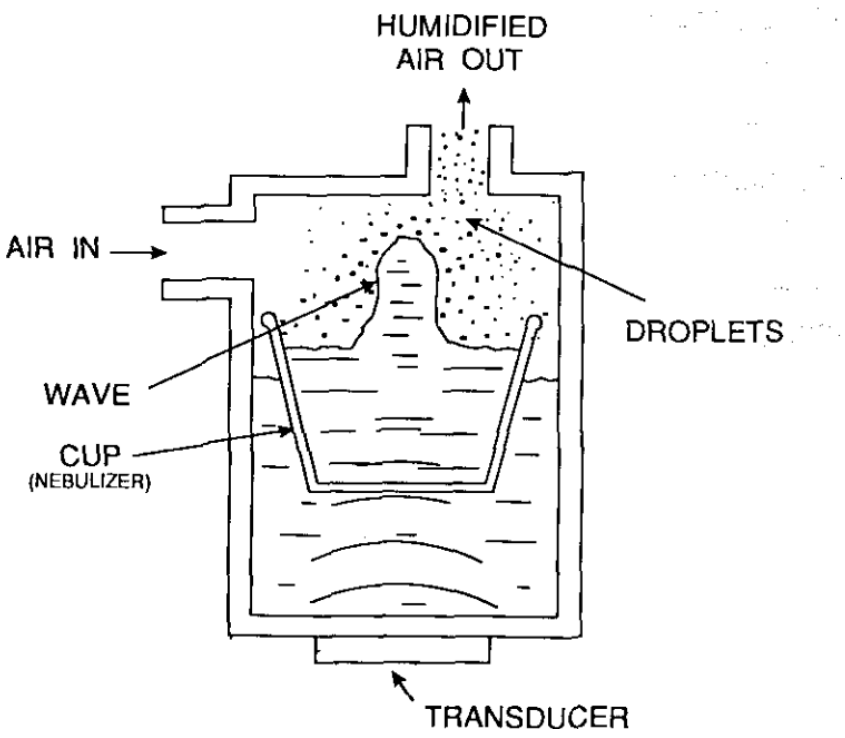

Figure 2. Operating principle of an ultrasonic humidifier (FIGURE 1 in [18]).

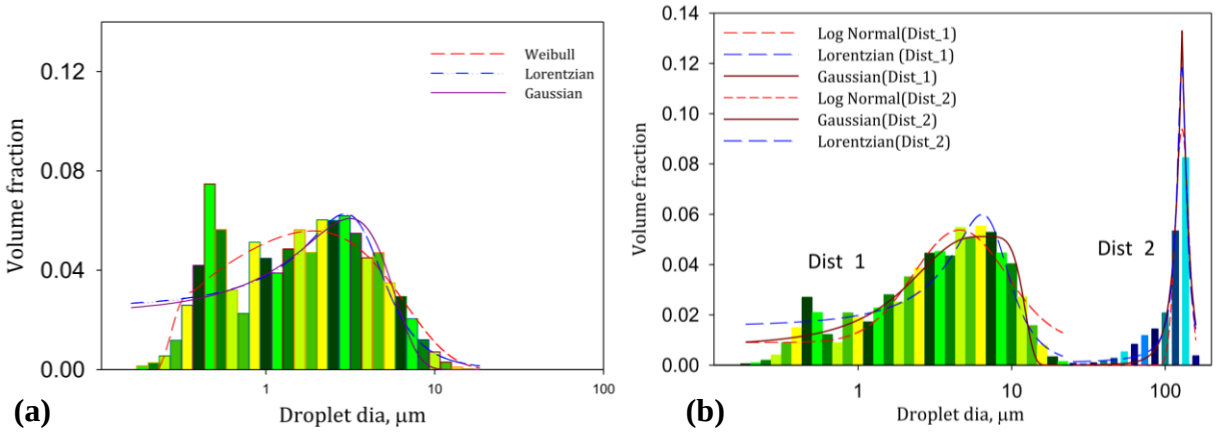

Figure 3. Droplet size distribution (a) directly from commercial ultrasonic humidifier, and (b) after precooling section (Fig. 3.5 and 3.6 in [16]).
(Note: Roman discussed possible droplet size distribution functions in his dissertation, hence the legends; however, since they are out of scope of this thesis they will not be discussed).

One problem Roman had with the apparatus, however, was the production of 100's µm diameter droplets observed at W2 which could not be properly explained. Having droplets as large as 100 µm in diameter was undesired as growth by coalescence can dominate in this regime, overshadowing the effect of radiation-induced growth. McNichols suspected that condensate was forming on the walls of flow straighteners, and the big droplets were entrained as the mist stream passed through. In order to eliminate these droplets, anti-condensation spray was applied to the flow straighteners. It worked reportedly in eliminating the 100's µm mode Roman used to have after the precooling section (Figure 4), and anti-condensation spray was reapplied every time the 100's µm droplets were observed again, about every 3-4 experiments. This would seem to have solved the problem, however, in reality applying the anti-condensation spray is a two-step process, the second step of which requires one-day drying time before it could take effect. This would add unnecessary waiting time and potentially delay the experiments.

The radiatively cooled distribution of by McNichols shows the appearance of a new mode of droplets between 30 and 50 µm in diameter not present after precooling. Initially this new mode was thought to be an effect of radiative cooling of the mist. However, estimates of

gravitational settling time of various size droplets suggested that the new mode was more likely due to gravitational settling of droplets. As the mist flowed horizontally along the tube, bigger droplets had the tendency to settle vertically from the top of the tube down into the center of the tube where the measurement windows are located. The mist flowing near the tube walls moves slower than the average or centerline velocity so droplets flowing near the wall (including the top of the tube) have time to grow larger than droplets flowing near the centerline. Large droplets that form near the top of the tube conceivably could settle downward into the center of the tube by the time they reached the measurement window and thereby affect the droplet size measurement. This was eventually postulated to be the reason for the 30-50 μm droplet mode that appeared in Figure 4(c), rather than radiative cooling. Such postulation was the motivation for changes made in the experimental work in this thesis.

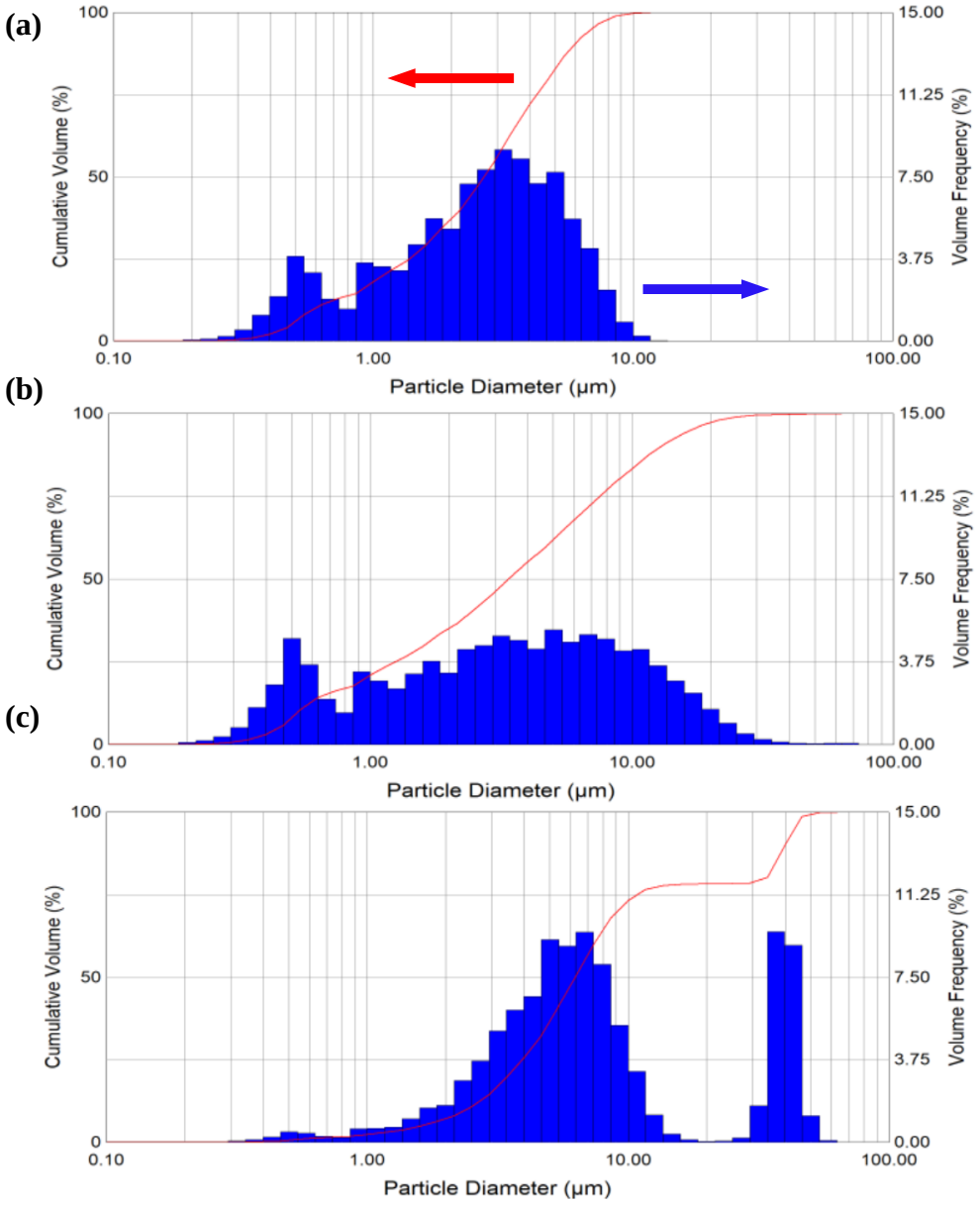

Figure 4. Droplet size distributions measured by McNichols for (a) mist generator output, (b) anti-surface-condensation precooling output and (c) radiative cooling output for a radiative wall temperature of 245 K and a radiative exposure time of 60 seconds (Figure 4.1 in [17]).

1.3 Objectives of the study

The primary objective of the study is to examine the effect of radiation on the growth of cloud-sized mist droplets (with diameter of 10's of µm) by a mist-flow chamber experiment with

a cold radiative sink and compare the result with numerical modeling using heat and mass transfer theory. The secondary objective is to resolve the issues present in the experiments from previous work mostly associated with the precooling section and hence improve the reliability of the experiments. As discussed in previous sections, radiation-induced condensational growth could be an important factor in explaining "condensation-coalescence bottleneck" phenomenon, and we hope to contribute in explaining the role of radiation through the experimental and modeling work of this study.

CHAPTER 2:EXPERIMENTAL METHODS

Working with the original apparatus built by Roman, an improved apparatus including mist generation (with supply air filtering and metering), radiative cooling and droplet size measurement was developed. Each component is discussed in detail in the rest of this chapter.

2.1 Mist generation

Efforts were first made to find an alternative mist generator that could produce droplets of desired sizes so that the precooling section could be eliminated. From [18] we know that for ultrasonic humidifiers droplet sizes increase with decreasing frequency, so we focused on looking for an ultrasonic mist generator with frequency lower than 1.6 MHz, which led us a commercially available ultrasonic piezoelectric atomizing disk by Icstation (disk diameter 20 mm) connected to a circuit board (Figure 5(a)) which operates at 116 kHz frequency. Different than the 1.6-MHz ultrasonic humidifiers, however, the atomizing disks require a water reservoir to be under and in direct contact with the disk (Figure 5(b)). No liquid can be over the top of the disk, or the atomizing stops. The manufacturer of the atomizing disks did not provide detailed information on the atomizing principles of the disks, and no information could be found in peer-reviewed literature. Based on our observation and a patent of ultrasonic atomizing device (U.S. Pat. No. 5,297,734) which seems to utilize a similar atomizing disk, we believe that mist is generated by water being pushed through tapered orifices in the center of the disk, where the inlet openings of the orifices (bottom of the disk where it contacts water) is larger than the outlet openings. Inspection under a microscope shows holes following the pattern showed in Figure 6, which agrees with our hypothesis. Droplet diameters from the atomizing disks fall between 0.6 to

20 μm with a single mode at 8 μm, suitable for our experiments. The size distributions will be presented in CHAPTER 3: EXPERIMENTAL RESULTS in Figure 15 and Figure 19. As a result, the precooling section was taken out, further simplifying the apparatus.

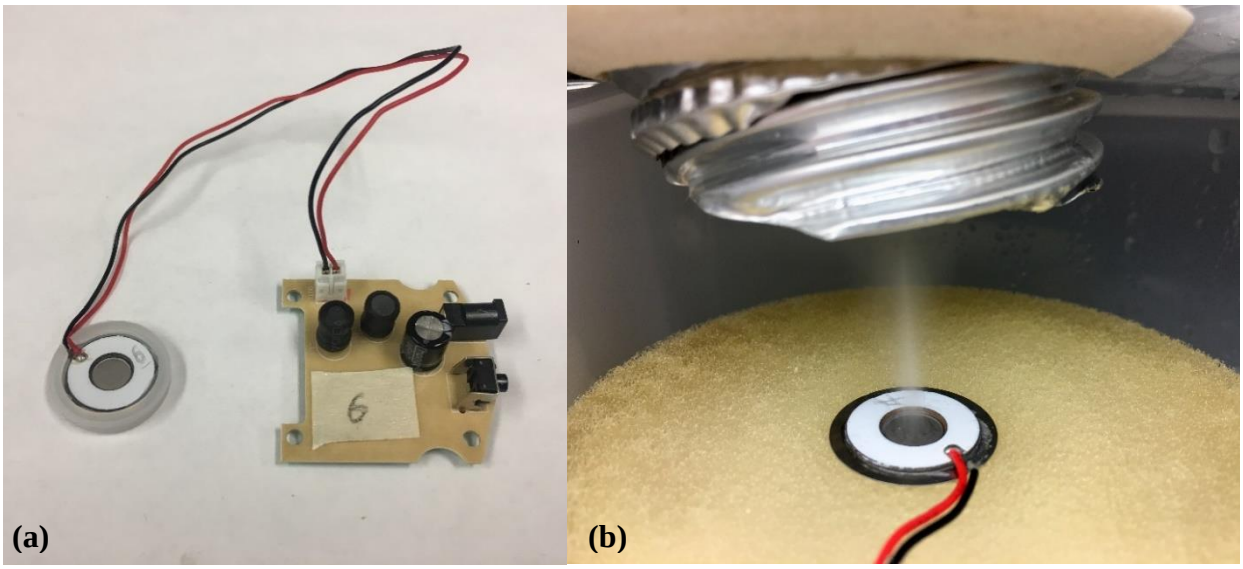

Figure 5. (a) Ultrasonic atomizing disk with circuit board, and (b) atomizing disk working on a wet sponge.

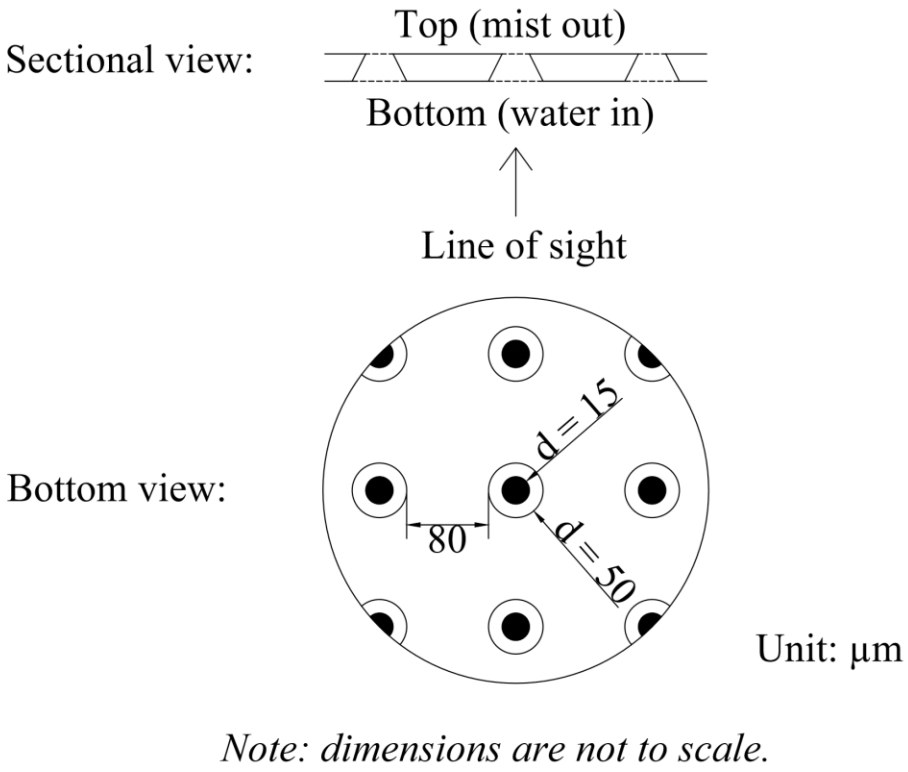

Figure 6. Illustration of the pattern on the disk surface under the microscope.

To ensure constant and controlled performance of the atomizing disk, an airtight housing (also serves as mixing chamber to mix and dilute mist droplets with air) was built as shown in Figure 7. The atomizing disk rests on a sponge soaked with water which acts as both a support and water supply. Water is filled to the top edge of the sponge before each experiment to prolong the operation time without having to soak the sponge often (such water level can sustain the continuous operation of the atomizing disk for four to six hours). Deionized water is used to prevent clogging of the orifices in the atomizing disk. Lab air is supplied to the mist generator box filtered and humidified. The filter used is a 0.2 μm mini-capsule high-efficiency particulate air (HEPA) filter (product no. 12122, Gelman). It removes any naturally occurring aerosols smaller than 0.2 μm in the supply air from getting into the mixing chamber and being activated. A bubble humidifier using deionized water partially submerged in a warm water bath (Figure 8) is built into the air line to humidify the supply air, until condensate forms in the tube at the exit of the humidifier (an indication of the air being saturated). A black synthetic fabric mesh is put into the humidifier to increase the contact between the air flow and water. The device helps to prevent low humidity air from evaporating the droplets. Warm water for bathing is acquired through the hot water supply from tap. There is no additional heater to keep the water warm, but the water in the bath is replaced every 30 minutes during the experiment to keep the supply air saturated. Air flow rate is regulated and measured through two identical parallel rotameters (Matheson, 11220) with a total capacity of 2.4 l/min (Figure 9).

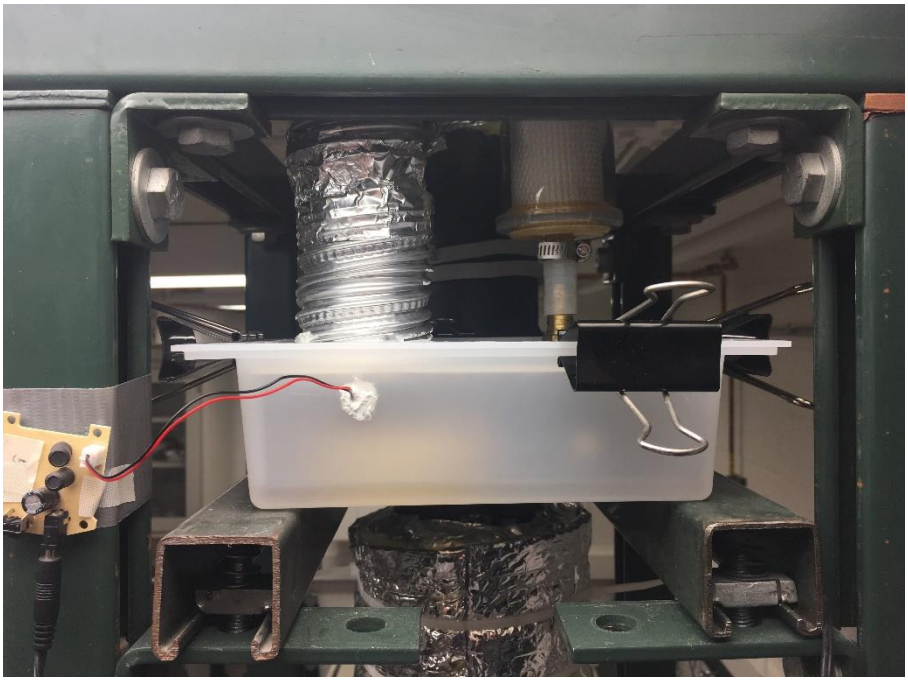

Figure 7. Housing of the mist maker.

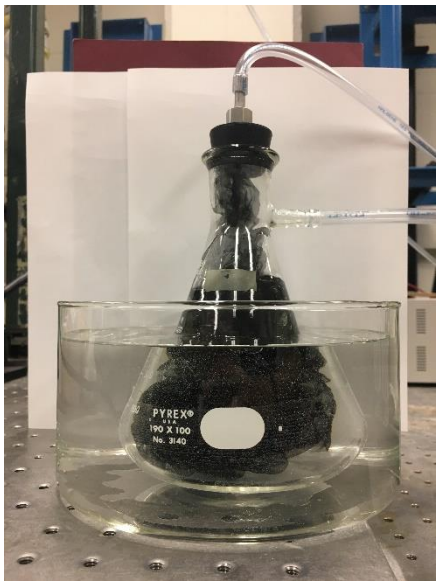

Figure 8. Bubble humidifier with black mesh in warm water bath.

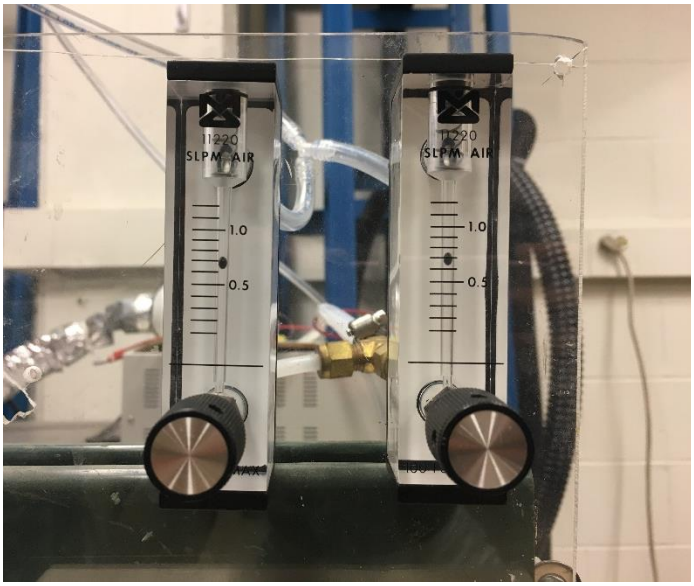

Figure 9. Rotameters for measuring airflow.

2.2 Radiative cooling

The main test section, similar to Roman's, is shown in the picture of the apparatus (Figure 10) and the schematic diagram of the apparatus (Figure 11), where radiative cooling of mist takes place. As discussed in section 1.3, one of the objectives of the study is to address the issues present in previous experimental work, one of them being the postulated gravitational settling of droplets near the upper tube wall. To solve this, a vertical orientation was adopted to set gravity in the same direction as the mist flow, which eliminated droplets settling radially across the tube when it was located horizontally, minimizing the chance of coagulation and collection. The section is comprised of an outer annulus, where liquid nitrogen (LN_2) flows, the LN_2-cooled aluminum (Al) tube wall, and an inner annulus formed between the Al tube wall and a polyethylene (PE) tube. LN_2 is poured into the outer annulus from the funnels on the sides to cool the tube wall to desired temperature to form the radiative sink. According to Roman [16] the inner annulus is made of 0.1 mm thick polyethylene (PE) film, which is largely transparent to infrared radiation. In an effort to reduce convective heat transfer between the PE and mist flow, air at the same temperature of the mist is forced to flow in the inner annulus. Mist from the mist generator box flows within the PE tube (Figure 12), in the center of the test section.

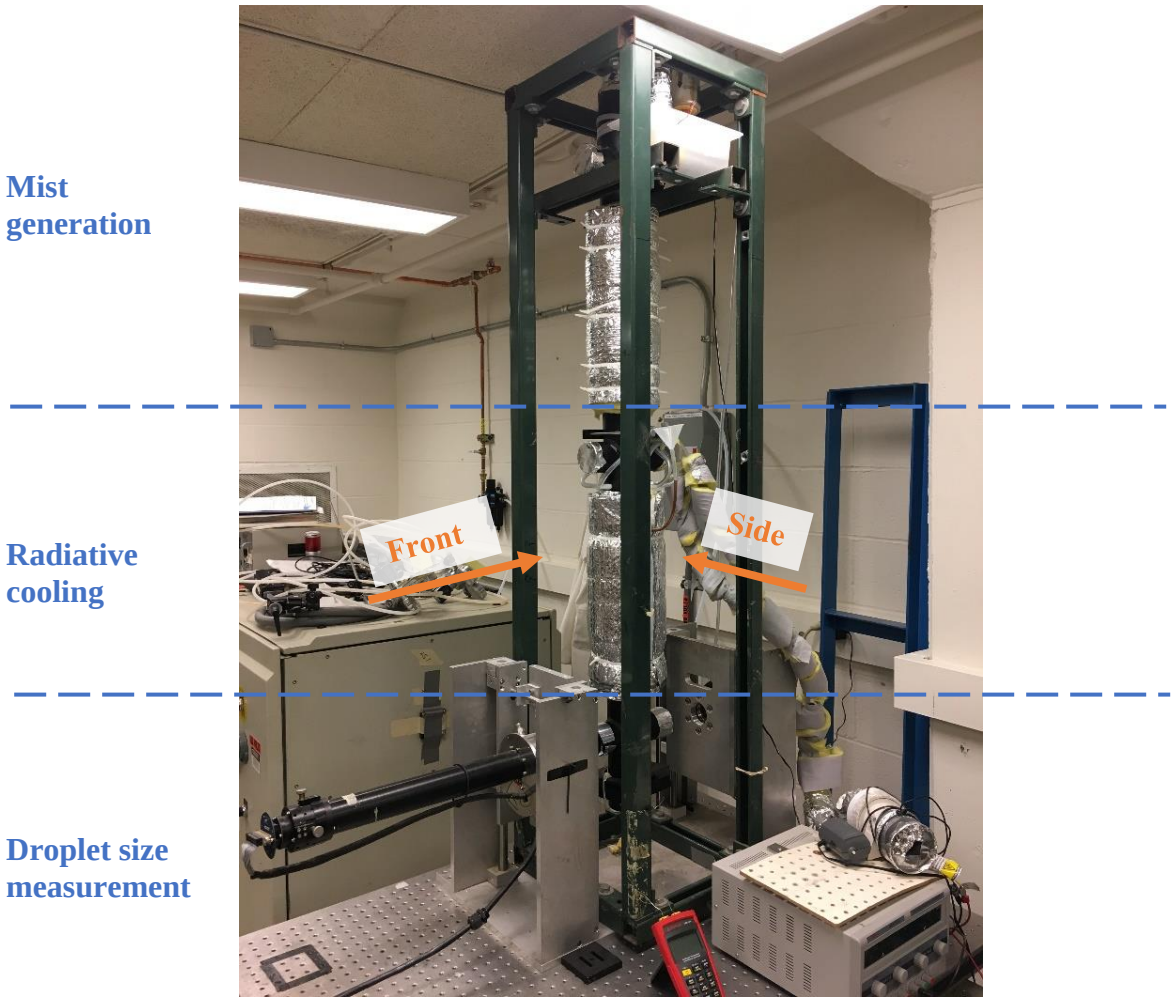

Figure 10. Improved apparatus in the lab. Front and side views correspond with schematic diagram presented below (Figure 11).

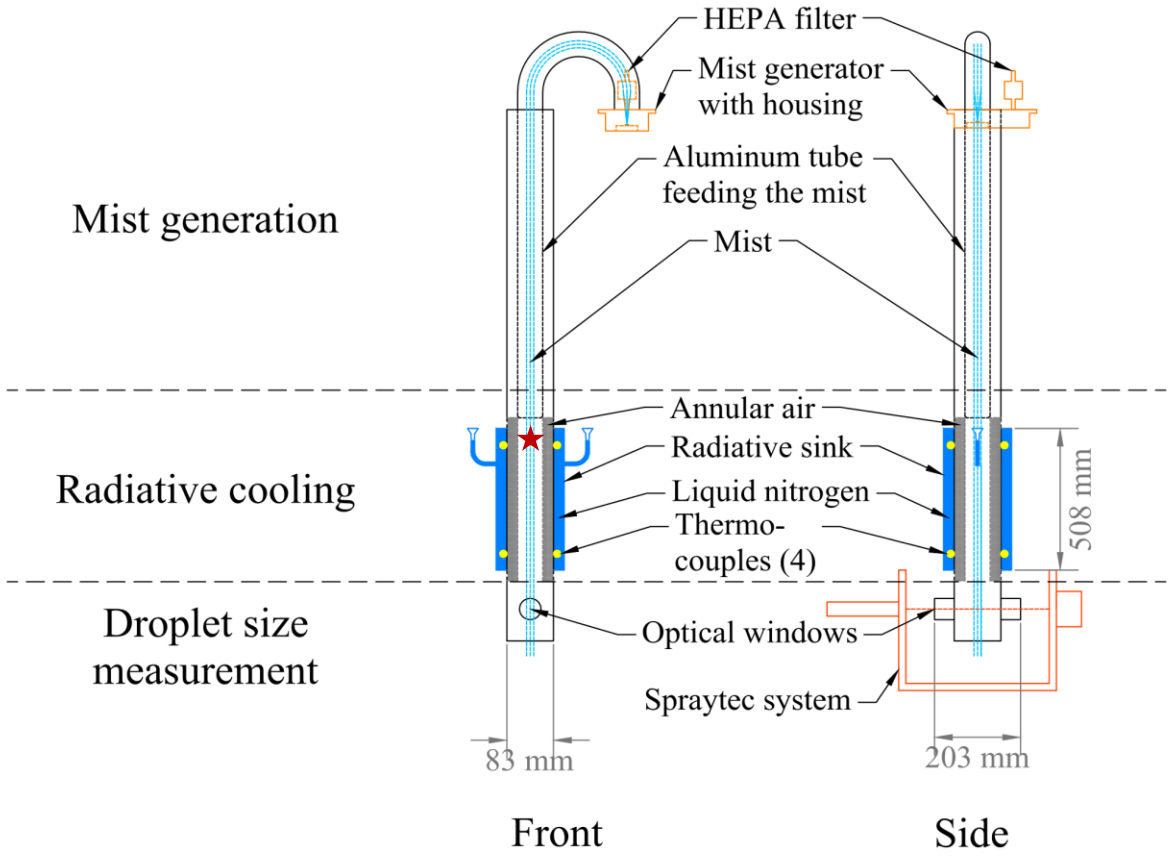

Figure 11. Schematic diagram of the improved apparatus. For clarity of the graphs, air supply tube with rotameters and humidifier are not shown. The red star in the Front view indicates the location inside the tube where Figure 12 was taken.

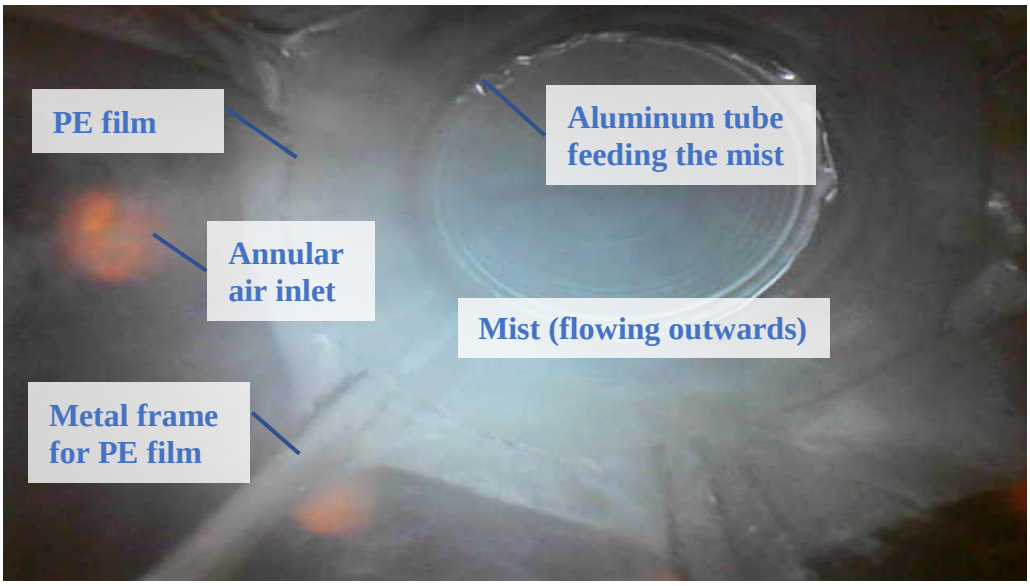

Figure 12. Photograph from inside the test section looking up of the improved apparatus. Shooting location was indicated by a red star in Figure 11.

The presence of an inner annulus is essential to this experiment. Since the objective of this research is to study the effect of radiative cooling alone, all other heat transfer mechanisms should be minimized if not completely removed. In our case, convective heat transfer is of primary concern. In this study, two thermal boundary conditions are studied: isothermal wall condition (same as precedent work) and conductively-adiabatic wall condition. Under isothermal wall condition, the thermal boundary layer formed by the LN_2-cooled Al tube wall is suppressed to as close to the tube wall as possible so as to keep the temperature of the PE constant. Such function is achieved by passing air through the inner annulus that is of the same temperature as the mist entering the radiative cooling section and at a speed that the thermal boundary layer is restricted to within the inner annulus. The Reynolds number of the annulus air flow is kept at 2,000, matching conditions in [16], [17]. Conductively-adiabatic wall condition tries to achieve no temperature difference between the PE tube wall and the mist throughout the radiative cooling section, hence the wall will appear adiabatic in terms of conductive/convective heat transfer. This is achieved by adjusting the annulus air speed until the annular outlet air temperature matches the outlet mist temperature as measured by holding a temperature probe (Klein Tools K-Type thermocouples, model no. 69413) near the air or mist outlet. On the other hand, the presence of an inner annulus should not impede the transmission of radiation. This is realized by using an infrared-transparent material, PE film, to construct the tube. The PE film is chosen for its high transmissivity (close to 1.0) over a wide infrared spectrum (Figure 13).

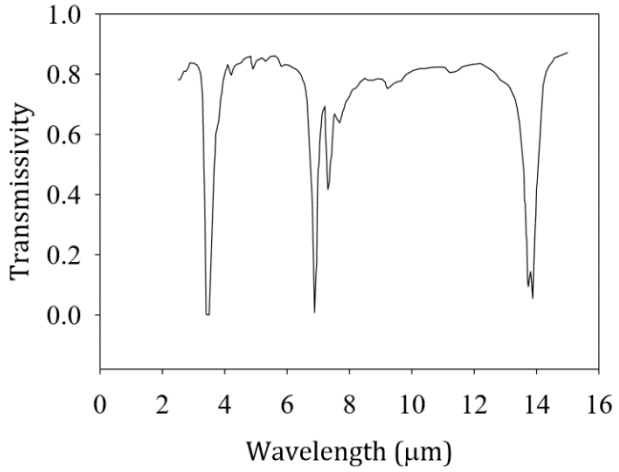

Figure 13. Spectral transmissivity of the 0.1 mm PE film (Fig. 5.6 in [16]).

Experiments are done for various radiant fluxes and droplet residence times in the radiative cooling section. Radiant flux is varied by controlling the amount of LN_2 poured in to vary the sink temperature. The residence time is controlled by the supply air flow rate. One important assumption is that when the flow enters the test section it is hydrodynamically fully developed, hence at the tube center where the size measurement takes place (see Section 2.3), the speed of the mist flow is known and constant. Also, for the radiation effect to be pronounced, the residence time of the mist flow subject to radiative cooling should be reasonably long for a change in the mist size distribution to be observed. 80-second residence time was chosen to conduct the final experiments, which corresponds to a mist flow rate of 1.5 L/s.

2.3 Droplet size distribution data acquisition

Droplet sizes are measured before and after radiative cooling through the optical windows (as shown in Figure 11) close to the exit of the mist. A laser diffraction system, Spraytec (Model No. RTS5008) and the accompanying software, Spraytec 97 (RTSizer) for Windows™ by Malvern Panalytical allow us to acquire the data with ease.

The operating principle of Spraytec system is illustrated in Figure 14. A laser beam at 670 nm wavelength passes through the center of tube and is aligned to reach the center of the detector which is made of 31 concentric rings when there is no dispersed media. The direct, unscattered transmission of the laser beam at the center ring is the highest and should be close to zero at all outer rings. When there are water droplets flowing through the measurement area, part of the laser beam will be scattered and captured by the outer rings in the detector. The directly transmitted part of laser beam will still hit the center ring but with reduced intensity. The amount of light incident on each ring is measured and transmitted to the analyzing software. With user specified optical properties of the particles (water) and the medium (air), the software can back calculate the volume size distribution of the droplets.

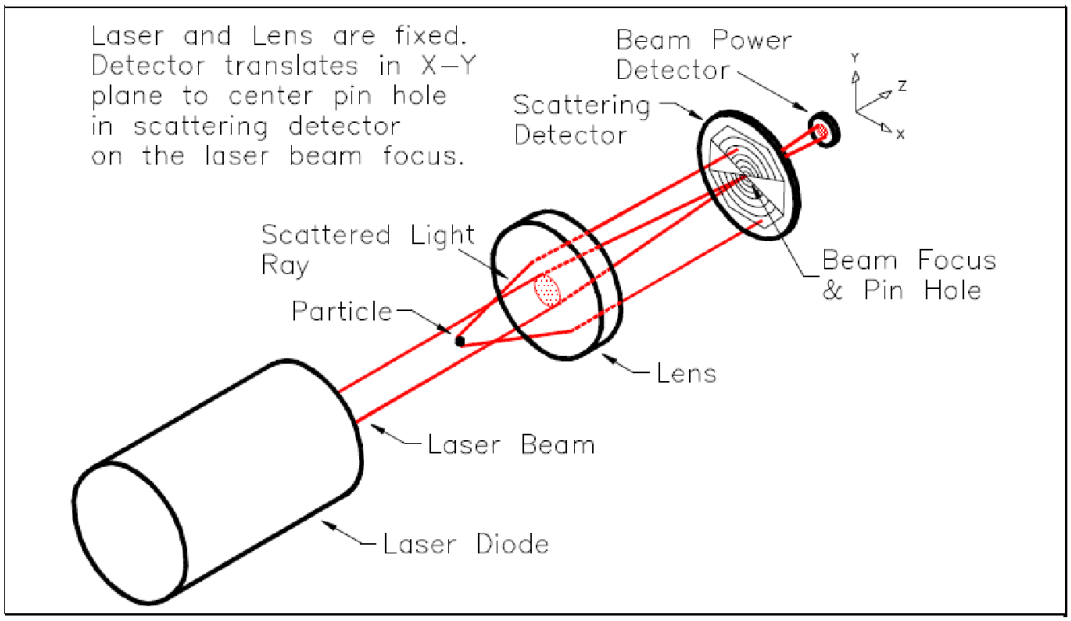

Figure 14. Operating principle of Spraytec laser diffraction system (Figure 8-1 in [19]).

For the combination of the focal length of the lens (450 mm) and the wavelength of the laser (670 nm), the Spraytec system measures an effective pathlength of 11.99 mm (as compared to the test tube diameter of 83 mm) at the center of the system, between the laser diode and the

detector lens. The center of the test tube is aligned at the center of the system. As detailed in Section 2.2, such arrangement tries to ensure that the measurement is made at the center of the fully developed flow. Not that based on snake camera observations, the mist flow appears to be closer to a uniform flow than to a laminar flow, which was contradictory to what was believed in earlier work.

With the 450-mm focal length lens, the effective droplet diameter measuring range for the Spraytec system is reportedly 2.5 – 4,000 μm. Data can still be obtained outside the range but of less accuracy and may not reflect the actual size distribution.

Before conducting droplet size measurements, noise and background measurements need to be conducted. The noise measurement returns the electronic noise of the system as apparent transmission signals across concentric rings, with no laser on. It helps verify or troubleshoot the electronic connections of the system. The background measurement is done after turning on the laser but with no mist flow and returns the transmission signal on each concentric ring. RTSizer uses the background to compensate for any particulate contamination by using the background as a baseline that is subtracted from all droplet size measurements.

The step-by-step procedure of conducting the experiment with the Spraytec system is included as APPENDIX A: EXPERIMENT PROCEDURES.

CHAPTER 3: EXPERIMENTAL RESULTS

3.1 Isothermal wall conditions

3.1.1 Before radiative cooling

Droplet size distributions of the mist flow were measured before it was cooled radiatively. The volume fraction distribution is shown in Figure 15. The maximum coefficient of variation (standard deviation divided by mean) for the measured droplet volume fraction for all six runs was < 0.08% for all droplet diameters, showing stable operation of the mist generator during the course of the experiment.

Note that a few peaks were present in the distribution outside the effective measuring range (droplet diameter < 2.5 μm as discussed in section 2.3). Based on the working principle of the mist generator discussed in section 2.1, it appeared to be quite unusual for the droplet distribution to have multiple modes. Since the results from each run showed constant characteristics of the modes, we postulated that the peaks at indicated diameters less than the main mode at 8 μm were likely due to the system's inability to accurately measure droplets smaller than 2.5 μm. To predict the actual distribution of the droplet assembly from the mist generator, boxcar smoothing (or moving average) was performed on the average measured distribution, as shown in Figure 16. The formula applied is:

$$vf_k = \frac{1}{2n+1} \sum_{i=k-n}^{k+n} vf_{o,i},\ n\ =\ 1\ or\ 2, \tag{1}$$

where vf_k = the volume fraction of the k-th bin after smoothing, and
$vf_{o,i}$ = the volume fraction of the i-th bin before smoothing (original measured data).

We can see that the with n = 1 (neighboring two; solid blue line), the smoothed distribution could accurately capture the behavior of the main mode (≥ 7 μm) while smoothing out the

undesired peaks on or before 2.5 μm. With n = 2 (neighboring four; dashed orange line), better smoothing is achieved on or before 2.5 μm but the accuracy near the main mode is compromised. Therefore, n = 1 is adopted for the following boxcar smoothing of the distributions.

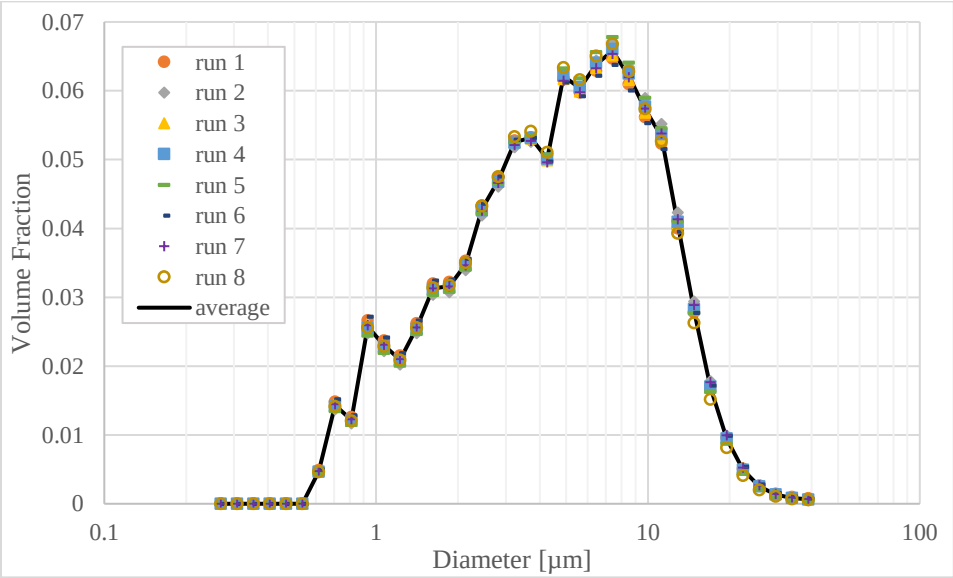

Figure 15. Mist droplet size distribution before radiative cooling for experiments with isothermal wall conditions. Symbols: distribution measured from each run, with the same symbol represents the same run. Line: average distribution.

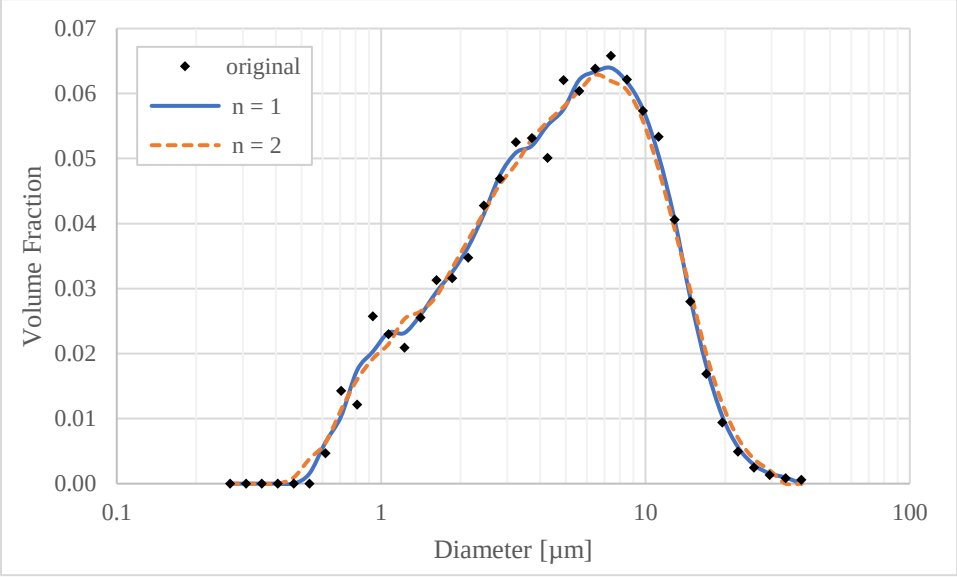

Figure 16. Boxcar smoothing with n = 1 and n = 2 by Eq. (1) for average measured distribution before radiative cooling for experiments with isothermal wall conditions.

Other parameters of the mist before radiative cooling, including liquid water volume concentration Cv, three-two moment, D_{32} and four-three moment, D_{43} of the distributions are presented in Table 1 together with data after radiative cooling.

3.1.2 After radiative cooling

Droplet size distribution data were collected at radiative sink (as shown in Figure 11) temperature T_{sink} = 0 ± 0.5 °C, -10 ± 0.5 °C and -20 ± 0.5 °C respectively as shown in Figure 17. The maximum coefficient of variation for the measured droplet volume fractions for all the runs under the same temperature are less than 0.1%, 0.09% and 0.08% respectively, showing acceptable reproducibility of the results.

Plotting the three average distributions with the distribution before radiative cooling in one graph (Figure 18), we could see that the main mode shifted towards the right (i.e., larger diameter) as the sink temperature decreased. Such a trend was also observed in the parameters (D_{32} and D_{43}) of the distributions (Table 2). The trend agreed with expectation, as lower sink temperature would result in larger radiative heat flux leaving the droplets, cooling the droplets more efficiently so the growth in diameter by condensation would be more pronounced.

As suggested by the measurement results, the lower the sink temperature the more growth observed (the distribution shifts more towards the right). Hence the lowest sink temperature T_{sink} = -20 °C was chosen as a representative to conduct the conductively-adiabatic wall experiment. It was also realized that mist temperatures were missing in the data record, which is an important parameter for understanding the experimental results and for use in the model. The mist temperature measurements were then done for conductively-adiabatic wall experiment.

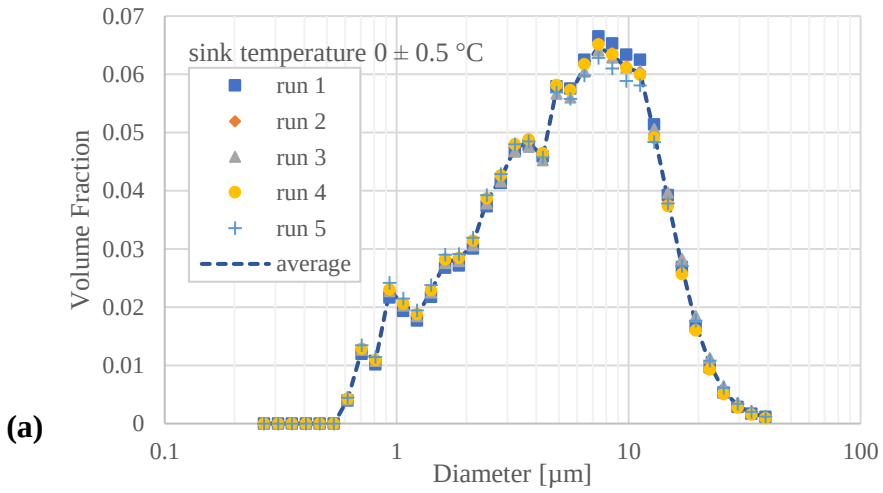

(a)

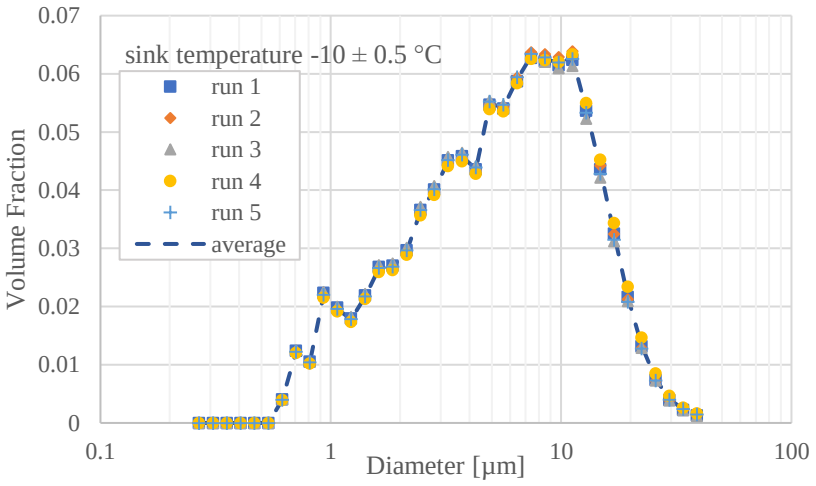

(b)

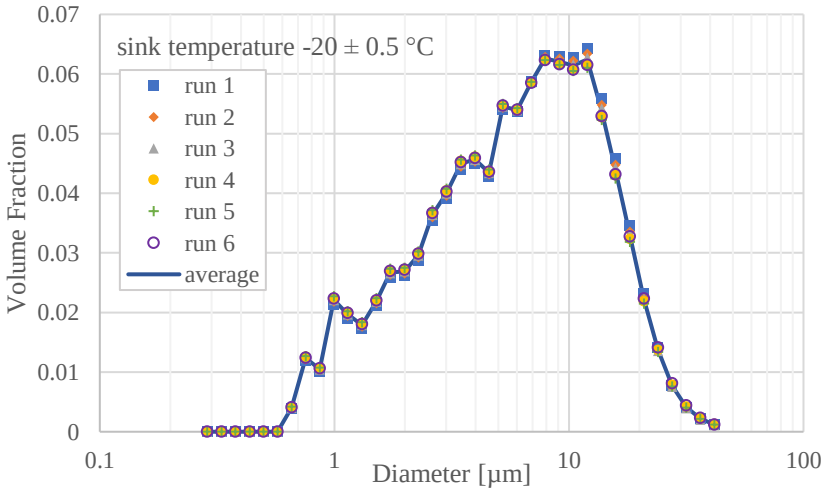

(c)

Figure 17. Measured size distribution after radiative cooling of 80 s with isothermal wall conditions, at sink temperature (a) 0 ± 0.5 °C, (b) -10 ± 0.5 °C, and (c) -20 ± 0.5 °C.

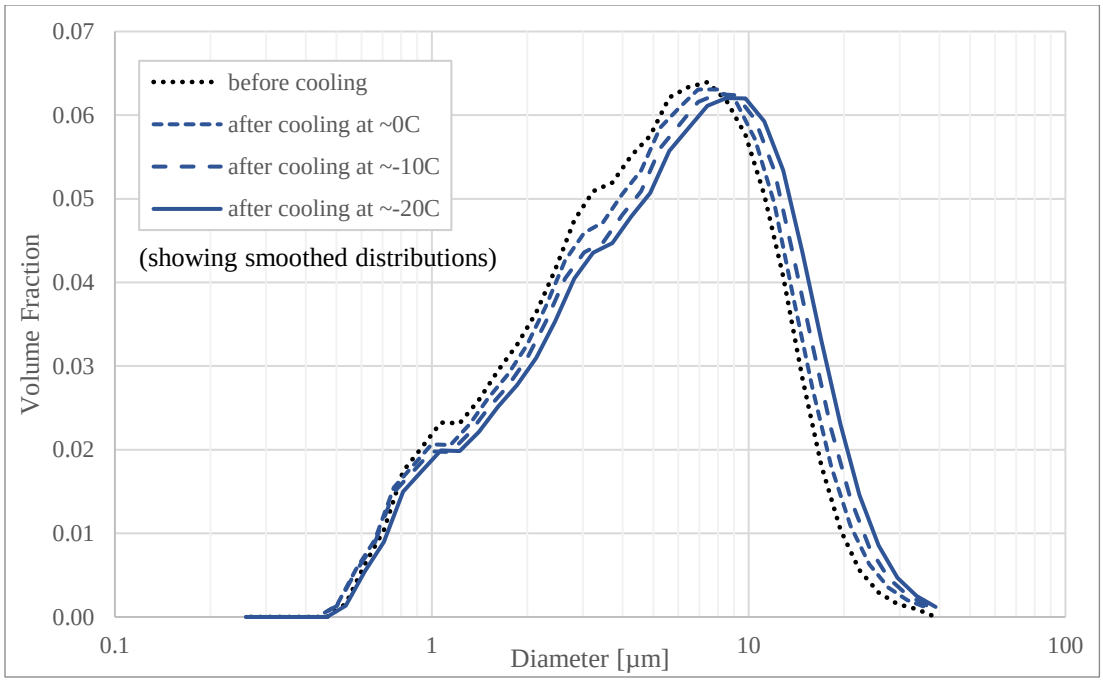

Figure 18. Smoothed size distributions before and after radiative cooling of 80 s with isothermal wall conditions for different sink temperatures.

Table 1. Liquid water volume concentration (Cv), three-two and four-three moments (D_{32} and D_{43}) of droplet size distributions before and after radiative cooling of 80 s for different sink temperatures with isothermal wall conditions.

	T_{sink}	Cv	D_{32}	D_{43}
Before cooling	-	60.7 ± 3.5 ppm	3.09 ± 0.02 µm	6.04 ± 0.04 µm
After cooling	0 ± 0.5 °C	31.2 ± 4.3 ppm	3.14 ± 0.03 µm	6.43 ± 0.05 µm
	-10 ± 0.5 °C	23.2 ± 2.1 ppm	3.25 ± 0.02 µm	6.82 ± 0.07 µm
	-20 ± 0.5 °C	25.2 ± 3.3 ppm	3.47 ± 0.03 µm	7.30 ± 0.05 µm

3.2 Conductively-adiabatic wall conditions

3.2.1 Before radiative cooling

Droplet size distributions of the mist flow were measured before it was cooled radiatively. The volume fraction distribution is shown in Figure 19. The maximum coefficient of variation of the measured droplet volume fraction for all six runs was < 0.15% for all droplet diameters, showing stable operation of the mist generator. Boxcar smoothing with two n values are examined in Figure 20 and, similar to the isothermal-wall experiment, n = 1 (neighboring two) is chosen to present data for this set of experiments.

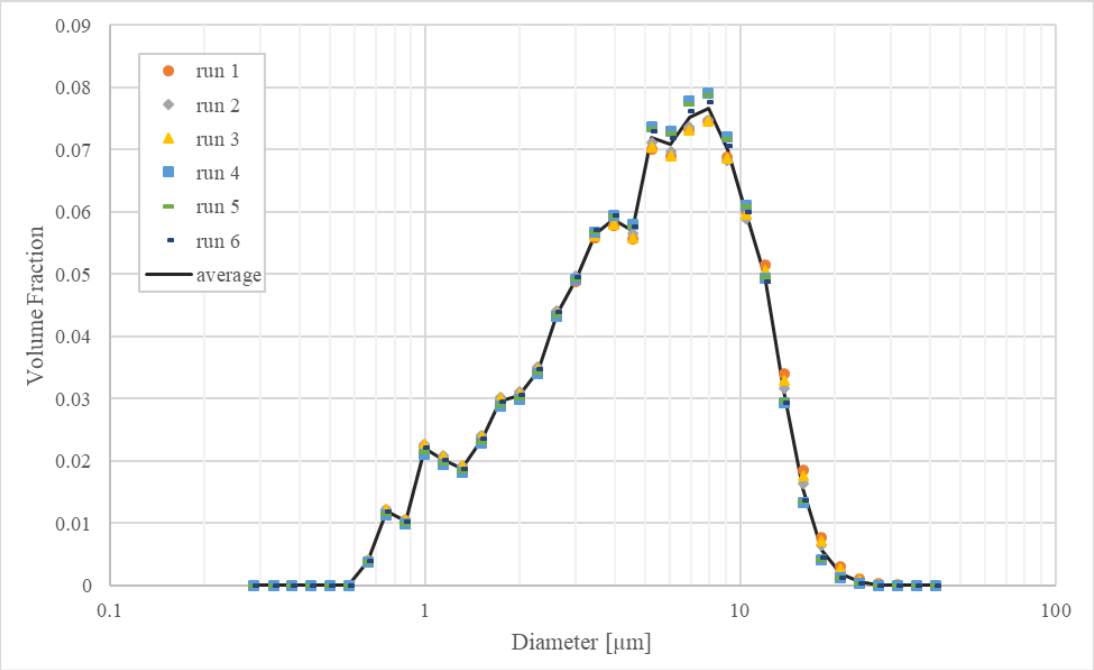

Figure 19. Mist droplet size distribution before radiative cooling for experiments with conductively-adiabatic wall conditions. Symbols: distribution measured from each run, with the same symbol represents the same run. Line: average distribution.

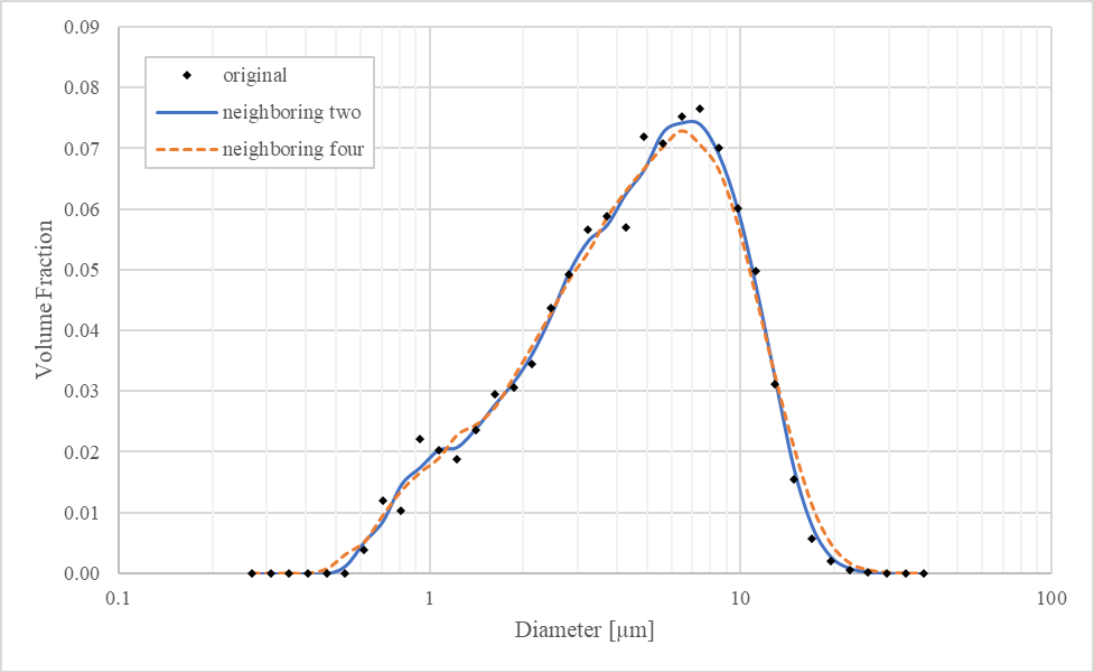

Figure 20. Boxcar smoothing for average measured distribution before radiative cooling for experiments with conductively-adiabatic wall conditions. Solid line (blue): each data point replaced by the arithmetic average of the neighboring two and itself; Dashed line (orange): each data point replaced by the arithmetic average of the neighboring four and itself.

3.2.2 After radiative cooling

Droplet distribution data were collected at sink temperature T_{sink} = -20 ± 0.5 °C and a residence time = 80 s as shown in Figure 21. The maximum coefficient of variation of the measured droplet volume fraction for all six runs is less than 0.3%, showing acceptable reproducibility of the results.

The effect of radiative cooling can be seen in Figure 22, where both distributions before and after radiative cooling are presented. The main mode around 8 µm before radiative cooling is shifted towards the right to around 10 µm, showing noticeable growth in droplet size. Such a trend can also be observed in some parameters (three-two moment, D_{32} and four-three moment, D_{43}) of the distributions (Table 2).

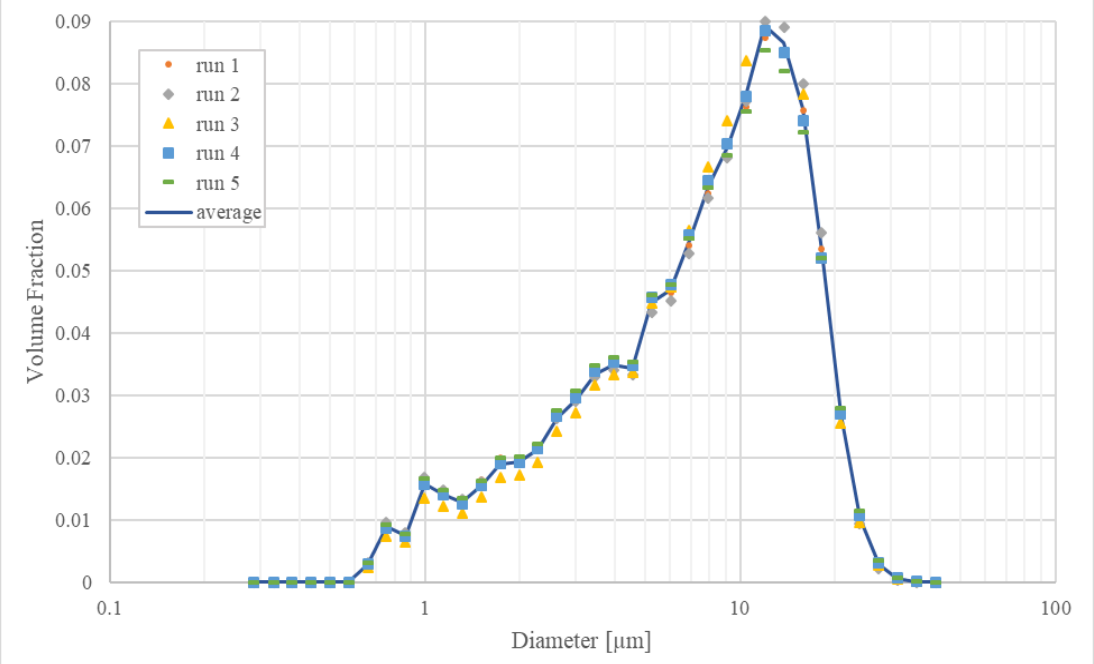

Figure 21. Measured size distribution after radiative cooling of 80 s with conductively-adiabatic wall conditions and sink temperature = -20 ± 0.5 °C. Symbols: distribution measured from each run, with the same symbol represents the same run. Line: average distribution.

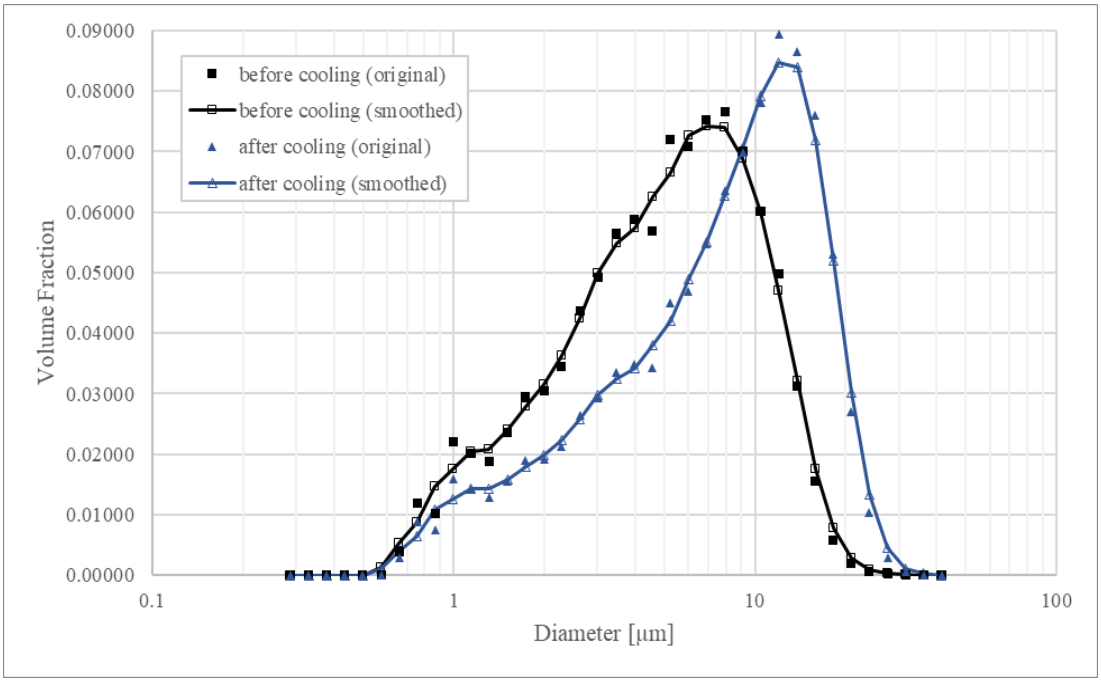

Figure 22. Size distributions before and after radiative cooling of 80 s with conductively-adiabatic wall conditions and sink temperature = -20 ± 0.5 °C. Boxcar smoothing with arithmetic average of the data point and the neighboring two points are also applied, respectively.

Table 2. Liquid water volume concentration (Cv), Three-two and four-three moments (D_{32} and D_{43}) of droplet size distributions before and after radiative cooling of 80 s and sink temperature = -20 ± 0.5 °C.

	Cv	**T_{mist}**	**D_{32}**	**D_{43}**
Before cooling	59.0±4.4 ppm	20.1±1.4 °C	3.17±0.02 μm	5.51±0.04 μm
After cooling (T_{sink} = -20 ± 0.5 °C)	67.9±11.1 ppm	2.9±0.2 °C	4.25±0.13 μm	8.39±0.08 μm

CHAPTER 4: COMPUTATIONAL MODELING

Two computational models, one with Engineering Equation Solver (EES, academic professional version 10.488) and one with MATLAB (version R2019a), for modeling the conductively-adiabatic wall experiments have been developed based on the mass- and energy-balance equations presented below. In this chapter, equations used in the EES model governing the liquid and vapor phases are presented first, followed by the approximate equations used in the MATLAB model, and finally a discussion of the two models. The full EES code is attached as APPENDIX B: ENGINEERING EQUATION SOLVER (EES) MODEL and MATLAB code as APPENDIX C: MATLAB MODEL.

4.1 Droplet (liquid-phase) equations

The equations below describe the mass and energy balances for the liquid phase (droplets) of the system. They are developed first for arbitrary relative humidity of the surrounding vapor phase (air and water vapor mixture), and then for nearly saturated conditions. In the following discussion, subscript *e* denotes vapor-phase mixture (water vapor and air), subscript *a* denotes air, subscript *v* denotes water vapor, subscript ℓ denotes liquid water (i.e. droplets) and subscript *s* denotes droplet surface. Other subscripts that are not applied universally will be defined after the equation where they first appear.

4.1.1 Arbitrary relative humidity (RH)

Thermodynamically, the droplets are an open, unsteady system with both mass and energy crossing the surfaces of the droplets, the aggregate of which is taken as the control surface of the system. They are assumed to be incompressible and insoluble to air. They

exchange heat by conduction with the surrounding vapor phase, and radiation with a remote heat sink. Mass transfer occurs in the form of condensation from the vapor phase on the surface of the droplets or evaporation from the surface of the droplets.

The equations are written as if for a single droplet of diameter *D*. In section 4.2, where balance equations are written for the vapor-phase that surrounds a droplet assembly with a distribution of sizes, a subscript i will be added to appropriate quantities, such as D_i, and sums taken over the terms involving these quantities.

The unsteady mass balance equation for a single droplet of diameter D is

$$\rho_\ell \frac{dD}{dt} = 2\dot{m}'', \tag{2}$$

where ρ_ℓ = density of liquid water, and
$\dot{m}''$ = condensation rate per unit surface area.

The left-hand side (LHS) term in Eq. (2) is the rate of mass accumulation in the droplet due to condensation from the vapor per unit surface area. The right-hand side (RHS) term is the condensation rate per unit surface area, or condensation mass flux. The mass flux at the droplet surface is assumed to be governed by Fick's law of diffusion. The relevant transport property for species diffusion is the binary diffusion coefficient for water vapor in air, D_{12}, where subscript-1 refers to water vapor and subscript-2 refers to air (and such rules follow hereinafter). In the present study, as in many situations, water vapor in the surrounding vapor phase is only of small relative amount or mass fraction which is in the dilute limit ($m_1 << 1$). Another key assumption is the no-slip assumption, that droplet inertia is small enough that the relative velocity between droplets and the surrounding vapor is negligible. This assumption is generally assumed to be valid for cloud or mist droplets [13]. In this dilute, no-slip regime the Fickian mass flux is given by

$$\dot{m}'' = \frac{2\rho D_{12}}{D}(m_{1,e} - m_{1,s}) \ \left(\text{dilute in water vapor}\right), \tag{3}$$

where ρ = vapor-phase mixture $\left(\text{air and water vapor}\right)$ density,

$m_{1,s}$ = mass fraction of water vapor near the droplet surface, and

$m_{1,e}$ = mass fraction of water vapor in the environment (far from the droplet surface).

The unsteady droplet energy balance equation is

$$\rho_\ell C_{p,l} \frac{D}{6} \frac{dT_s}{dt} = q_{c,s} - q_r Q_a + \dot{m}'' h_{fg}\,, \tag{4}$$

where $C_{p,l}$ = specific heat of liquid water,

T_s = droplet surface temperature,

$q_{c,s}$ = conductive heat transfer from the surrounding vapor to the droplet surface,

q_r = blackbody radiative heat transfer from the droplet to the radiative sink (will be defined in Eq. (6)),

Q_a = droplet absorption efficiency (will be defined in Eq. (7)), and

h_{fg} = latent heat of water.

The LHS of Eq. (4) is the unsteady term related to the rate of energy storage in the droplet per unit surface area. It is the energy accumulation term minus the contribution due to condensative mass accumulation in the droplet, $\dot{m}'' h_f$, which has been moved to the RHS and combined with the energy flux associated with saturated water vapor diffusing to the droplet surface and condensing, $\dot{m}'' h_g$, to form the net latent energy flux term, $\dot{m}'' h_{fg}$.

The conductive (or diffusive) heat flux at the droplet surface is assumed to be governed by Fourier's law of heat conduction, given that species-diffusion energy flux is negligible in the dilute limit. In this dilute, no-slip regime, the Fourier conductive heat flux at the droplet surface is

$$q_{c,s} = \frac{2k}{D}\left(T_e - T_s\right), \tag{5}$$

where k = vapor-phase thermal conductivity, and

T_e = temperature of the environment far away from the droplet surface.

If the droplet is part of an optically thin assembly so that it directly exchanges radiation with a remote sink that is a large isothermal surrounding at radiative sink temperature T_r through a unity view factor (source-to-sink view factor $F_{sr} = 1$), and it is treated as a non-reflecting, non-refracting, gray emitting-absorbing sphere in the geometric optics regime with gray internal absorption coefficient K_a. Note that in the discussion in section 5.2, T_r is referred to as T_{sink} to accommodate the definition in the experimental sections; they are effectively interchangeable. The radiation terms in Eq. (4) are

$$q_r = \sigma\left(T_s^4 - T_r^4\right), \tag{6}$$

where σ = Stefan-Boltzmann constant = 5.67 x 10^{-8} W·m^{-2} K^{-4} ,

T_r = radiative sink temperature, and

$$Q_a \simeq 1 - \exp(-K_a D(2/3)), \tag{7}$$

where K_a = grey absorption coefficient = $1/(4.3 \times 10^{-6})$ m^{-1} [13].

Cloud droplets are typically assumed to be thermally quasi-steady (QS) over time scales of importance fluid mechanically in cloud dynamics [13]. This is a significant mathematical simplification because the droplet energy equation changes from differential to algebraic. The QS assumption involves neglecting the LHS of the droplet energy Eq. (4) to give,

$$0 = q_{c,s} - q_r Q_a + \dot{m}'' h_{fg}; \tag{8}$$

combining with Eq. (5) gives the QS droplet energy equation:

$$\Delta T \equiv T_s - T_e = \frac{D}{2k}\left(-q_r Q_a + \dot{m}'' h_{fg}\right). \tag{9}$$

4.1.2 Nearly saturated environment

Cloud droplets typically exist in a nearly saturated vapor-phase environment. Therefore, it is common to specialize the QS droplet equations developed above to conditions near saturation. Supersaturation, *s*, is introduced and defined as the relative humidity (*RH*) minus one:

$$s = RH - 1. \tag{10}$$

Perfect saturation over a flat interface of pure water means $s = 0$. The liquid droplets in clouds typically raise the RH slightly above 100% (s slightly above zero by a fraction of a percent) due to the Kelvin effect associated with the curvature of the droplets. A typical magnitude of s in stable clouds is less than a fraction of a percent, such that near-saturation conditions prevail: $|s| << 1$. The Clausius-Clapeyron equation is introduced to describe the variation of saturation pressure (equilibrium vapor-pressure over a flat interface) with temperature. In integrated form (assuming h_{fg} does not change for small deviations from saturation) the Clausius-Clapeyron equation is:

$$\frac{P_{sat,s}(T_s)}{P_{sat,e}(T_e)} = \exp\left[\frac{h_{fg}}{R_w}\left(\frac{1}{T_e} - \frac{1}{T_s}\right)\right], \tag{11}$$

where $R_w =$ ideal gas constant for water vapor = 461.5 J/kg-K,
$P_{sat,s}(T_s) =$ saturation water vapor pressure over droplet surface at surface temperature T_s, and
$P_{sat,e}(T_e) =$ saturation water vapor pressure far from droplets at environment temperature T_e.

For small supersaturation values the temperature difference ΔT between the droplet and the environment as previously defined in Eq. (9) is also very small, hence the following approximation could also be applied:

$$\frac{h_{fg}\,|\Delta T|}{R_w T^2} << 1, \tag{12}$$

where $T = T_s \approx T_e$, for small ΔT as defined in Eq. (9).

Taylor series expansions are applied to the QS droplet energy equation (Eq. (9)) to obtain (see [13] for details) the following approximate *explicit* relations for droplet temperature and size:

$$\Delta T \approx \frac{s - Q_r D \dfrac{\Psi}{H} - \dfrac{D_c}{D} + \left(\dfrac{D_s}{D}\right)^3}{H + \Psi}, \tag{13}$$

$$\frac{dD^2}{dt} \approx \frac{\Gamma\left(s + Q_r D - \dfrac{D_c}{D} + \left(\dfrac{D_s}{D}\right)^3\right)}{H + \Psi}, \tag{14}$$

where $H = \dfrac{h_{fg}}{R_w T^2}$; $\quad \Psi = \dfrac{k R_w T}{D_{12} h_{fg} P_{sat,e}}$; $\quad \Gamma = \dfrac{8k}{\rho_\ell h_{fg}}$; $\quad Q_a = \dfrac{Q_a q_r H}{2k}$.

The first relation above (Eq. (13)) is the QS algebraic droplet energy equation. The second relation (Eq. (14)) is the combined (algebraic) energy and (differential) mass equations. The quantity D_c is the effective diameter for the Kelvin effect, which is introduced when the equilibrium water vapor partial pressure at the droplet surface $P_{v,s}$ is corrected for curvature effect (surface tension), and is typically of order 10^{-3} μm. The effective Kelvin diameter can be defined in terms of more basic physical properties such as surface tension and can be found in [13]. The Kelvin term, with a D^{-1} dependence, becomes less important for increasing D values. The solute term, which has a D^{-3} dependence, becomes less important at increasing diameters, where surface tension and radiation effects become more important.

4.2 Vapor-phase equations

Here the vapor-phase mass and energy balance equations are presented. The vapor phase is assumed to be a dilute, binary (air and water vapor) ideal-gas mixture that surrounds a polydisperse assembly of spherical liquid water droplets that are incompressible, insoluble to air,

and have negligible inertia (no velocity slip). Thermodynamically, the vapor-phase is an open, unsteady system with both mass and energy crossing part of the control surface of the system—the part that is the aggregate of all the droplet surfaces. The other part of the control surface for the vapor phase would be an outer boundary corresponding to an enclosure surface. For the sake of presenting the equations the enclosure surface is viewed as the surface of a control mass, a volume of fixed mass (but arbitrary size) flowing with the mist at constant pressure. In this (LaGrangian) view the change in quantities is written as a material time derivative d()/dt. Transformation between the LaGrangian and Eulerian views can be made by introducing an axial mist flow velocity u to give d()/dt = ud()/dx. Other than the microscopic heat conduction around each droplet that is associated with the small ΔT noted in Eq. (9), macroscopic heat conduction in the vapor phase is neglected here. For flow in a tube, this corresponds to assuming an adiabatic wall boundary condition.

The mass of vapor, m_e, is the sum of the air and water-vapor masses (m_a and m_v, respectively):

$$m_e = m_a + m_v. \tag{15}$$

The mass of air in the vapor phase m_a is constant. The unsteady mass conservation equation for water-vapor is:

$$\frac{dm_v}{dt} = -\pi \sum_i N_i \dot{m}_i'' D_i^2, \tag{16}$$

where i = bin number in the models, and
N_i = total number of droplets in bin i.

The unsteady energy conservation equation for the vapor phase is:

$$\rho_e\left(1-f_{v,\ell}\right)C_{p,e}\frac{dT_e}{dt}=-2\pi k\sum_i N_{v_i}D_i\left(T_e-T_{s,i}\right)$$
$$=-12k\sum_i\frac{f_{v_i}}{D_i^2}\left(T_e-T_{s,i}\right), \tag{17}$$

where ρ_e = density of the vapor phase (water and air),

$f_{v,\ell}$ = total volume concentration of liquid (droplets) = $\sum_i f_{v_i} = \frac{\pi}{6}\sum_i N_{v_i}D_i^3$,

f_{v_i} = volume concentration of liquid (droplets) in bin *i*,

N_{v_i} = volumetric number density of droplets in bin *i*, and

$C_{p,e}$ = specific heat of the vapor phase.

Note that the total number of droplets N_i is replaced by the volumetric number density N_{v_i}.

Vapor phase density ρ_e has units of mass per unit volume of vapor phase, say, kg of vapor per cubic meter of vapor, which is technically different than kg of vapor per cubic meter of mist, but the difference is negligible since the total liquid water volume concentration is negligibly small in the present study.

The equations compiled up to this point, consisting of separate droplet-phase and vapor-phase equations, together comprise a complete, coupled set of equations that can be solved numerically for the evolving droplet temperatures, droplet diameters, vapor temperature, and other variables as a function of time (or distance along a tube) for an adiabatic tube wall condition (i.e., neglecting radial heat conduction).

4.3 Combined liquid (droplet) and vapor phase equations

When the droplet phase and vapor phase are combined the system becomes a closed system of fixed mass of air and water with a moving outer boundary. The change in internal energy *U* of the system is still written as a material derivative, d()/d*t* (in some places written as D/D*t*), balanced by radiation from the droplet phase and *PV*-work at the system outer boundary:

$$\frac{dU}{dt} = -\pi \sum_i N_i q_{r_i} Q_{a_i} D_i^2 - P\frac{dV}{dt}. \tag{18}$$

At this point, the equation is written without any heat conduction term(s) because the system is arbitrarily large. Using the definition of enthalpy *h* (and the constant pressure condition) to combine the internal energy and *PV*-work terms gives

$$m\frac{dh}{dt} = -\pi \sum_i N_i q_{r_i} Q_{a_i} D_i^2 . \tag{19}$$

Next, the energy balance equation above, which applies to an arbitrarily large control volume of mass *m*, is divided by the volume of the system. Upon doing so, the equation takes on the usual form of a volumetric energy balance differential equation (in W/m^3, for example) and a term for radial heat conduction can be included, written here in cylindrical coordinates with variable *r* (axial conduction is assumed to be negligible):

$$\rho\frac{dh}{dt} = -\pi \sum_i N_{v_i} q_{r_i} Q_{a_i} D_i^2 + \frac{k}{r}\frac{d}{dr}\left(r\frac{dT_e}{dr}\right). \tag{20}$$

This equation applies to the two-phase mixture consisting of vapor (ideal gas) and liquid droplets (which are incompressible and insoluble to air), such that the mixture density ρ and mass-specific enthalpy h are, respectively:

$$\rho = \rho_e\left(1 - f_{v,\ell}\right) + \rho_\ell f_{v,\ell} , \tag{21}$$

$$h = \rho_e\left(1 - f_{v,\ell}\right)h_e + \rho_\ell f_{v,\ell} h_\ell . \tag{22}$$

Approximate analytical solutions can be obtained from the volumetric energy equation to describe the variation of the mixture (mist flow) temperature under certain limiting conditions. For this purpose the radiation term is linearized by defining a radiative heat transfer coefficient h_r:

$$q_{r_i} = h_r \left(T_{s_i} - T_r \right) \simeq h_r \left(T_e - T_r \right), \tag{23}$$

$$h_r = \sigma \left(T_e^2 + T_r^2 \right) \left(T_e + T_r \right). \tag{24}$$

whereupon the volumetric energy equation (Eq. (20)) becomes:

$$\rho \frac{dh}{dt} = -4 h_r K_{a_P} \left(T_e - T_r \right) + \frac{k}{r} \frac{d}{dr} \left(r \frac{dT_e}{dr} \right), \tag{25}$$

where the Planck mean absorption-emission coefficient K_{a_P} is

$$K_{a_P} = \sum_i \frac{1.5 f_{v_i} Q_{a_i}}{D_i}. \tag{26}$$

4.4 Combined vapor and droplet phase equations for non-volatile droplets

A limiting regime that is useful for examining the heat transfer behavior of the system is that of droplets that are assumed to be non-volatile, meaning non-condensing and non-evaporating. In this limit the mixture enthalpy change term can be written in the familiar form of a temperature derivative, which can be changed from the Lagrangian description to a Eulerian one, with *x* being the mist flow tube axial coordinate, *r* the radial coordinate, and *u* the flow velocity, assumed to be constant radially, i.e., uniform velocity profile. In addition, the distinction between vapor temperature and droplet temperatures is dropped; for the present purposes the difference (typically a few percent of one degree) is negligible:

$$\rho C_p u \frac{dT}{dx} = -4 h_r K_{a_P} \left(T - T_r \right) + \frac{k}{r} \frac{d}{dr} \left(r \frac{dT}{dr} \right). \tag{27}$$

Non-dimensional variables are defined using the initial mist temperature T_o and the polyethylene tube radius R_1:

$$\theta = \frac{T - T_r}{T_o - T_r}, \tag{28}$$

$$r' = \frac{r}{R_1}, \tag{29}$$

$$x' = \frac{xk}{\rho C_p u R_1^2}, \tag{30}$$

$$Q_r = \left(\frac{h_r 2R_1}{k} \right) \left(K_{a_P} 2R_1 \right). \tag{31}$$

where a non-dimensional radiative parameter Q_r is defined as the product of a radiative Nusselt number based on polyethylene tube diameter and a Planck mean optical depth based on that same diameter. These definitions transform the equation as follows:

$$\frac{d\theta}{dx'} = -Q_r \theta + \frac{1}{r'} \frac{d}{dr'} \left(r' \frac{d\theta}{dr'} \right), \tag{32}$$

where $\theta(x' = 0) = 1, \quad \left. \frac{d\theta}{dr'} \right|_{r'=0} = 0.$

4.4.1 Adiabatic wall: no radial conduction and non-volatile droplets

The approximate solution considered here with non-volatile droplets is that which includes only radiative cooling by the droplets and neglects radial conduction in the vapor, i.e., for an adiabatic wall (and assuming constant Q_r):

$$\theta = \exp\left(-Q_r x'\right) = \exp\left(-x''\right) = \exp\left(-t''\right). \tag{33}$$

where the following scaling gives the characteristic distance or time for temperature change due to radiative cooling (non-volatile droplets):

$$x'' = \frac{x}{x_r}, \tag{34}$$

$$x_r = \frac{\rho C_p u}{4 h_r K_{a_P}}, \tag{35}$$

$$t'' = \frac{t}{t_r}, \tag{36}$$

$$t_r = \frac{\rho C_p}{4 h_r K_{a_P}}. \tag{37}$$

where t_r means the time for the temperature to drop 1-1/e (~ 63%) of its total possible change.

4.5 Combined vapor- and droplet-phase equations for volatile (condensing) droplet without radial conduction in the tube

The governing equation for this solution can be obtained from Eq. (17) in the vapor-phase equation section (section 4.2) above:

$$\rho_e \left(1 - f_{v,\ell}\right) C_{p,e} \frac{dT_e}{dt} = -12k \sum_i \frac{f_{v_i}}{D_i^2} \left(T_e - T_{s,i}\right), \tag{38}$$

by neglecting the liquid-phase volume fraction, dropping the e-subscript on density and specific heat (the vapor phase dominates these properties in the two-phase mixture), introducing the analytic solution (small *s*) for temperature difference between droplets and vapor (neglecting the solute term):

$$\Delta T = \left(T_{s,i} - T_e\right) \approx \frac{s - Q_{r,i} D_i \dfrac{\Psi}{H} - \dfrac{D_c}{D_i}}{H + \Psi}, \tag{39}$$

and linearizing the radiation term to give

$$\frac{d\theta}{dt} = 1/t_c - \theta/t_{rc}\ , \tag{40}$$

$$t_c = \frac{\rho C_p \left(T_o - T_r\right)\left(\Psi + H\right)}{12k\sum_i \left(s - \frac{D_c}{D_i}\right)\frac{f_{v_i}}{D_i^2}} \ , \tag{41}$$

$$t_{rc} = \frac{t_r\left(\Psi + H\right)}{\Psi} = \frac{\rho C_p}{4h_r K_{a_P}}\left(1 + \frac{H}{\Psi}\right). \tag{42}$$

Assuming constant s, D_c, ρ, H, Ψ, C_p, h_r and K_{a_P}, and using an integrating factor gives the solution:

$$\theta = \frac{t_{rc}}{t_c} + \left(1 - \frac{t_{rc}}{t_c}\right)\exp\left(-t / t_{rc}\right). \tag{43}$$

The characteristic time for temperature change with radiation and condensation is t_{rc}, which is bigger (longer) than the characteristic time for only radiation t_r by the factor $(1 + H / \Psi)$. The long-time, asymptotic value of non-dimensional temperature is t_{rc}/t_c:

$$\frac{t_{rc}}{t_c} = \frac{12k}{4h_r K_{a_P}} \frac{\sum_i \left(s - \frac{D_c}{D_i}\right)\frac{f_{v_i}}{D_i^2}}{\Psi\left(T_o - T_r\right)}. \tag{44}$$

The parameter t_c can have either plus or minus sign or be zero. The magnitude of t_c would be the characteristic time for 1-1/e temperature change if only phase change occurred (no radiation) at the same values of f_{vi}, s and D_c/D_i. These values can be such that, without radiation, either condensation or evaporation would occur. A plus sign means condensation would occur; a minus sign means evaporation would occur.

In the limit of large Ψ and small H ($H / \Psi \rightarrow 0$), as would occur for non-volatile droplets (i.e., $P_{s,e}$ and/or h_{fg} vanishingly small), the characteristic times would rank as $|t_c| >> t_{rc} \rightarrow t_r$ and the solution would revert to that given above for non-volatile droplets with radiation only (no radial conduction).

4.6 Quasi-steady water vapor approximation

Numerical solution of the coupled droplet- and vapor-phase problem of mist condensation induced by radiative cooling for the adiabatic wall condition shows that the vapor-phase relative humidity or supersaturation achieves a quasi-steady value almost immediately that is maintained throughout the process. Examination of this value of quasi-steady supersaturation suggests that it can be approximated analytically in the following way. Consider first a droplet phase that is mono-sized at diameter *D*. Assuming that the e-state water vapor partial pressure is the same as the water-vapor partial pressure at the surface of the droplets, the definitions of relative humidity and supersaturation give the following:

$$1 + s = RH = \frac{P_v}{P_{s,e}} = \frac{P_{s,e}\exp(D_c / D)}{P_{s,e}} \simeq 1 + \frac{D_c}{D}; \quad \frac{D_c}{D} << 1. \tag{45}$$

where only the Kelvin effect has been assumed to modify the vapor pressure adjacent to the droplets (no solute effect). Thus the quasi-steady supersaturation is approximately the ratio D_c/D and the fully-coupled numerical calculations that solve the water mass balance equation for supersaturation confirm this.

$$s \simeq \frac{D_c}{D}; \quad \text{monodisperse droplets.} \tag{46}$$

The difference between the numerical quasi-steady supersaturation value and this approximation is small. This small difference is what would be expected according to the neglect of the small difference in vapor pressure between the surface of the droplets and the bulk vapor-phase e-state. To account for the polydispersed droplet size distribution requires taking into account the varying surface area of different size droplets.

$$s \simeq \frac{\sum_i \frac{D_c f_{v_i}}{D_i^3}}{\sum_i \frac{f_{v_i}}{D_i^2}} \Rightarrow \sum_i \left(s - \frac{D_c}{D_i} \right) \frac{f_{v_i}}{D_i^2} = 0; \quad \text{polydisperse droplets.} \tag{47}$$

From the water mass balance it can be seen that this approximation is equivalent to assuming $dm_v/dt = 0$, in other words, the water vapor mass accumulation rate is small compared to the individual condensative or evaporative mass flux terms. If some of the droplets in an assembly (the smaller ones) are evaporating while some (the larger ones) are condensing, this quasi-steady approximation implies that the difference between water-vapor input to the vapor phase from evaporating droplets and the water-vapor out-take from the vapor phase by condensing droplets (i.e., dm_v/dt) is small compared to each of these sums individually. This approximation also implies that $t_c \rightarrow \infty$ in the previous combined condensing droplet-and vapor-phase analytical temperature solution such that:

$$\frac{d\theta}{dt} = -\frac{\theta}{t_{rc}}. \tag{48}$$

This quasi-steady water-vapor approximation is also applicable during a process that is entirely adiabatic, i.e., radiatively adiabatic as well as conductively, such that temperature stays constant. During such a process supersaturation decreases as smaller droplets evaporate and larger droplets grow by condensation but temperature and water-vapor mass stay fairly constant.

4.7 The EES and the MATLAB model

Two mathematical models were developed in this research, an EES model (by X. Li) and a MATLAB model (by M. Q. Brewster and X. Li). The EES model was used to solve the fully coupled set of equation with the unsteady water vapor mass equation included. The MATLAB

model was used to solve the similar set of equations but with the quasi-steady water vapor approximation included.

EES is a general equation-solving program that can numerically solve thousands of coupled non-linear algebraic, differential and integral equations. A major feature of EES is the high accuracy thermodynamic and transport property database that is provided for hundreds of substances that can be used with the equation solving capability, making it a suitable choice for our purpose which is to solve coupled heat and mass transfer equations. The EES code developed for this project contains 1,016 equations and the same number of variables, most of which need to be supplied proper initial guesses for the program to run without stopping. This is because EES uses Newton's method to solve systems of non-linear equations which requires the initial guess of a variable to be at least of the same order of magnitude as the final solution [20]. Variable information including units, initial guesses, upper and lower limits for solving the EES model is provided as APPENDIX D: VARIABLE INFORMATION FOR EES MODEL. Different than EES, MATLAB processes the characteristics of a programming language, where variables need to be defined before they are used, and equations have to be in a certain sequence. It also does not have in-built thermodynamic property functions so variables with strong temperature dependence (such as saturation vapor pressure) needs to be manually supplied with a polynomial curve fit. However, the MATLAB code does not need the same level of initialization as it solves the differential equations by numerically marching through time by a small time step and filling the pre-sized arrays after each time step. It also has embedded graphing commends that generate curves for size distribution, temperature and diameter time profiles after each run. The time step is set to 0.01 s and lowering it results in negligible change of the results.

CHAPTER 5: MODELING RESULTS

5.1 Comparison between the EES and the MATLAB models

The input size distribution data were taken from the average measured distribution in the adiabatic-wall experiment as presented in Figure 19. To get unbiased results, the full range of data was preserved although the distribution was likely skewed for diameters below 2.5 μm as discussed in section 3.1.1. Input mist and sink temperatures were averaged among all the runs, taken to be 20℃ and -20℃, respectively. The initial liquid water volume concentration Cv was averaged and corrected for a more realistic value, 3.5 ppm. The correction of Cv is discussed in the next chapter, section 6.1.

Figure 23 below shows the modeled size distributions from both the EES and the MATLAB model. The agreement is outstanding in all size bins with the maximum coefficient of variation of 0.03%. Such agreement can also be observed in the temperature and supersaturation time profiles (Figure 24 and Figure 25). This shows that the quasi-steady water vapor mass balance assumption made in the MATLAB model have minimal effect in accurately describing the physical processes.

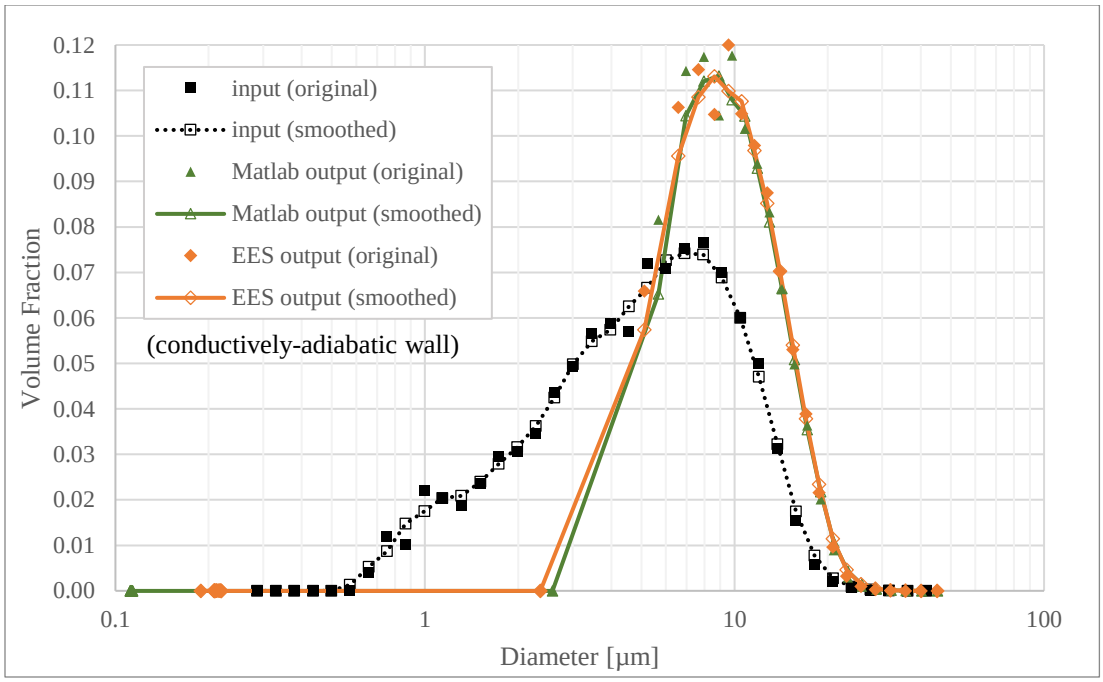

Figure 23. Droplet size distributions as calculated by EES and MATLAB models after 80 s radiative cooling under conductively-adiabatic wall condition. The input droplet size distribution (black dotted line) is the same as in Figure 19.

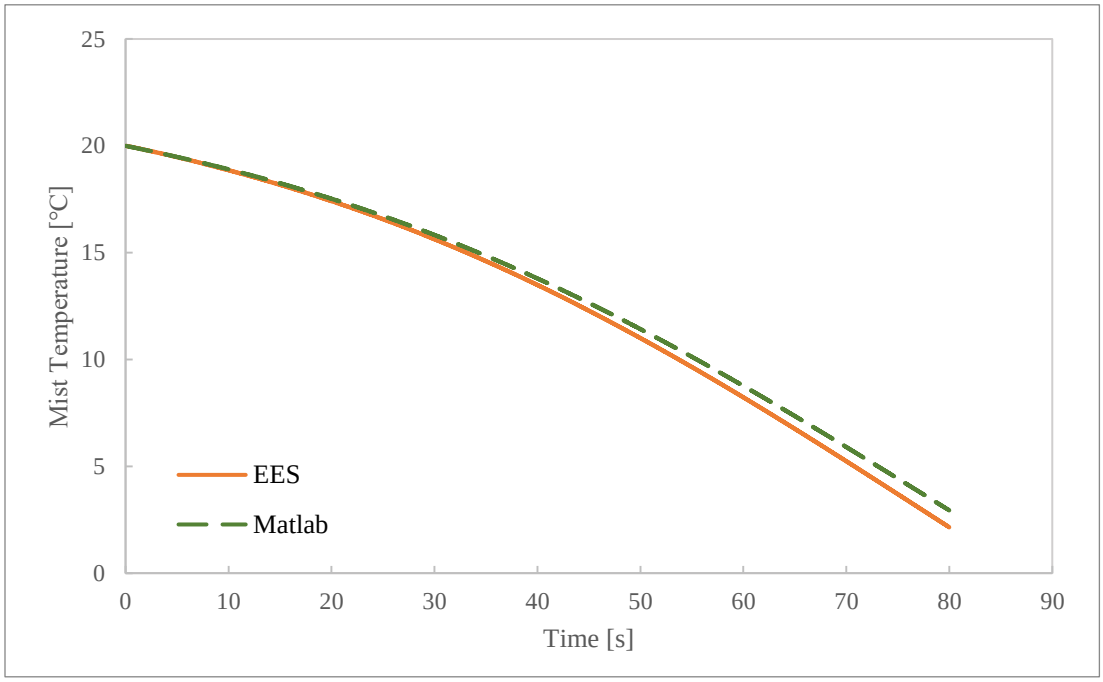

Figure 24. Mist temperature time profiles as calculated by EES and MATLAB models for 80 s radiative cooling under conductively-adiabatic wall condition.

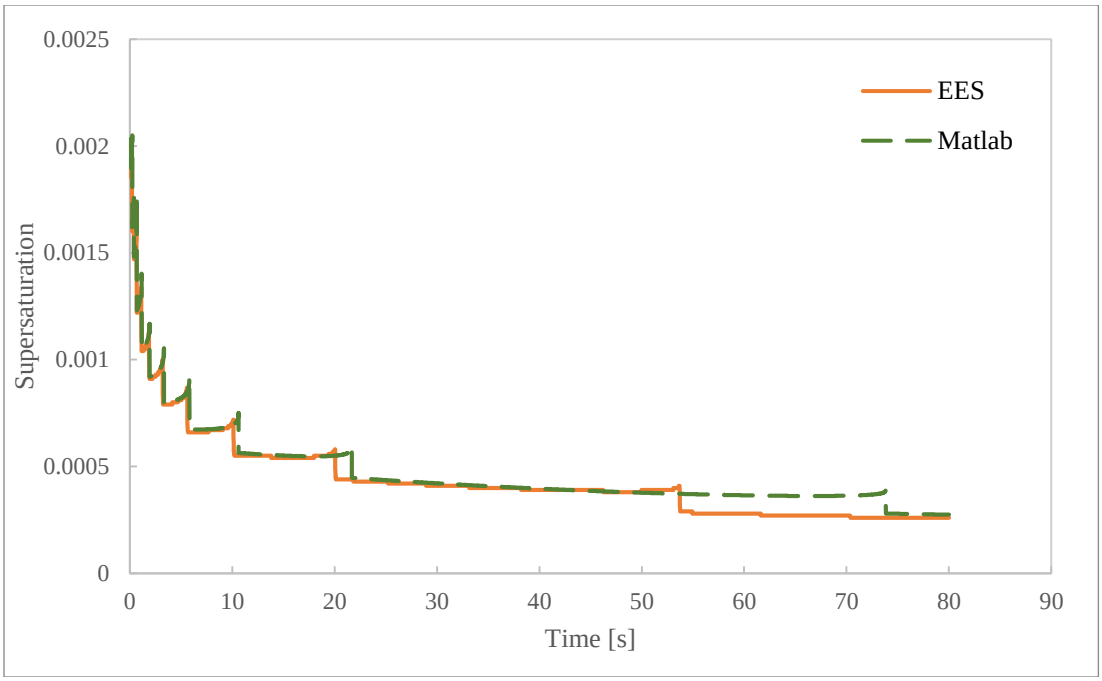

Figure 25. Supersaturation time profiles as calculated by EES and MATLAB models for 80 s radiative cooling under conductively-adiabatic wall condition.

The key advantage of the MATLAB code is its speed. While running the EES code to simulate the 80 s experiment takes around 12.5 hours, running the MATLAB code takes only about 20 seconds. The improvement in speed is mainly due to the approximations of quasi-steady water vapor mass balance that greatly simplify the algorithm. In addition, the step size in the EES code is 0.0001s while in the MATLAB code 0.01s. The MATLAB code takes a hundred times less steps which also reduces its computational time. It is possible to increase the step size (reduce the number of steps) but the possibility of getting terminating errors caused by drastic changes in values for some variables would increase. Other advantages of the MATLAB code include strong graphing capacity and easy initialization. However, the EES code also has its merits. Since less approximations are made in the equations, the EES code is believed to be more fundamental. As EES would allow relaxing the quasi-steady water vapor assumption and solving the unsteady water mass balance, it would be more accurate in situations when this was important. Also, more physical variables are preserved in the EES code, which allows the user to

trace and study any variable of interest through its time history. Hence, the MATLAB code and the EES code can be used to fulfil different purposes and/or in conjunction to confirm the results.

5.2 Parametric study

A parametric study was done with the MATLAB model to explore the variations of radiative sink temperature (T_{sink}) and liquid water volume concentration (Cv) and their effects on mist droplet size distribution, mist temperature and supersaturation. Note that T_{sink} here follows the definition in experimental sections, and is interchangeable with T_r as defined in section 4.2.

5.2.1 Cases with no radiative cooling

Before considering radiative cooling, let us look at the case where there is no radiative cooling, meaning that the sink temperature T_{sink} is equal to the initial mist temperature T_0. There is essentially no heat exchange of any form (conduction, convection or radiation) between the mist and the sink. In other words, any effects we see in the following discussion, any processes that occur, are a result of factors and equilibration internal to the mist. This will help set the stage for later discussion when equilibration due to external radiative non-equilibrium and associated variation of parameters is brought in.

First, a "warm" case is explored where T_{sink} is set to match T_0 at 20℃, and the initial droplet distribution is the same as presented in Figure 19. We select a few representative bins from the distribution and plot their diameter versus time for 80 s in Figure 26. Bins 5 to 13 all ultimately evaporate and disappear (meaning diameter reaches 0), with the smallest bin 5 disappearing very quickly within 1 s, whereas bins 7 to 13 grow briefly in size at first but eventually start to evaporate and disappear. The remaining bigger bins (bin 15 to bin 31, the largest bin in the distribution) grow slightly throughout 80 s by one to a couple of μm's.

The disappearance of bin 5 to 13 has to do with the Kelvin (curvature) effect, where equilibrium supersaturation, s_{eq}, is a function of droplet diameter, D_i, and i denotes the bin number as stated in section 4.2. Smaller droplets have higher saturation vapor pressures over their surface, needing higher equilibrium supersaturation $s_{eq}(D_i)$ to maintain their size. As D_i increases, $s_{eq}(D_i)$ reduces and approaches 0. The environment supersaturation s is determined by all droplets in the system, as calculated by Eq. (47). In a way, s is a mean of $s_{eq}(D_i)$ for all bins, whose value is between all $s_{eq}(D_i)$ as determined by the quasi-steady water vapor assumption. There will be a critical diameter D_{cr} that satisfies $s_{eq}(D_{cr}) = s$, and droplets of diameter D_{cr} will by definition be in equilibrium at the current environment, not growing or shrinking. For $D_i < D_{cr}$ (smaller droplets), $s_{eq}(D_i) > s$, the environment does not have high enough supersaturation to sustain the smaller droplets, so they will evaporate and eventually disappear. On the contrary, for $D_i > D_{cr}$ (larger droplets), $s_{eq}(D_i) < s$, they could survive and grow by diffusion (condensation).

The environment supersaturation s is plotted against time in Figure 27 (note the x-axis is now in log scale). It can be seen that despite the periodic jumps, s drops rapidly at the beginning (about 75% drop in the first 20 s), and the decrease slows down for the rest of the 80 s and s reaches around 0.0003 in the end. This is due to the model assumption of mass conservation for water in the system. With the finite water mass available s is constantly being perturbed by the evaporation and condensation of water, and the decreasing s means more water is condensed than is evaporated. As s drops in time, D_{cr} increases. This means some droplets that used to be larger than D_{cr} and hence would grow at first, could then start to evaporate once D_c increases to become larger than their diameters. The behavior of bins 7 to 13 could thus be explained this way. Note another assumption present in the model is the neglection of solute effect (Köhler theory), i.e. all droplets are made of pure water and there's no condensation nuclei present in the

system that can be activated. Should Köhler theory be considered, D_c could be significantly lower, allowing much smaller bins to be preserved.

If we compare Figure 26 with Figure 27, we can see at the disappearance of each of the bins from bin 5 to 13, a jump in supersaturation is observed; for example, the disappearance of bin 5 corresponds to the jump at 1 s, and the disappearance of bin 13 to the jump at 70 s. This is an artifact of the binning method used in the model, where droplets within a certain range of diameter are grouped into one bin and represented by the mean diameter of the range. In other words, droplets are monodispersed within each bin. Each of the jumps represent one bin (of the smallest diameter at the moment) being evaporated and hence an injection of water vapor that temporarily boosts *s*. Then *s* quickly drops down as one less small bin is present. In reality, the size distribution within a droplet assembly is continuous, so the supersaturation profile should mostly be smooth, without sharp transitions.

If we extend the residence time from 80 s to 600 s (10 min), we can see bin 15 also evaporates and disappears at 250 s (Figure 28), and the remaining larger bins grow steadily in size. The supersaturation time profile is not presented here; it shows similar characteristics as in Figure 27.

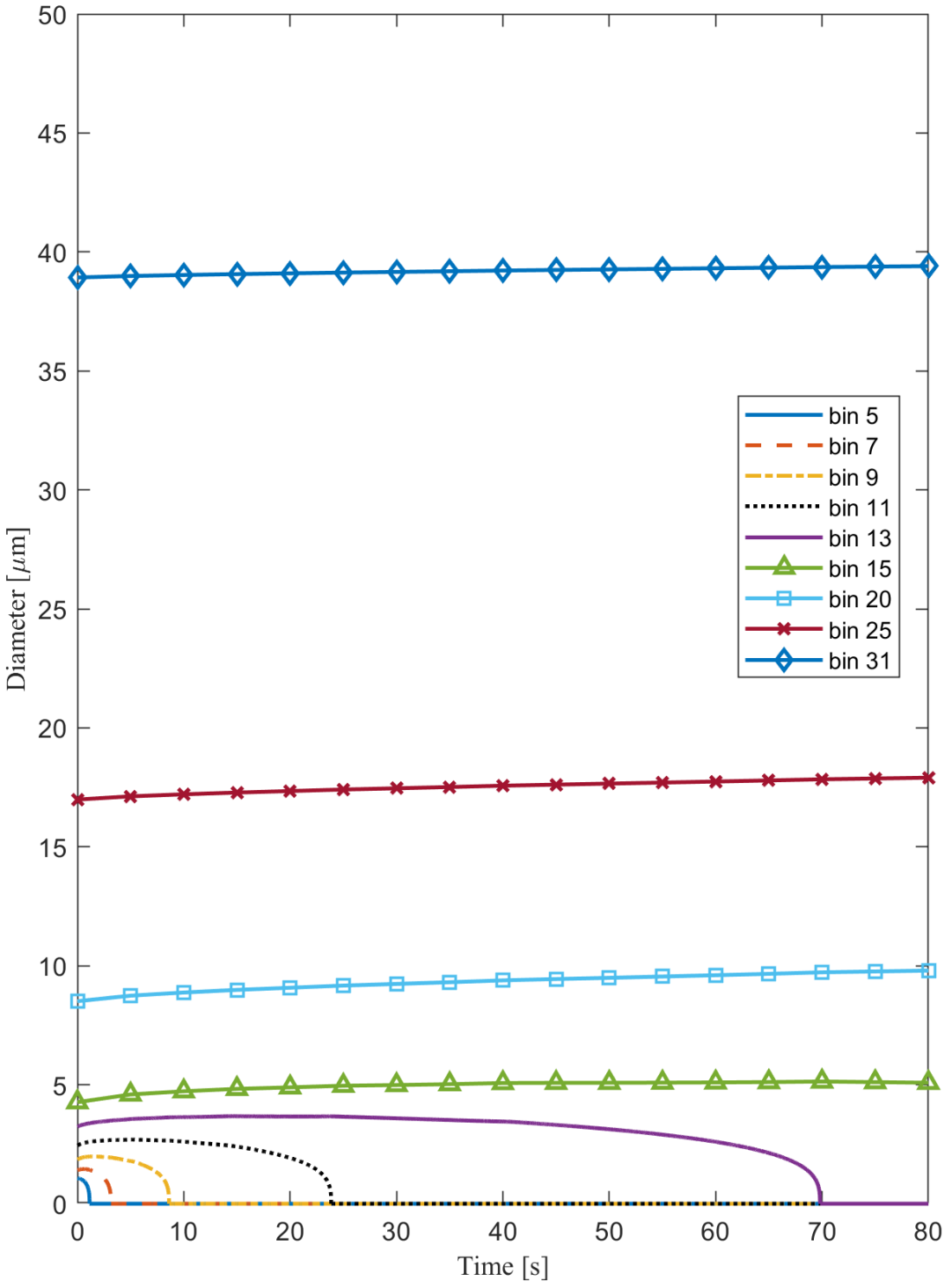

Figure 26. Selected bins time profiles for 0 to 80 s in the "warm" case under conductively-adiabatic wall condition and sink temperatures of 20°C (no cooling).

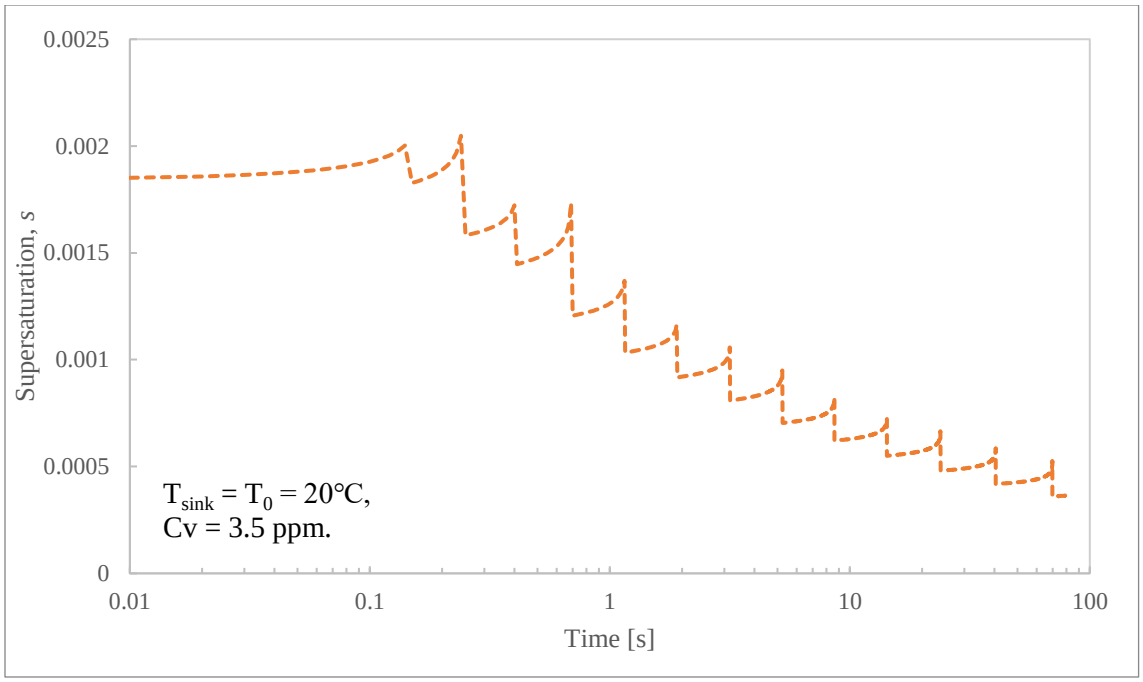

Figure 27. Supersaturation time profiles for 0 to 80 s in the "warm" case under conductively-adiabatic wall condition and sink temperatures of 20°C (no cooling).

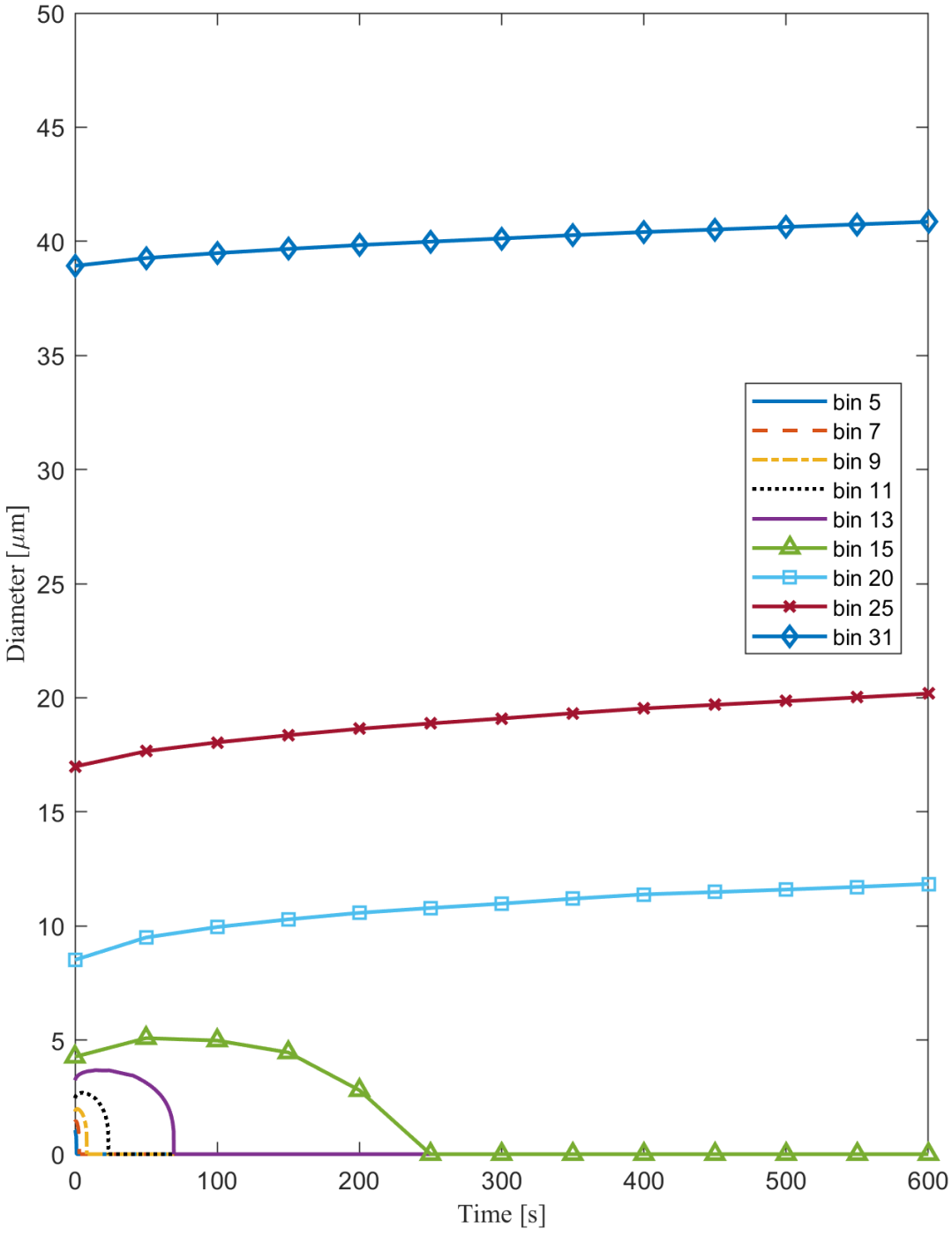

Figure 28. Selected bins time profiles for 0 to 600 s in the "warm" case under conductively-adiabatic wall condition and sink temperatures of 20°C (no cooling).

Figure 29 below plots the droplet size distributions at 0 s (initial distribution, input), 80 s and 600 s. As time progresses the distribution shifts towards the right (bigger droplets) and peaks higher (larger volume fraction). This agrees with the observations in Figure 26 and Figure 28, where more small bins are evaporated and larger bins keep growing in time. Figure 29 also suggests that the distribution gets narrower i.e. more monodispersed for longer time. This is similar to the classic textbook observation [3] about diffusion-limited cloud-droplet growth. However, in the textbook discussions, the environment supersaturation is usually assumed constant.

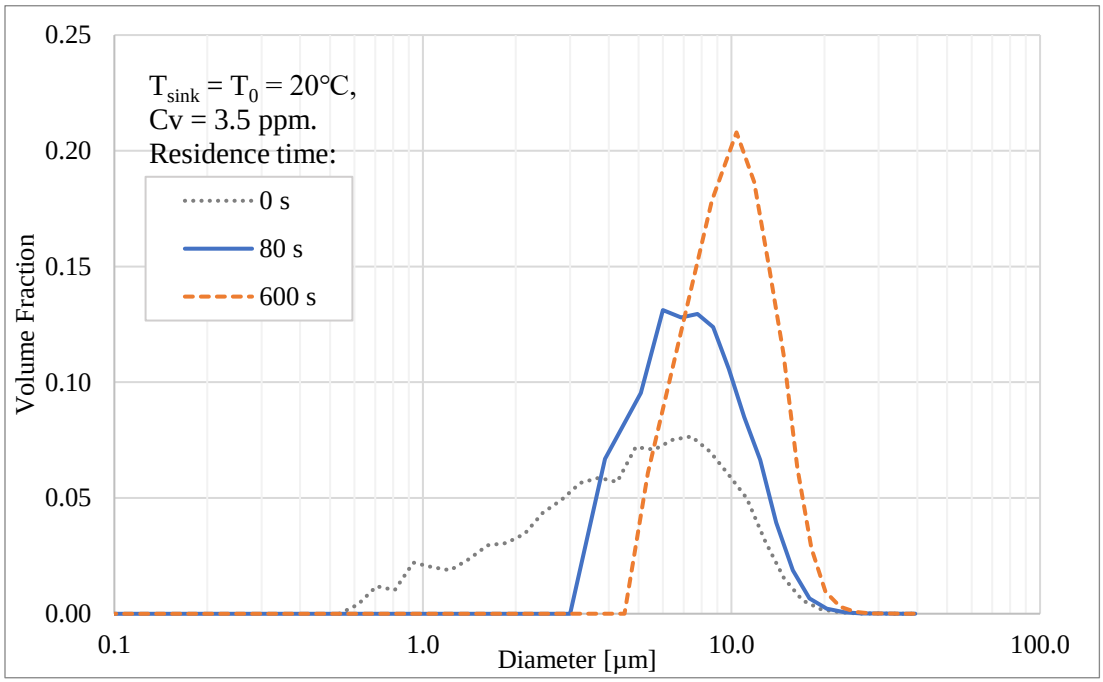

Figure 29. Droplet size distributions at 0 s, 80 s and 600 s for "warm" case under conductively-adiabatic wall condition and sink temperatures of 20°C (no cooling). The four-three moments (D_{43}) of the distributions are: 5.51 μm (0 s), 8.32 μm (80 s) and 11.70 μm (600 s).

To conclude, in this case where no external thermal effect is present, the droplet assembly tries to "equilibrate" on itself by evaporating smaller droplets while feeding the growth of bigger droplets, leading the droplet distribution to become larger and more monodispersed as time progresses. We name this phenomenon internal equilibration.

Next, T_0 is made to match T_{sink} at -20°C for a "cold" case with the initial droplet distribution the same as the "warm" case. Comparing the "cold" case with the "warm" case can inform us the effect of temperature on the internal equilibration.

The same set of bins are plotted against time for 600 s in Figure 30. Comparing with the "warm" case (Figure 28), one more bin (bin 15) is preserved, and the growth of bigger droplets is slower. This suggests that both the evaporation and condensation of water happen at a slower pace when the temperature is lower. This is an effect of the strong temperature dependence of vapor pressure. As temperature changes from 20 to -20°C, both vapor pressures of the environment ($P_{v,e}$) and near the droplets' surfaces ($P_{v,s}$) drop significantly, resulting in the absolute value of their difference ($P_{v,e}$ - $P_{v,s}$) also becoming much smaller. This difference is the driving force for water diffusing from a droplet surface into the vapor phase (evaporation) or from the vapor phase to the liquid-phase droplet surface (condensation) as determined by the sign, and its magnitude is proportional to the mass flux of diffusion as can be seen in Eq. (3). Therefore, lower temperature leads to smaller mass fluxes at a given time hence slower overall evaporation and condensation rates. The internal equilibrating effect is also present in the "cold" case (Figure 31) as the distribution moves to the right and grows higher as time progresses. However, the droplet growth is less significant, with less shifts towards right and lower peaks as compared to the corresponding curves in the "warm" case (Figure 29), as evidenced by the smaller values of D_{43} at a given time for the "cold" case compared with the warm case (see captions of Figure 31 and Figure 29, respectively). This reduction in the D_{43} value is another manifestation of the slower rate of diffusion-limited droplet growth due to lower temperature and lower water saturation pressure.

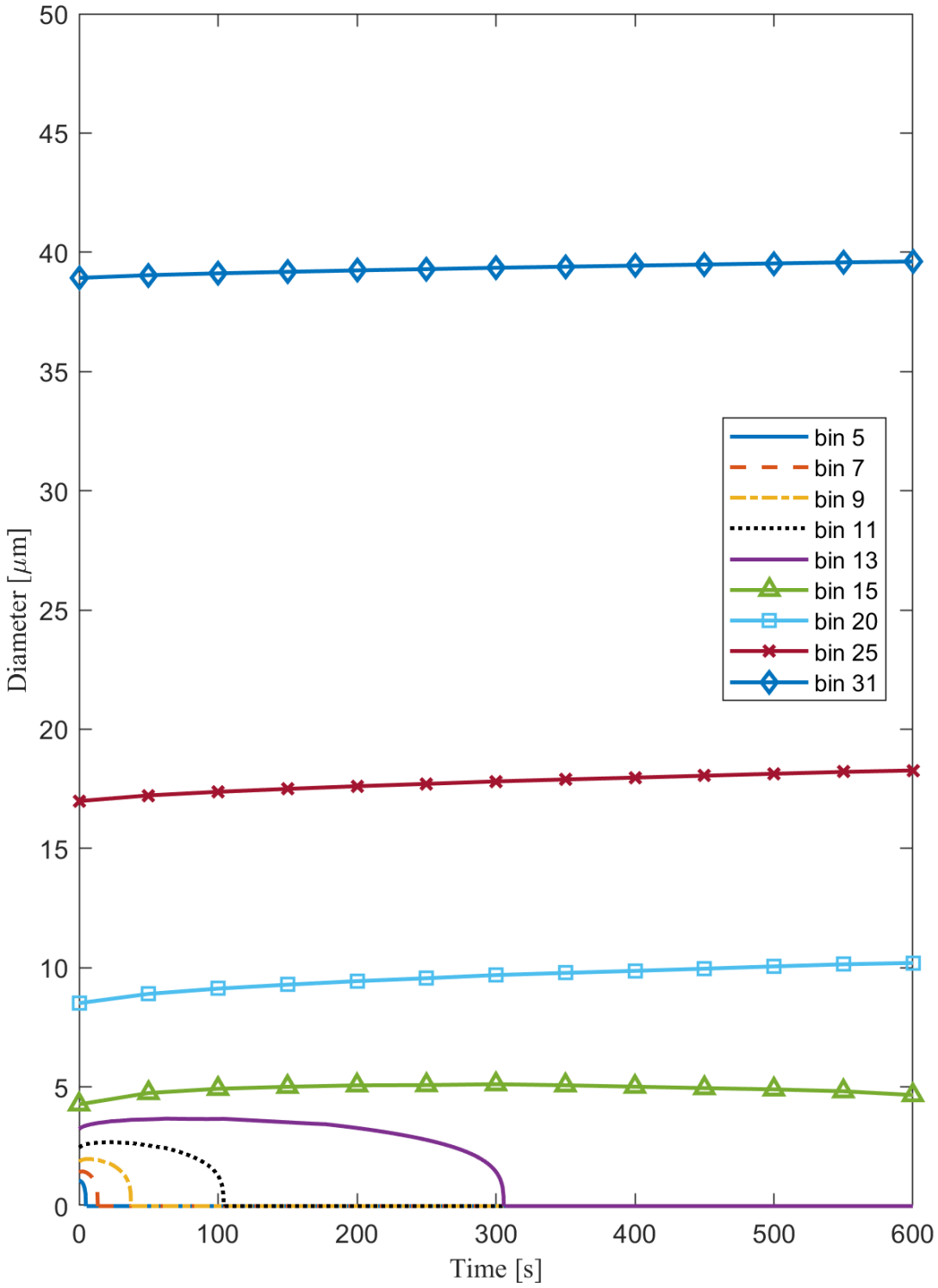

Figure 30. Selected bins time profiles for 0 to 600 s in the "cold" case under conductively-adiabatic wall condition and sink temperatures of -20°C (no cooling).

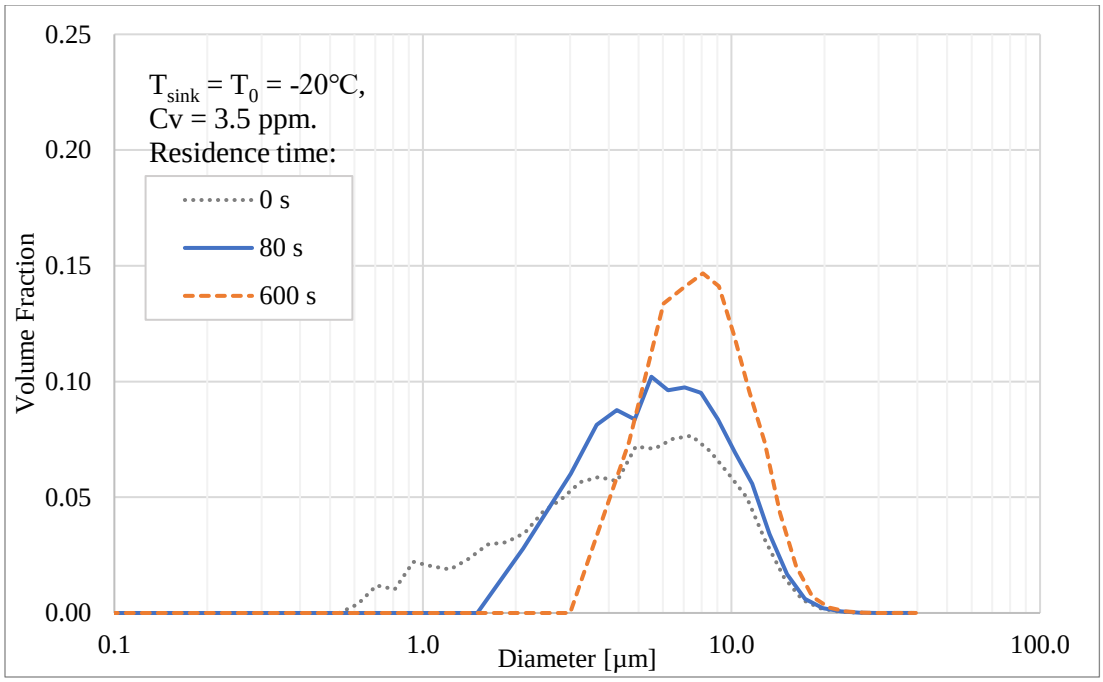

Figure 31. Droplet size distributions at 0 s, 80 s and 600 s for "cold" case under conductively-adiabatic wall condition and sink temperatures of -20°C (no cooling). The four-three moments (D_{43}) of the distributions are: 5.51 µm (0 s), 6.91 µm (80 s) and 9.03 µm (600 s).

To summarize, a mist or droplet assembly of an arbitrary droplet-size distribution goes through a process of internal equilibration even when no heat transfer is present between the mist and external environment. During this process, smaller droplets evaporate and disappear, and the water vapor made available by these evaporated droplets feeds the growth of larger droplets through condensation. As a result, the droplet distribution becomes more and more monodispersed at larger diameters. Temperature influences the degree of such equilibration by determining the rate of mass transfer via diffusion of water. The lower the temperature, the slower the overall rates of evaporation and condensation, and as a result the less internal equilibrating effect within a given time period.

With this ground work on internal equilibration, we now add in external heat transfer (radiation) to the mist and explore the changes in mist temperature, droplet sizes and supersaturation.

5.2.2 Sink temperature, T_{sink}

Keeping residence time at 80 s, initial mist temperature at 20℃ and liquid droplet volume concentration at 3.5 ppm, T_{sink} is varied from -50℃ to 20℃, with T_{sink} = 20℃ matching the "warm" case in the previous discussion.

Mist temperature time profiles for varying sink temperatures are presented in Figure 32 below. For T_{sink} < 20°C, the temperature of the mist decreases towards the respective T_{sink}, which is the lower limit the mist temperature could reach if more time were given. Here -50℃ was chosen to be the lowest T_{sink} since homogeneous nucleation (freezing) is likely to happen as mist temperature approaches -30℃, a phenomenon that is not considered in the current model.

The rate of temperature decline (absolute value of the slope) increases as the sink temperature goes down. This can be explained by referring to the differential equation of nondimensionalized temperature (Eq. (40)) that determines the rate of decrease in temperature. As discussed in modeling methods, the slope is determined by the inverse of the characteristic time, t_{rc}, which is the time for the temperature to drop 1-1/e (~ 63%) of its total possible change. The larger the t_{rc}, the longer it takes for the mist to cool, i.e. the slower the temperature drops. The characteristic time t_{rc} has a strong temperature dependence mostly because of two important factors: h_r and H / Ψ. The radiative heat transfer coefficient h_r positively correlates with temperature T by its definition (Eq. (24)). The parameter ratio H / Ψ appears to have an explicit T^{-3} temperature dependence; however, the saturation vapor pressure $P_{s,e}$ in the numerator has an even stronger positive dependence on temperature (around T^5 temperature dependence based on the curve fit used in the model) ; as a result, H / Ψ also turns out to be positively dependent on temperature. This gives t_{rc} a positive correlation with temperature. The colder the mist, the smaller the t_{rc} and the faster the mist cools. This well agrees with the observation in Figure 32.

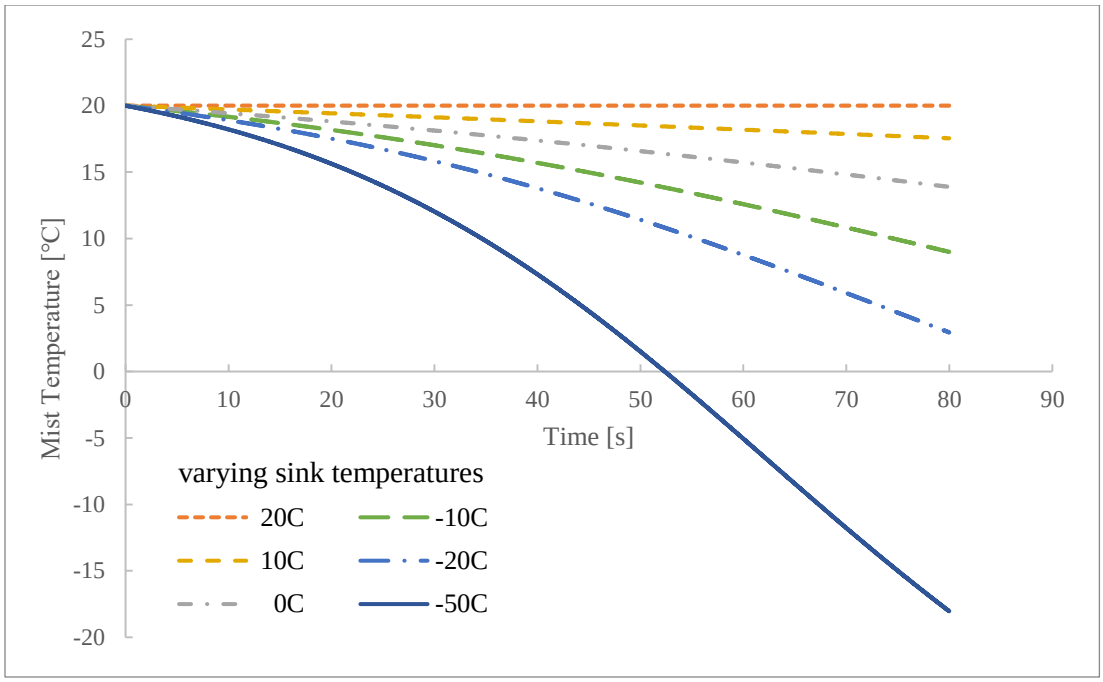

Figure 32. Mist temperature versus time for 80 s of radiative cooling under conductively-adiabatic wall condition and varying sink temperatures from -50°C to 20°C.

Figure 33 shows the diameter of selected bins versus time at T_{sink} = -20°C. Similar to the "warm" case (Figure 26), bins 5 to 11 evaporate while bins 13 to 31 grow in size. This means the effect of internal equilibration is still present, reflected especially in the similarity of the evaporated bins' profiles with and without radiative cooling. However, the equilibration is now influenced by the external factor of radiation, shown in the faster growth of the larger droplets as compared to the "warm" case. This external equilibration is a clear indication of radiation-augmented droplet growth. With Figure 33, one can almost predict the trend of size distributions plotted in Figure 34 after 80 s of radiative cooling. As sink temperature goes down, more radiative cooling is added, and the size distributions are shifted more towards the right (bigger droplets). The rightward-shifting trend is also reflected in the four-three moments (D_{43}) of the distributions as presented in Table 3 below.

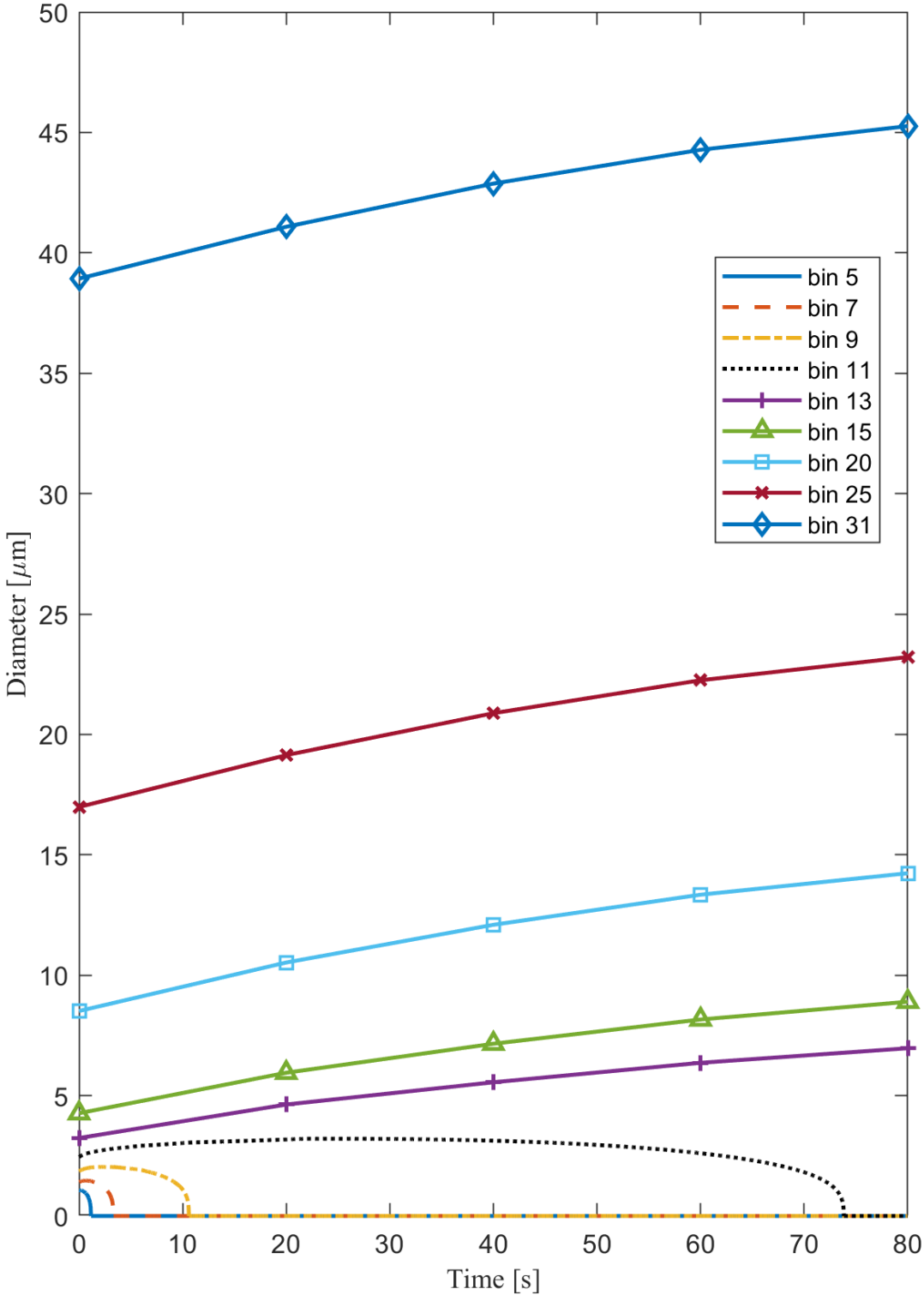

Figure 33. Selected bins time profiles for 0 to 80 s under conductively-adiabatic wall condition and sink temperatures of -20°C.

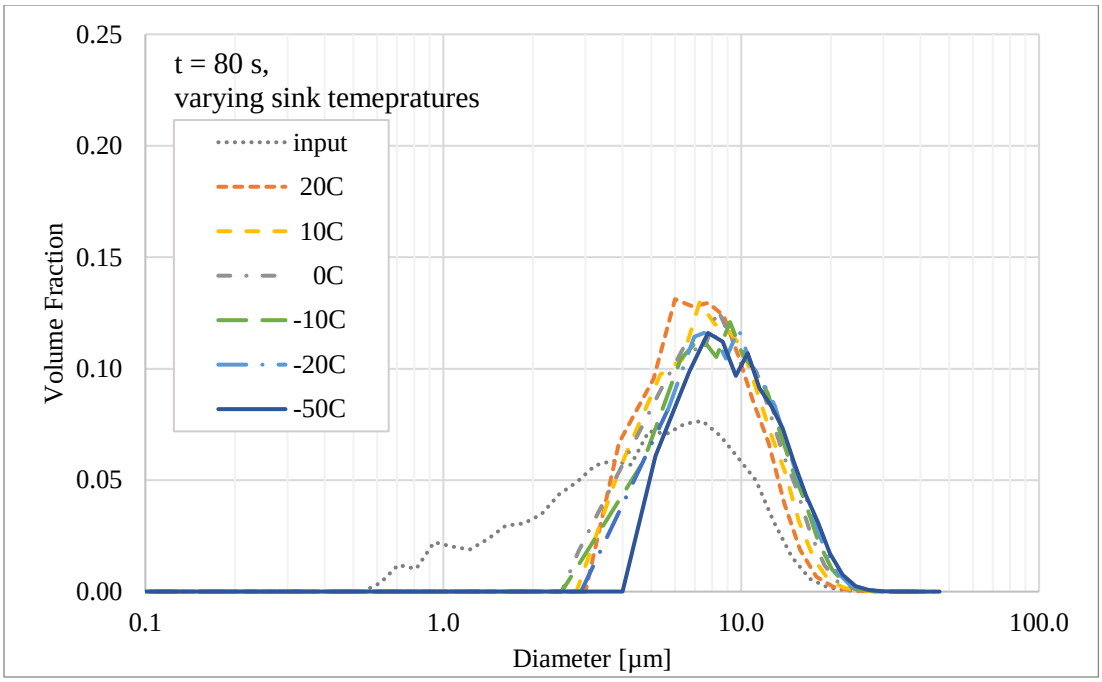

Figure 34. Droplet size distributions with varying radiative sink temperatures from -50°C to 20°C, after radiative cooling of 80 s under conductively-adiabatic wall condition. The input droplet size distribution (black dotted line) is the same as in Figure 19.

Table 3. Four-three moments (D_{43}) and their percentage increase for size distributions in Figure 34.

	T_{sink}	D_{43}	% change
Before cooling	-	5.51 μm	(base)
After cooling	20 °C	8.32 μm	+ 51%
	10 °C	9.05 μm	+ 64%
	0 °C	9.71 μm	+ 76%
	-10 °C	10.16 μm	+ 84%
	-20 °C	10.59 μm	+ 92%
	-50 °C	10.75 μm	+ 95%

To observe the effect of radiation-influenced external equilibration on a longer time scale, the residence time is extended to 600 s. The very cold case T_{sink} = -50°C is excluded in the discussion below to avoid the possibility of freezing. By observing the temperature profiles (Figure 35) it can be seen that in all cases with radiative cooling mist temperatures approach the respective sink temperatures at the end of 600 s. When infinitesimal difference is achieved between the mist and sink temperatures, negligible radiation is exchanged between the mist and the sink, which means for the rest of the time the mist droplet assembly will be subject to the

effect of internal equilibration only. We now focus on T_{sink} = -20°C to examine this statement. Figure 36 plots selected bins' diameters versus time for T_{sink} = -20°C, where (a) shows the whole period of 600 s, and (b) – (d) zoom in to the first 400 s, 200 s and 80 s respectively. At the first 80 or 200 s (c and d), larger droplets exhibit noticeable growth. This time period corresponds with rapid temperature decrease as shown in Figure 35, where radiation-influenced external equilibration is playing a role. After 200 s, the rate of growth slows down significantly, and the bins behave similarly to the "cold" case (Figure 30). This is an indication that the mist is now under the effect of almost purely internal equilibration, where the distribution would become more monodispersed but the growth rate slows down. The same process would be experienced by all the radiative cooling cases, so one can speculate that all distributions after 600 s of cooling would come towards stacking (monodispersed), with T_{sink} = 10°C peaking at the highest and T_{sink} = -20°C at the lowest, due to the temperature and saturation pressure effect on internal equilibration. The speculation is readily verified when size distributions are plotted of all cases after 600 s in Figure 37.

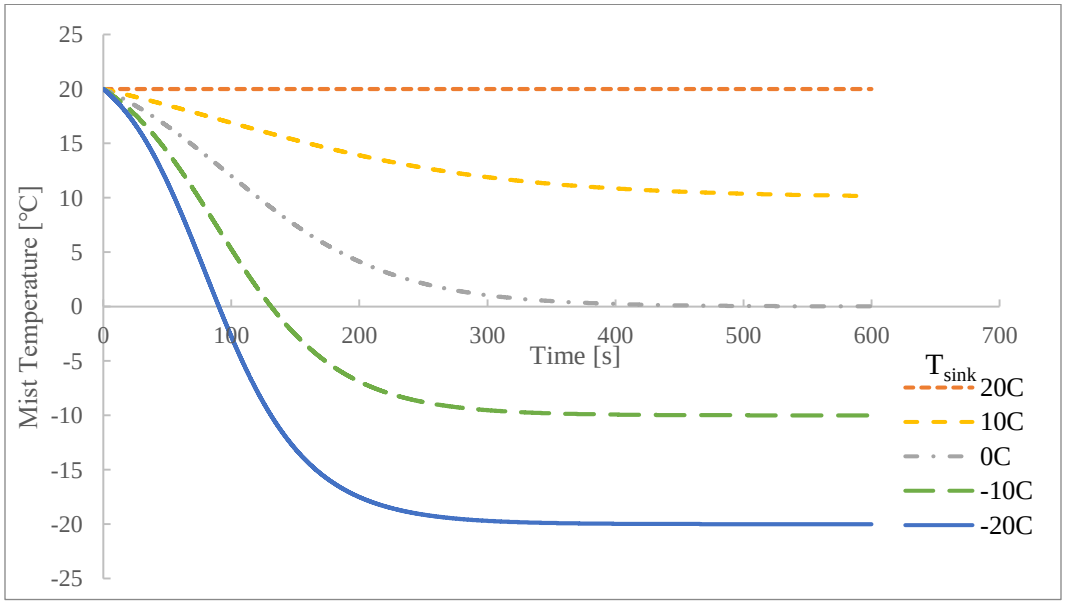

Figure 35. Mist temperature versus time for 600 s of radiative cooling under conductively-adiabatic wall condition and varying sink temperatures from -20°C to 20°C.

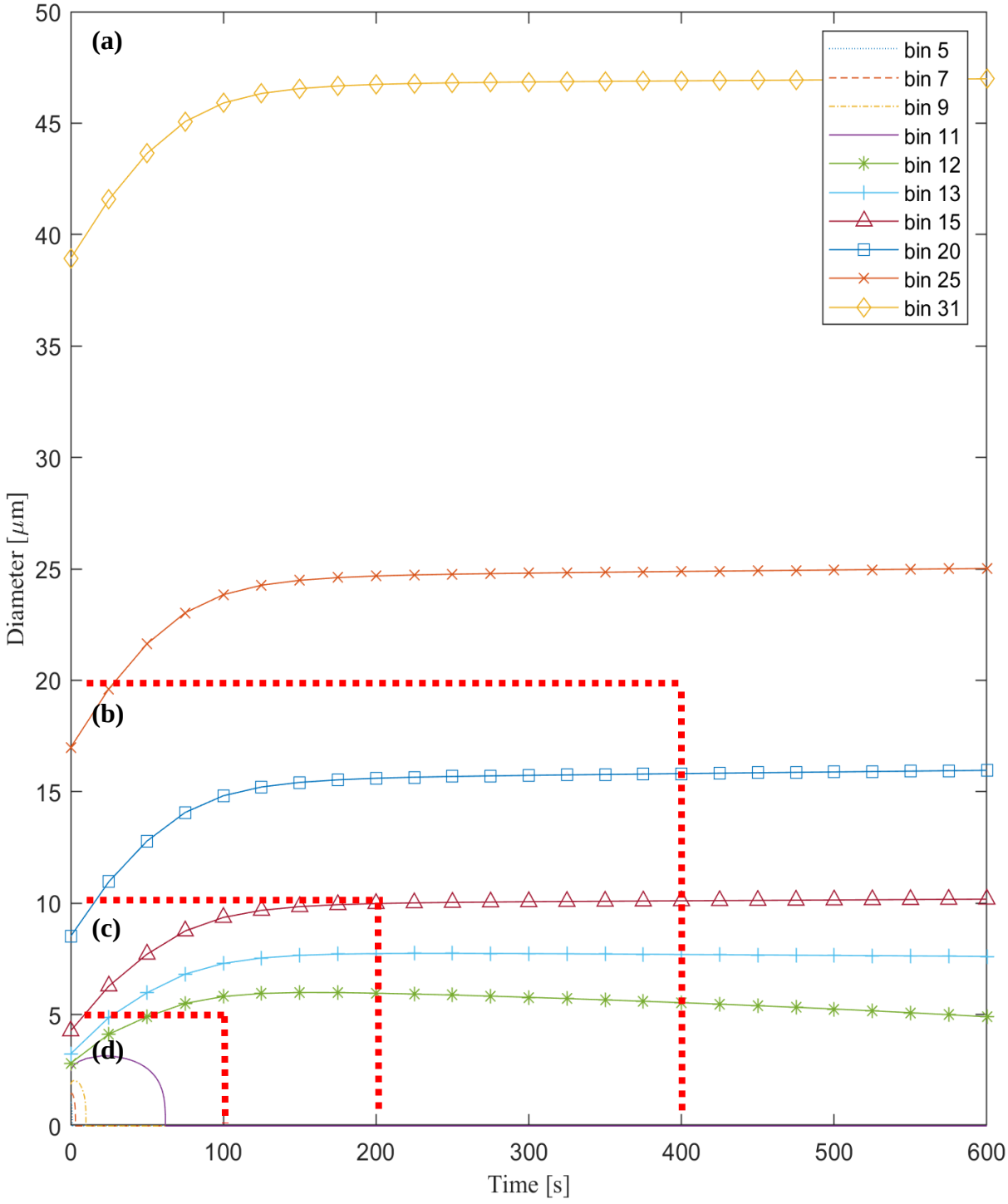

Figure 36. Selected bins time profiles for (a) 0 to 600 s, (b) 0 to 400 s, (c) 0 to 200 s and (d) 0 to 80 s of radiative cooling under conductively-adiabatic wall condition and sink temperatures of -20°C.

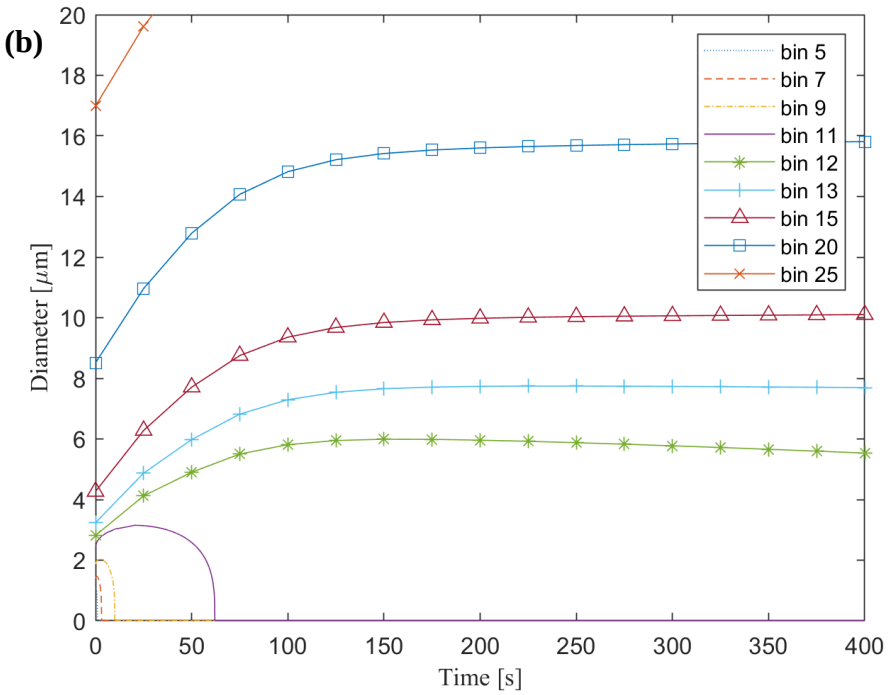

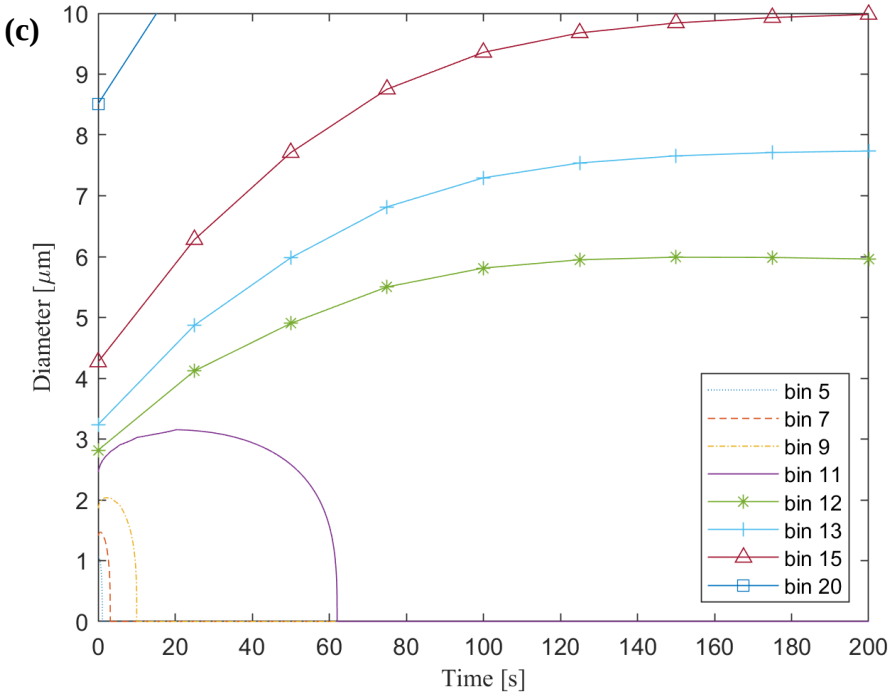

Figure 36 cont.

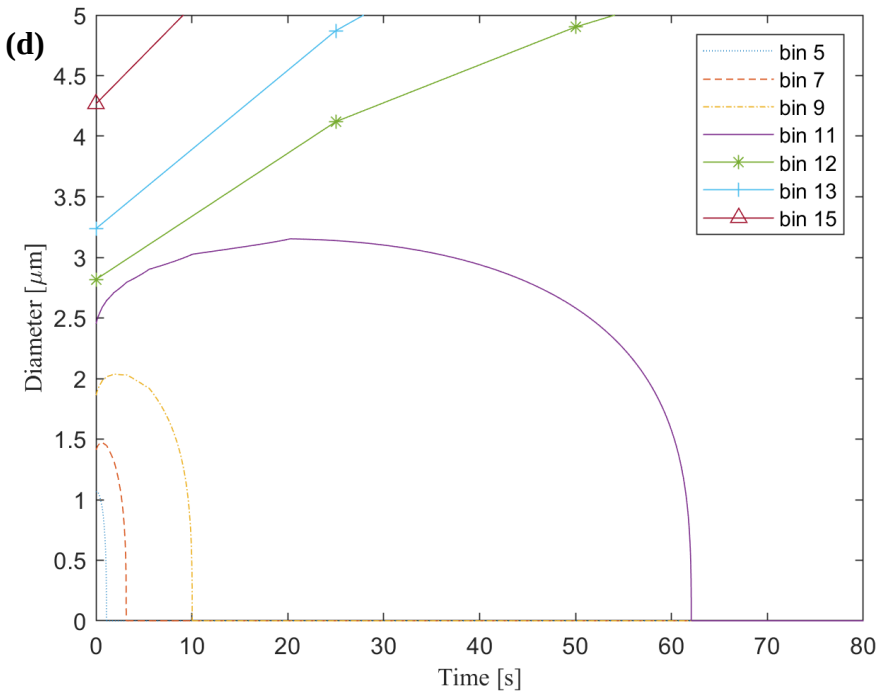

Figure 36 cont.

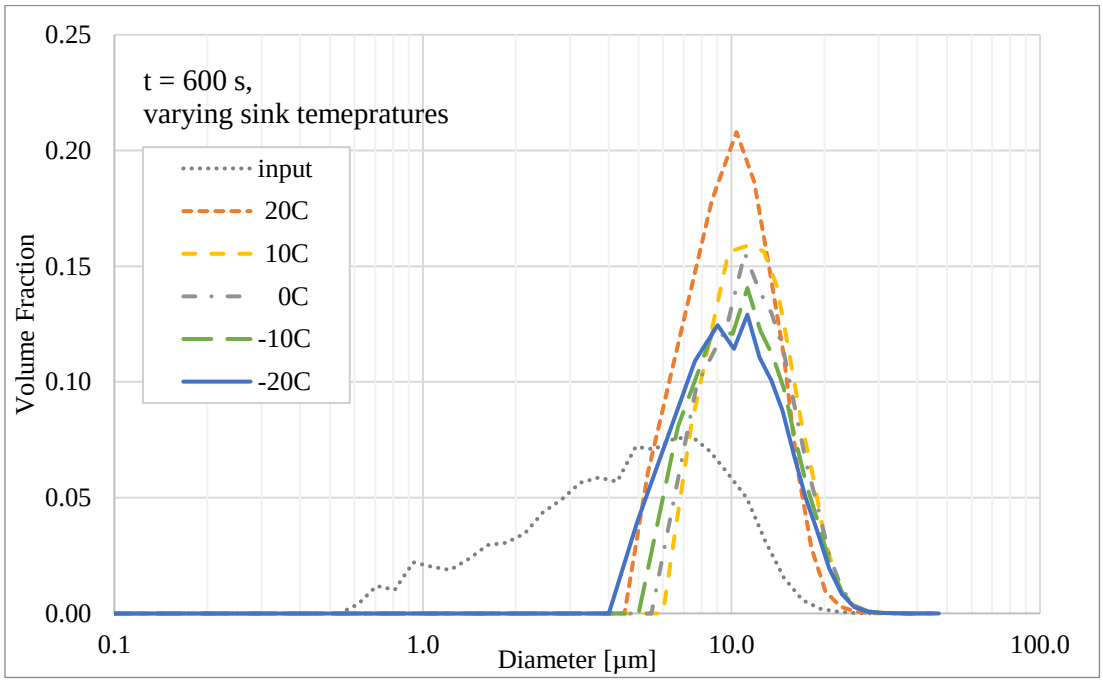

Figure 37. Droplet size distributions with varying radiative sink temperatures from -20°C to 20°C, after radiative cooling of 600 s under conductively-adiabatic wall condition. The input droplet size distribution (black dotted line) is the same as in Figure 19.

Supersaturations are plotted versus time for varying sink temperatures in Figure 38. For clarity of the figures only T_{sink} = -50℃, -20℃, 0℃, and 20℃ are shown and (b) shows the same data as (a) on a logarithmic x-axis to better resolve changes in earlier stage of the process. In all cases the supersaturation profiles are remarkably similar, where they drop rapidly at the beginning (about 75% drop in the first 20 s) and flatten out to around 0.0003 till the end of 80 s. This reflects the rapid growth of most droplets happening at the beginning, as the curvature effect becomes less significant with more droplets of larger diameter.

One may notice in Figure 38(b) that the lower the sink temperature the higher supersaturation at the start, despite having exact same initial mist temperature and size distribution. This is because of the approximation employed to simplify the model in the calculation of supersaturation (Eq. (46)). The characteristic diameter for curvature effect, D_c, is calculated with respect to T_m, the arithmetic mean of the initial and final mist temperatures. The lower the sink temperature, the smaller the T_m, the larger the D_c hence the larger the initial supersaturation. The actual initial supersaturation in all cases should equal the one calculated for T_{sink} = 20℃, which is 0.0018. The maximum discrepancy caused by this approximation among the cases tested is within 7%. If desired, the approximation in temperature can be substituted with the actual temperature that changes with time to minimize the error.

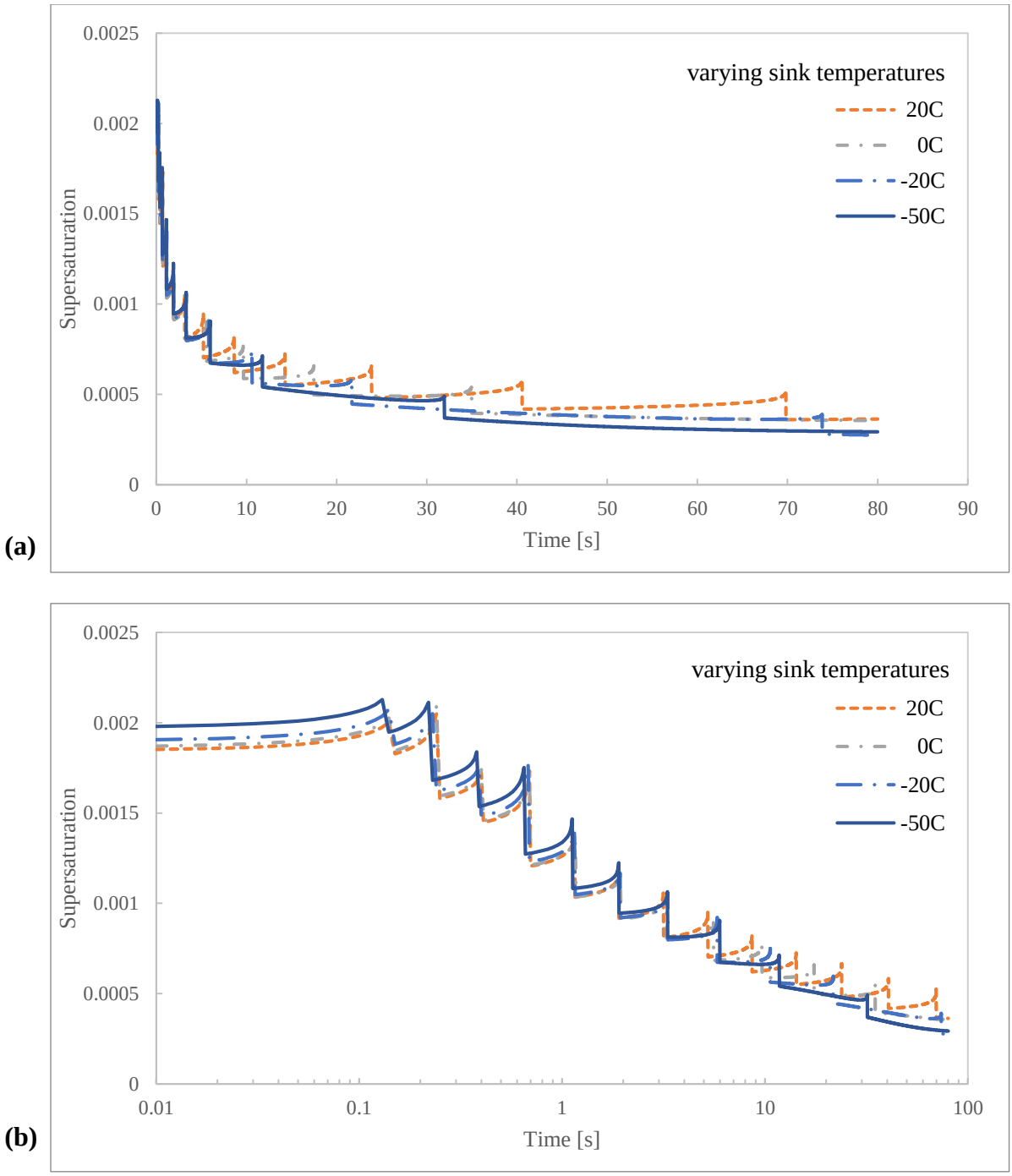

Figure 38. Supersaturation versus time on (a) linear x-axis and (b) logarithmic x-axis for 80 s of radiative cooling under conductively-adiabatic wall condition and varying sink temperatures from -50°C to 20°C.

As a conclusion, the presence of radiation affects the equilibration externally by growing larger droplets at a faster rate, making the size distribution shift more towards the right. The stronger the radiative cooling the more pronounced the external equilibration. However, the

external equilibration dies down as mist temperature approaches sink temperature, and afterwards internal equilibration dominates the dynamic of distribution, and is subject to the temperature and saturation pressure effect.

In the next section, with the presence of radiation, liquid water volume concentration, Cv, a parameter internal to the mist distribution is varied to examine the interaction between internal and external equilibrations.

5.2.3 Liquid water volume concentration, Cv

In this section, Cv is varied from 0.1 ppm to 100 ppm while keeping T_{sink} = -20°C and residence time at 80 s. The input size distribution remains unchanged, following the measurement results as shown in Figure 19; however, as Cv increases the more liquid volume (fv_i) is in each size bin. Here fv_i follows the definition in the modeling section.

Temperature profiles are presented first in Figure 39. The mist cools significantly faster as Cv increases. In the case of Cv = 100 ppm, the mist temperature reaches within a fraction of a percent difference with the sink temperature within 30 s, whereas for Cv = 0.1 ppm the mist barely cools by a fraction of a degree even after 80 s. We can again look for the explanation in the parameter t_{rc}. According to Eq. (42), t_{rc} relates to fv_i through the Plank mean absorption-emission coefficient K_{a_p}, as defined in Eq. (26). Increasing fv_i increases K_{a_p} and hence reduces t_{rc}, which means mists of higher Cv would cool much faster and approaches the limit of no radiative external equilibration much quicker. On the other hand, since Cv only affects the temperature profile, it does not affect the internal equilibration process as mist temperature under internal equilibration is always constant regardless of Cv. Based on the earlier discussion, one can expect Cv = 100 ppm to experience a very short period of radiation-augmented growth and quickly enters the internal equilibration regime, whereas Cv = 0.1 ppm will be dominated by

radiation augmentation and external equilibration. Is this true? We will test our speculation by plotting diameter versus time for the two limiting cases, Cv = 100 and 0.1 ppm.

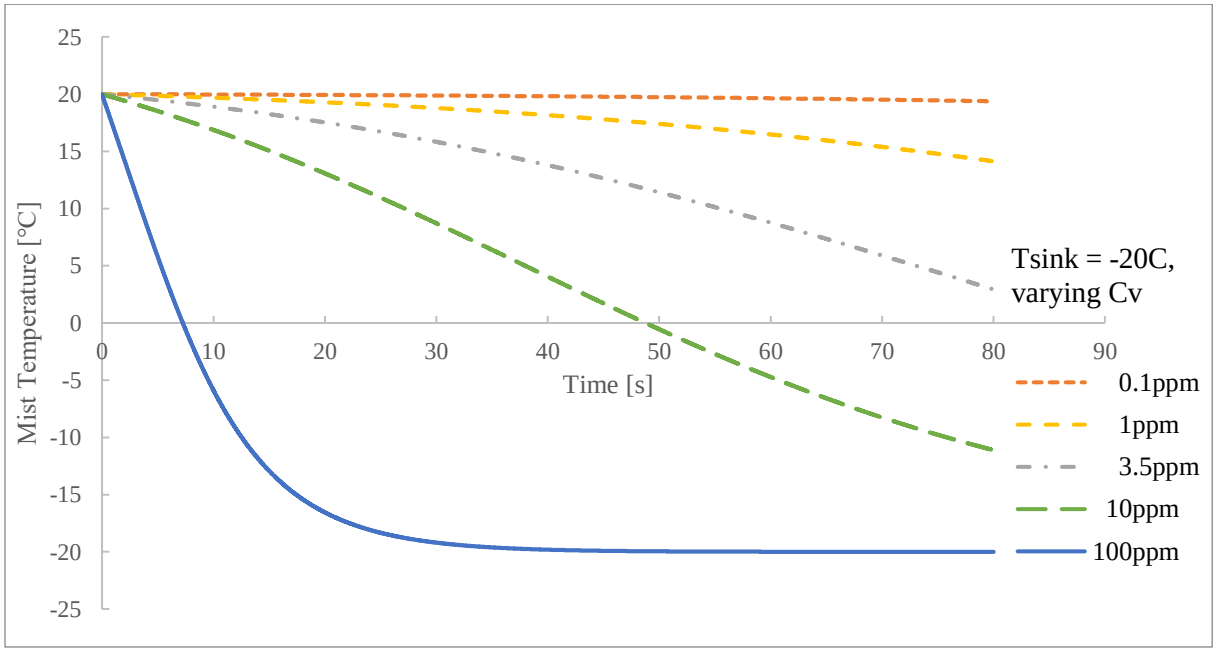

Figure 39. Mist temperature versus time for 80 s of radiative cooling under conductively-adiabatic wall condition and sink temperatures at -20°C, with varying liquid water volume concentration from 0.1 ppm to 100 ppm.

Diameter profiles of selected bins for Cv = 100 ppm and 0.1 ppm are presented in Figure 40 and Figure 41, respectively. Notice the remarkable similarity between Figure 40 and Figure 30, the diameter versus time plot for the "cold" case, except for the initial 20 s. This is convincing evidence that external equilibration is effective only at the early stage for Cv = 100 ppm and the mist droplets quickly transition into internal equilibration. Figure 41 on the contrary shows consistently significant radiation-assisted growth, as the growing droplets' profiles are almost straight lines. We can readily translate these observations into the size distribution curves as presented in Figure 42, where the smaller the Cv the more rightwards-shifting of the curves, and for Cv = 100 ppm, the distribution looks close to identical to the "cold" case at 80 s cooling (Figure 31).

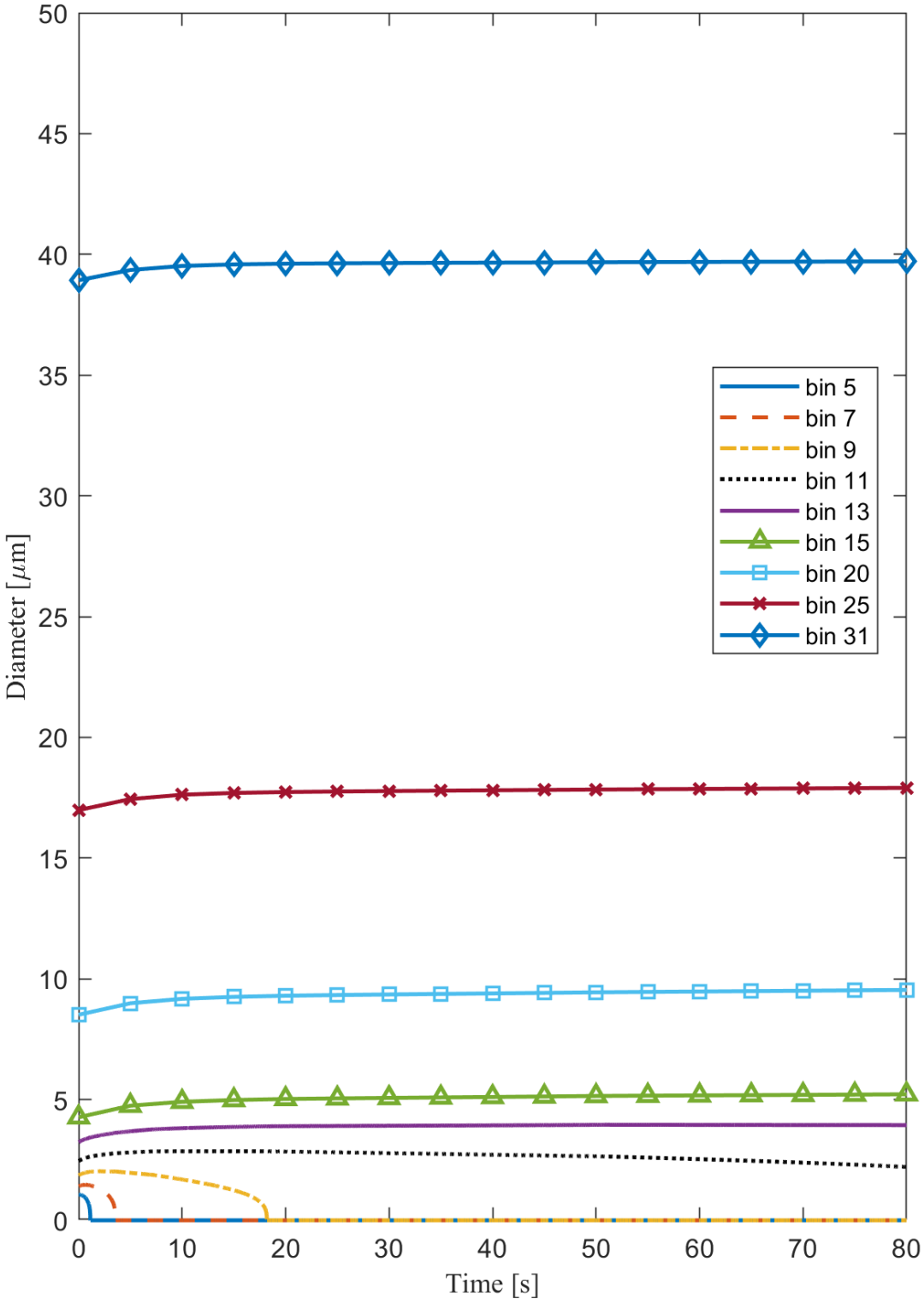

Figure 40. Selected bins time profiles for 80 s of radiative cooling with initial Cv = 100 ppm under conductively-adiabatic wall condition and sink temperatures of -20°C.

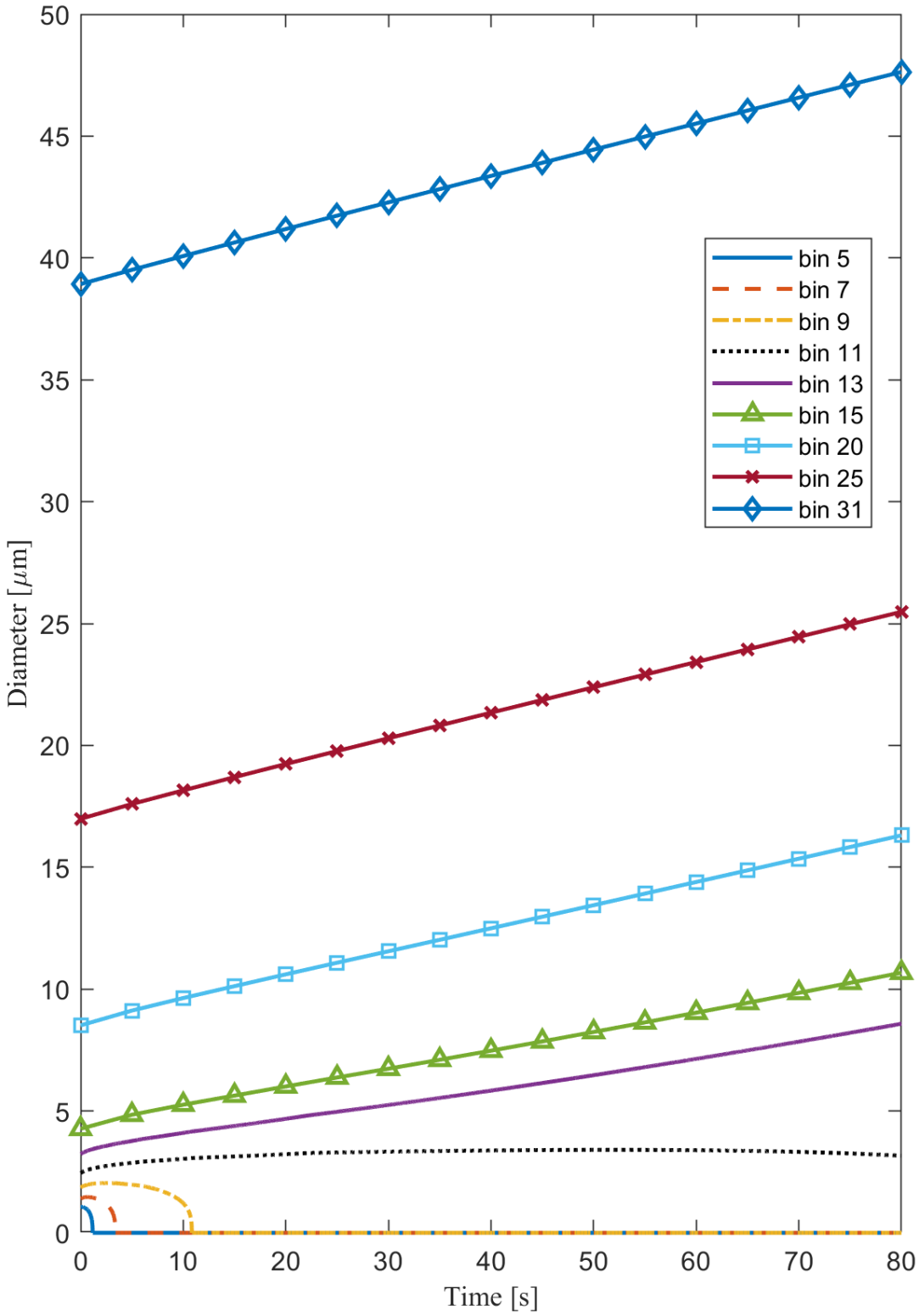

Figure 41. Selected bins time profiles for 80 s of radiative cooling with initial Cv = 0.1 ppm under conductively-adiabatic wall condition and sink temperatures of -20°C.

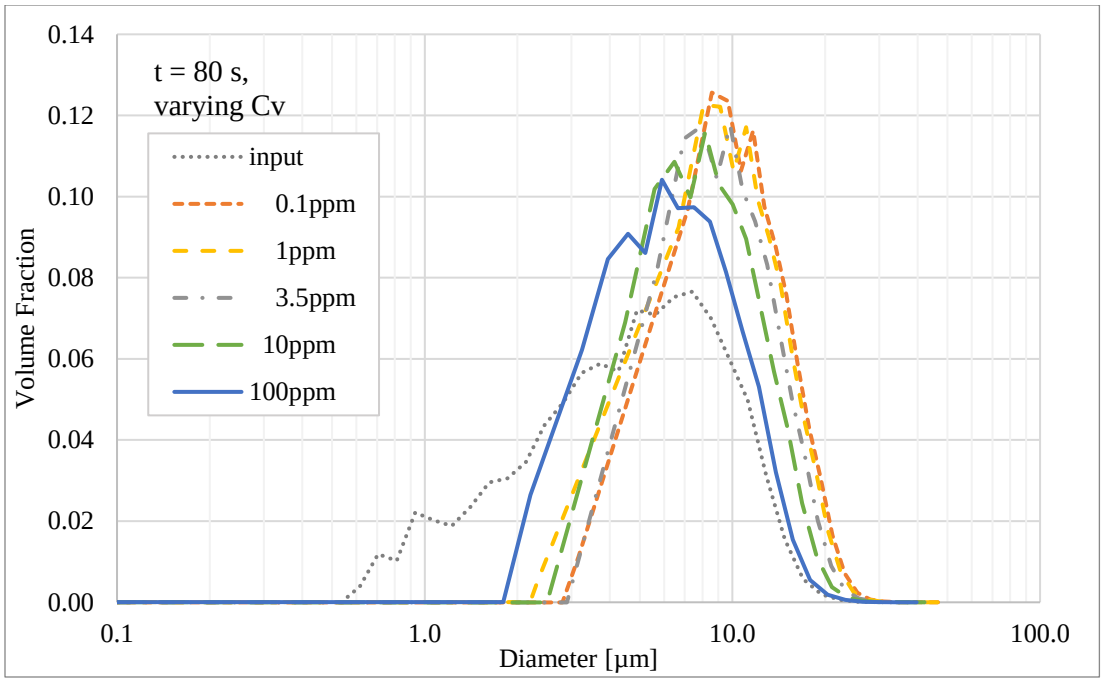

Figure 42. Droplet size distributions with varying liquid water volume concentration from 0.1 ppm to 100 ppm, after radiative cooling of 80 s under conductively-adiabatic wall condition and -20°C sink temperature. The input droplet size distribution (black dotted line) is the same as in Figure 19.

To conclude, the value of Cv affects the mist's sensitivity to radiation-influenced external equilibration. Higher Cv makes the mist cool faster, but less sensitive to external equilibration. This allows internal equilibration to quickly take over and become dominant, subject to the temperature and saturation pressure effect. Thinner mist (lower Cv) does not cool as efficiently but is very sensitive to radiation augmentation, shifting the size distribution towards larger droplets, the manifestation of a more predominant external equilibration.

CHAPTER 6: CORRELATING MODELS AND EXPERIMENTS

6.1 Comparison between the modeling and the experimental results

The modeling and experimental droplet size distributions after radiative cooling are plotted in Figure 43 below (because of the close agreement between the two models only EES results are shown for clarity). The size distribution from the models are in bulk agreement with the experiments, showing droplet growth in both increased diameter (distributions shifting to the right) and increased volume fraction for bigger droplets (distributions peaking higher), while smaller droplets are suppressed (experiments) or completely removed (models). This trend also agrees with the results presented in [7], [14]. However, measurements from the experiments show more significant droplet growth in size (diameter), while the models predict less growth in size but higher volume fraction of droplets between 5-12 μm. Another discrepancy between the experimental and modeling results is the behavior of the smaller droplets. Model calculations show droplets smaller than 2.5 μm are evaporated entirely to feed the growth of bigger droplets, while measurements still indicate presence of those droplets although of reduced volume fraction. Such differences in size distributions are also reflected in the D_{43} values, where the models predicted D_{43} to grow from 5.5 to 10.6 μm but the measurements showed growth to 8.4 μm after 80 s of radiative cooling.

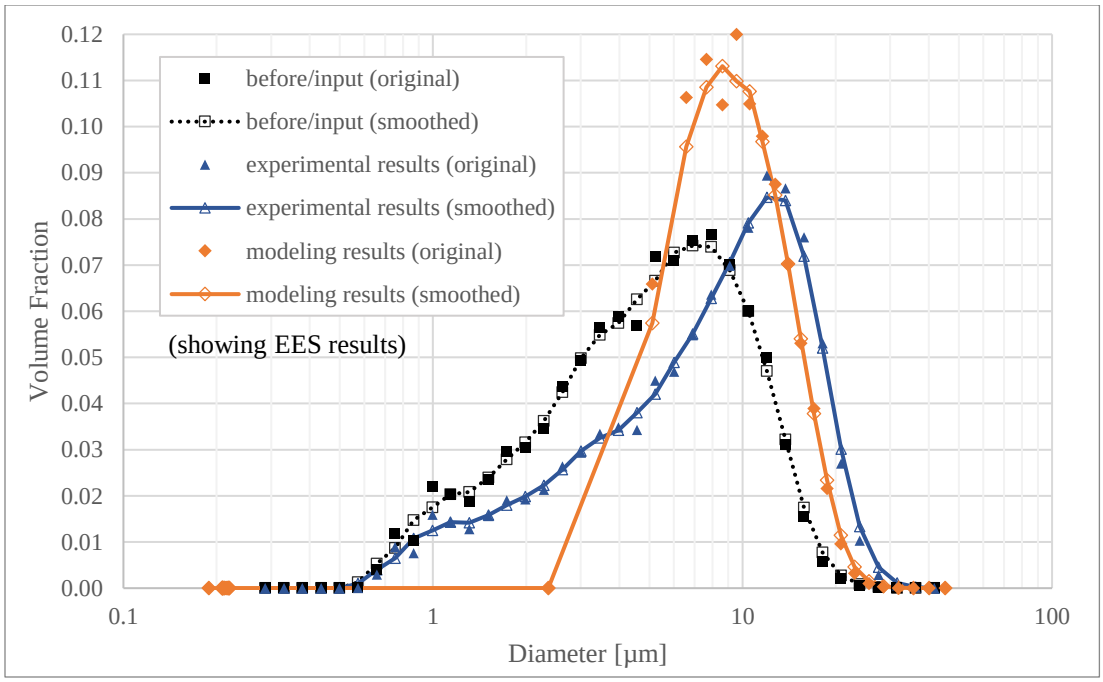

Figure 43. Droplet size distributions after radiative cooling of 80 s under conductively-adiabatic wall condition and -20°C sink temperature as measured in experiments (triangle, blue) and as predicted by the EES model (diamond, orange).

The mist temperature time profiles as predicted by the models are shown in Figure 44. The discrete points (since only before and after cooling data are available) show the measurement results from the experiments. The predicted mist temperatures after radiative cooling are in good agreement with the measurements, with the experiments measuring 2.9 ± 0.2 °C and the models predicting 2.15 °C (EES) and 2.94 °C (MATLAB).

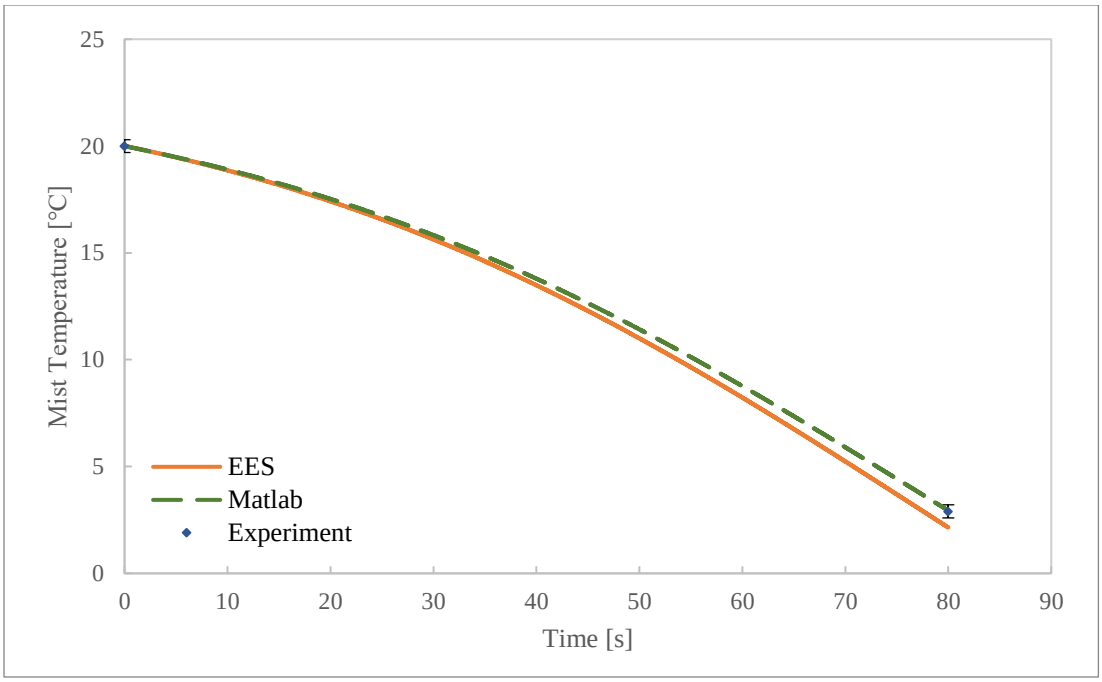

Figure 44. Mist temperature time profiles as predicted by the models (lines) and the measured mist temperatures before and after radiative cooling (symbol) with error bars.

6.2 Droplet volume concentration (Cv) correction

Spraytec system calculates Cv of a point in time by assuming spherical particles and uses the three-two moment (D_{32}) and transmission (T) in its calculation, and T is measured as the percentage of the laser signal that falls at the center of the detector (scattering ring 0) when droplets are present as compared to the background signal at ring 0 when no droplet is present [19]. In other words, T is equivalent to the transmittance (τ) of the media, which is defined as:

$$\tau = e^{-t}, \tag{49}$$

where τ = transmittance of the media, and
t = optical depth of the media.

Assuming negligible absorption, optically thin condition and geometric optics limit, we can calculate the optical depth t by:

$$t = K_s \cdot L, \tag{50}$$

$$K_s = \frac{1.5 Q_s}{D_{32}} Cv, \tag{51}$$

where K_s = scattering coefficient of the droplets,
L = scattering path length,
Q_s = scattering efficiency of the droplets,
D_{32} = the three-two moment of the droplet distribution, and
Cv = liquid water (droplet) volume concentration.

We can see from Eq. (19) and (20) that in reporting Cv, a path length L must have been assumed by Spraytec in its calculation. L as determined by the focal length and the configuration of the laser diffraction system is reportedly 12 mm, and since no other input of a physical path length is identified, it is reasonable to assume that Spraytec uses the same L of 12 mm in calculation of Cv. However, because T is measured after the signal is attenuated by all the media present in between the two set of optical windows, not only by the 12 mm in the center, the reported values of Cv (refer to as Cv_r hereinafter) by Spraytec likely differ from the actual droplet volume concentration, Cv_a.

By setting the optical depth t as constant, using Eq. (22) and (23) we can obtain a correction factor between Cv_a and Cv_r:

$$Cv_a = \frac{L_r}{L_a} Cv_r = 0.059 Cv_r, \tag{52}$$

where L_r = scattering path length as reported by Spraytec = 12 mm, and
L_a = actual scattering path length in the experiment = 203.2 mm.

With the average Cv_r to be reportedly 60 ppm, we could get Cv_a = 3.5 ppm by using Eq. (24). This value of Cv (3.5 ppm) is used as an initial condition in the models.

Note that no other information could be found on the algorithm used by Spraytec in calculating Cv. Since Spraytec also corrects for multiple scattering, the formula for calculating

Cv is most certainly more complicated than what is presented above. However, this analysis is still informative in getting a Cv that is closer to the actual value.

6.3 No-slip condition

No-slip condition is assumed between the droplet and the gas mixture in the models, meaning that all droplets move at the same speed as the gas flow, or in other words, there is no relative velocity or "slip" between the gas mixture and the surface of the droplets. Such assumption is valid for droplets having negligible terminal settling velocity as compared to the gas velocity. To examine the validity of the assumption, terminal settling velocities are calculated by:

$$v_t = \frac{D^2 \rho_l g C_c}{18\mu} \quad \text{(for Stokes' regime, Re < 0.1)} \tag{53}$$

$$C_D \,\mathrm{Re}^2 = \frac{4D^3 \rho(\rho_l - \rho)g}{3\mu^2} \quad \text{(outside of Stokes' regime, Re > 0.1)} \tag{54}$$

where v_t = terminal settling velocity of the droplet with diameter D (assuming spherical),
ρ_l = density of liquid water, taken as 1,000 kg/m^3,
g = gravitatonal acceleration, taken as 9.81 m/s^2,
C_c = slip correction coefficient, as determined by Eq. (5.13) in [21],
μ = dynamic viscosity of air, taken as 18.18×10^{-6} Pa · s (at 298 K and atmospheric pressure),
C_D = drag coefficient, as determined by Eq. (5.9) in [21],
Re = Reynolds number as defined later in Eq. (56), and
ρ = density of air, taken as 1.2 kg/m^3.

Eq. (18) and (19) correspond to Eq. (5.30) and (5.54) in [21] respectively. As determined in [21], for droplets smaller than 20 μm in diameter, Eq. (18) is applicable which straightforwardly gives v_t. For droplets larger than 20 μm in diameter, Stokes' Law becomes less

accurate and Eq. (19) should be used to determine the value of $C_D \mathrm{Re}^2$. With the calculated $C_D \mathrm{Re}^2$ and Figure 45 below (Figure 5.6 in [21]) the value of Re that corresponds to v_t can be determined, which yields v_t through the definition of Re:

$$\mathrm{Re} = \frac{v_t D}{\nu} \tag{55}$$

where ν = kinematic viscosity of air, taken as 15.06×10^{-6} m^2/s.

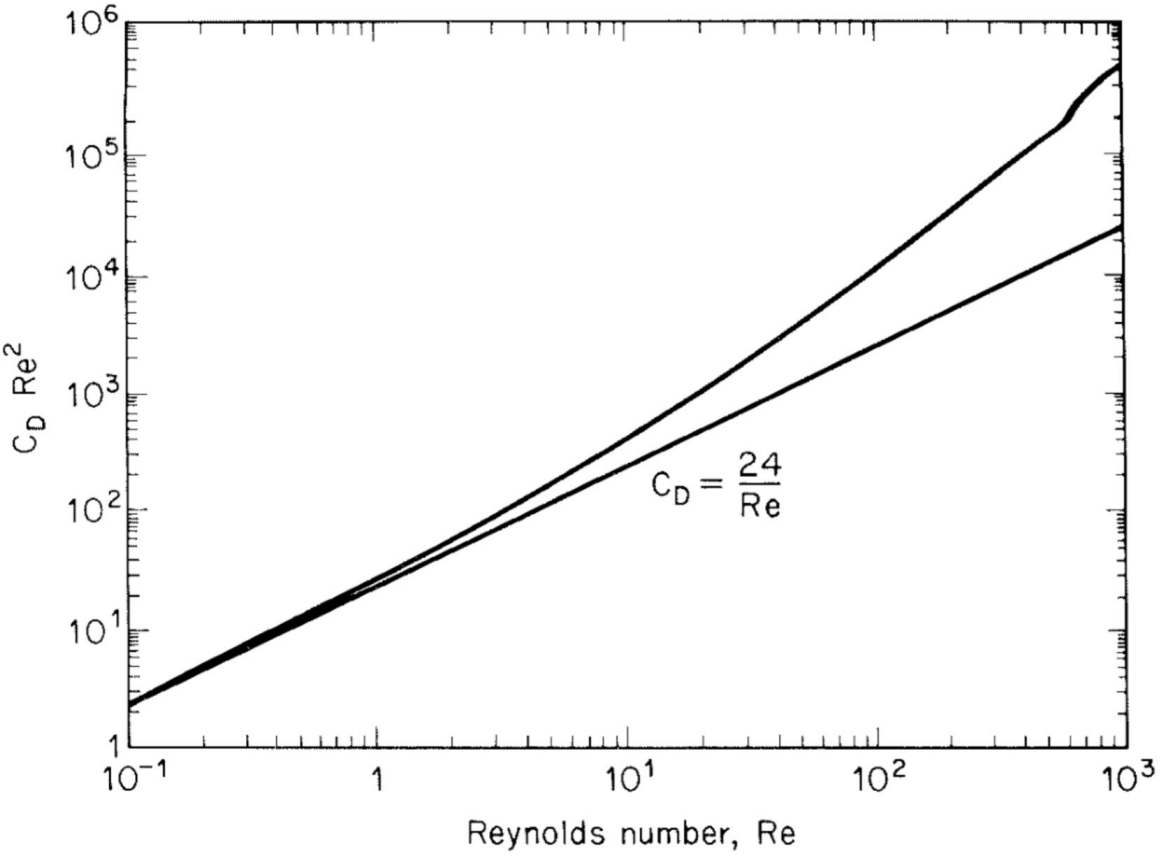

Figure 45. $C_D \mathrm{Re}^2$ as a function of Re for a sphere (Figure 5.6 in [21]).

Computed values of v_t for a few representative diameters are listed in Table 1. We could see that for droplets smaller than 10 μm in diameter, their v_t are relatively small as compared to the gas velocity, which means that the no-slip assumption is acceptable. However, for larger droplets of a few 10's μm in diameter, their v_t could be a few times larger than the gas velocity,

creating velocity gradient or "slip" near the droplet surface. Although most droplet volume in our mist flow resides below diameter of 10 µm, the few larger droplets with velocity differences as compared to smaller ones could become collector droplets that initiate collision-coalescence as they fall through the mist stream and collect smaller droplets, forming even bigger droplets. Such process is not considered in the models (the number of droplets is assumed constant unless droplets are calculated to be removed by evaporation) but is likely happening in the experiments. This may help explain the presence of bigger droplets observed in the experiment than calculated in the models.

Table 4. Terminal settling velocity of droplets of different diameters.

D [µm]	v_t [cm/s]	% of gas velocity (0.63 cm/s)
1	0.0035	1%
5	0.078	12%
10	0.31	49%
20	1.5	238%
30	3	476%

6.4 Droplets with diameter smaller than ~2.5 µm after radiative cooling

According to the models, once the droplet evaporates to a diameter smaller than a threshold diameter (0.1 µm), it is considered completely evaporated and is taken out from the system. This is a manifestation of the Kelvin effect, where droplets smaller than a critical diameter as determined by the supersaturation would evaporate and eventually disappear. This explains the removal of droplets smaller than ~2.5 µm in diameter after radiative cooling as seen in modeling results (Figure 23). However, in the experiments, droplets were still present in that range (Figure 43). This could possibly be related to Malvern system's effective measuring range that covers 2.5 – 4,000 µm. If we remove the smoothed lines, for example, in Figure 22, and observe the original measured distributions before and after cooling (Figure 46), we could see that the characteristic peaks and valleys smaller than 2.5 µm are almost entirely preserved. This

phenomenon can also be observed for any other original measured distributions presented in this study. This may suggest that the measured distribution for droplets smaller than 2.5 μm in diameter in the experiments is a systematic error caused by the inaccuracy of the instrument outside of its effective range.

Conversely, assuming there are indeed droplets present with under 2.5 μm diameter, what could possibly be the cause? Although the apparatus is set up to minimize the aerosols at its supply end by using deionized water for mist generation and a HEPA filter to condition the air, the fact that the apparatus is an open system which is in contact with the room air, makes it possible that some aerosols present in the room air can be entrained and activated under the supersaturated environment during experiments. Future work could be done to run the room air through a cloud condensation nuclei (CCN) counter after it is filtered while the experiment is running and estimate the effect by the activation of room aerosols.

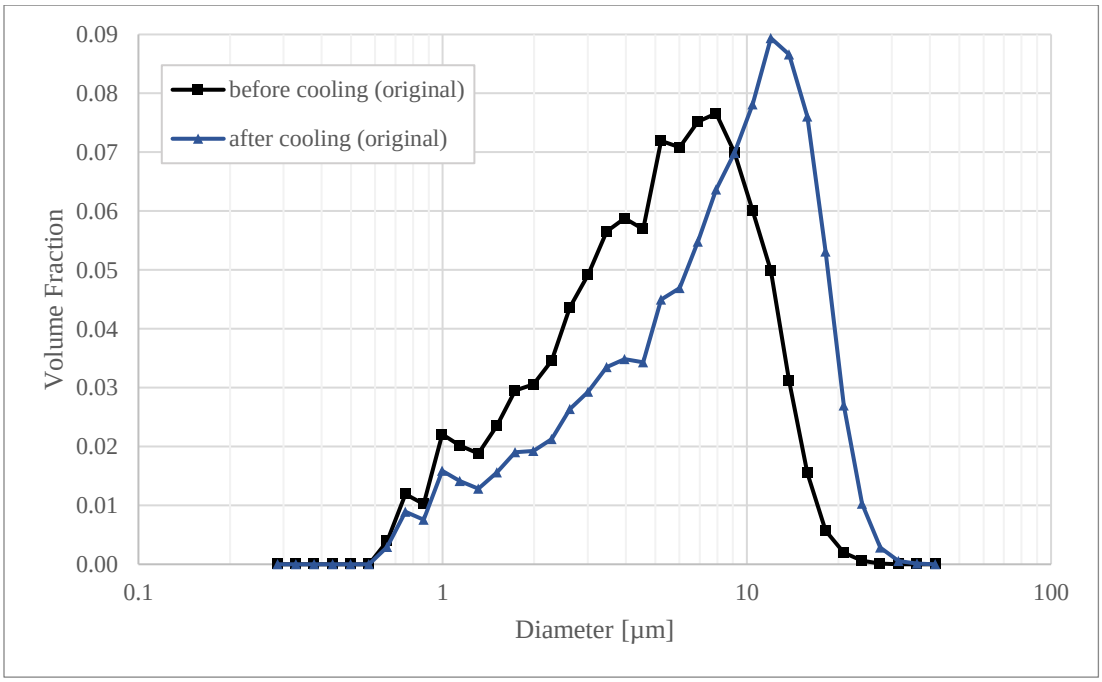

Figure 46. Similar to Figure 22 except that the boxcar smoothed lines are removed to show the characteristics of the original measured distributions.

CHAPTER 7: SUMMARY AND FUTURE WORK

7.1 Summary of important findings and conclusions

In this study, both experimental and modeling work were done to better understand the process of radiative cooling of cloud/mist droplets and its effect on droplet growth.

The experimental apparatus was originally designed and operated by two previous students. Issues were first identified with the original horizontally-oriented setup, including: 1) droplets generated by commercial humidifiers did not have large enough size to represent cloud droplets (typically of 10's μm diameter), making a precooling section necessary; 2) surface condensate was inclined to form due to the presence of the precooling section and caused undesirable production of big droplets of diameter larger than 100 μm; 3) the effect of droplet gravitational settling in the radial direction could not be controlled or quantified, potentially invalidating the measurement results. Modifications were made to address these issues. The original commercial humidifier was replaced by an ultrasonic piezoelectric atomizing disk which produces droplets from a few to 20 μm in diameter, suitable for the experiments. The precooling section was then eliminated. The apparatus was also reoriented into a vertical direction, setting gravity in the same direction as the mist flow to prevent droplets from settling radially. In addition to addressing the existing issues, more efforts were made to eliminate experimental factors that might influence the credibility of the results. An air-tight housing was built for the ultrasonic atomizer to ensure the system's stable operation. This also allowed the air supply to be maintained saturated and aerosol-free by a bubble humidifier and a HEPA filter. The addition of rotameters made it possible to precisely control and measure the mist flow rate.

Experiments were conducted with the improved apparatus under two boundary conditions: the isothermal wall condition following the previous work, where the tube wall was kept at a constant temperature, and the conductively-adiabatic wall condition, where the tube wall matched the mist temperature as it cooled so conductive heat transfer was minimized. Under the isothermal wall condition, the mist entering the test section with an average D_{43} = 6.04 µm was cooled for 80 s at radiative sink temperature of 0℃, -10℃ and -20℃, and D_{43} on average grew to 6.43 µm, 6.82 µm and 7.30 µm, respectively. Under the adiabatic wall condition, the mist entering the test section at 20℃ with an average D_{43} = 5.51 µm was cooled radiatively at -20℃ sink temperature. After a residence time of 80 s the mist temperature dropped to 2.9 ℃ and the average D_{43} grew to 8.39 µm. The droplets grew a larger relative amount in the adiabatic-wall case than in the isothermal wall case for the same residence time because heat conduction from the PE wall was not mitigating the volumetric radiative cooling effect to the radiative sink. The reproducibility of the results was shown with less than 1% coefficient of change for all the measurements. The experiments showed that radiative cooling can grow the droplets considerably in diameter subject to the conditions of the experiments.

Two computational models were developed to model the conductively-adiabatic wall experiments based on the mass- and energy-balance equations. The EES model solves the fully coupled system including the unsteady water mass balance and preserves more physical variables for analysis, yet it requires more than 10 hours of computational time for modeling the 80 s experiment. The MATLAB model reduces the complexity of the system by assuming quasi-steady water vapor mass balance and greatly reduces the computational time to a few 10’s of seconds. The results from both the models showed remarkable agreements in droplet

distributions, mist temperature and supersaturation profiles, confirming the validity of the quasi-steady water vapor approximation in these mist systems.

A parametric study was done with the MATLAB model to study the effects of varying sink temperature and liquid water volume concentration on mist droplet distributions, temperature and supersaturation. When the mist is at the same temperature of the sink, no form of heat exchange is present between the mist and the external environment, and the mist droplets go through a process of internal equilibration by evaporating smaller droplets while feeding the growth of bigger droplets, leading the droplet distribution to become larger and more monodispersed as time progresses. Temperature influences the degree of such equilibration by determining the rate of mass transfer via diffusion of water. Lower temperature leads to lower saturation vapor pressure, which slows the overall rates of evaporation and condensation, and as a result, less internal equilibrating effect (droplet growth) is predicted within a given time period. When radiative cooling is added as an external factor, the mist droplets go through both internal and external equilibrations. Radiation-augmented external equilibration grows larger droplets at a faster rate, shifting the size distribution more towards larger droplets. However, the external equilibration dies down as mist temperature approaches sink temperature, and afterwards internal equilibration dominates the dynamics of droplet size distribution evolution, which is subject to the temperature and saturation pressure effect. The mist droplet volume concentration affects the mist's sensitivity to radiation-influenced external equilibration. Higher mist droplet volume concentration makes the mist cool faster, but with less sensitivity to external equilibration. This allows internal equilibration to quickly take over and become dominant, subject to the temperature and saturation pressure effect. Thinner mist (lower mist droplet volume concentration) does not cool as efficiently but is very sensitive to radiation augmentation,

shifting the size distribution towards larger droplets, the manifestation of a more predominant external equilibration.

The comparison between the experiment and modeling results showed excellent agreements in the mist temperature and D_{43} predictions with ~1% difference. The experimental size distribution after radiative cooling is in bulk agreement with the model prediction, while discrepancies were observed for the smallest and largest droplets. Measurements showed preservation of droplets smaller than 2.5 μm in diameter during radiative cooling and more significant droplet growth in larger droplets, while the models predicted complete removal of droplets below 2.5 μm and more volume fraction of droplets between 5-12 μm with less above 12 μm, compared with experiments.

Assumptions were examined to explain the differences between experimental and modeling results. No-slip condition was assumed in the models. By calculating the terminal settling velocities of droplets of different sizes, the no-slip condition is validated for droplets smaller than 10 μm but likely breaks down for larger droplets. This may stimulate collision-coalescence in the experiments that would result in larger droplets than condensational growth alone would produce, which is not considered in the models. Another assumption examined was that of pure water droplets in the model (no solute effect). If condensation nuclei got into the apparatus from the openings or due to filter failure, they could possibly activate and account for the apparent distribution below 2.5 μm in the experiments. However, since the Spraytec laser diffraction system has an effective measuring range of 2.5 – 4,000 μm, the measurements below 2.5 μm could also include a systematic error caused by the inaccuracy of the instrument.

In conclusion, the study accomplished the objectives set forth at the beginning and showed through experimental and modeling work that radiative cooling can augment droplet

growth considerably under favorable conditions, which makes it a potential important mechanism in cloud droplets overcoming condensation-coalescence bottleneck.

7.2 Limitations and future work

The modeling study conducted here is a simplified analysis of the actual complex processes because of the assumptions made and the many externalities that were not well understood. There are limitations that could be addressed in future work to take into consideration more externalities and further the understanding of radiation-induced condensational growth of cloud/mist droplets, and a few of them are highlighted below.

Since the two models only describes the experiment processes under conductively-adiabatic wall conditions, another dimension along the radial direction of the tube could be incorporated so that the models would have the ability to model experiments under isothermal wall conditions. All experimental results presented in this study could then be compared with the modeling results which might provide more valuable insights.

To address the differences in experimental and modeling results, the no-slip and no-solute assumptions might need to be relaxed. Incorporating collision and coalescence by parameterization would help where the no-slip condition breaks down for larger droplets. CCN analysis for the air that passed through the HEPA filter might be helpful in confirming or eliminating the effect of aerosol activation. Quantifying and correcting for any error in the droplet size measurements below 2.5 μm diameter would also be useful. The solute effect could also be included in the models. An initial effort should be to explore hypothetical solute properties that would allow the initial mist size distribution to be relatively stable, as seemed to be the case experimentally. In regard to the latter conjecture, measurements of the internal

equilibration process (without radiation) to confirm or check the stability of the initial droplet size distribution and further validate modeling assumption using the internal equilibration process, at least at room temperature. This recommendation also leads to the next.

The before and after radiative cooling in the experiments were fixed as two discrete stages, and tracing the changes as the mist flows and develops was impossible due to instrument limitations. However, if tracing in time could be realized, the model and experiment comparison could then be done in time profiles, unlocking more possibilities in exploring the phenomenon.

Moving forward, more work could be done to include soluble and insoluble aerosols as CCN in the mist droplets, more resembling cloud droplets in the atmosphere. Some aerosols (e.g. black and brown carbon) have very different radiative properties than pure water; it would be interesting to see how the addition of such aerosols could alter the inherent characteristics of the droplets and their effects to radiation augmented growth. The effect of shortwave radiative heating is also worthwhile to explore as suggested by the literature. Seeing the interactions between these added externalities would be fascinating, and if the technology advancements in atmospheric observation in the future would allow us to measure cloud droplet sizes when radiative cooling was controlled and/or measured in the atmosphere, we would be able to compare these laboratory experimental results with atmospheric observations. Although there is still distance to cover, any contribution along this path might lead us closer to understanding mechanisms by which droplets overcome the condensation-coalescence bottleneck.

REFERENCES

[1] Y. Zhou, “Water cycle and precipitation,” 2019. [Online]. Available: https://atmospheres.gsfc.nasa.gov/climate/index.php?section=135. [Accessed: 08-Jun-2019].

[2] T. F. Stocker, Q. Dahe, and G.-K. Plattner, “Technical summary,” *Intergov. Panel Clim. Chang. Phys. Sci. Basis*, 2013.

[3] J. M. Wallace and P. V. Hobbs, *Atmospheric Science: an Introductory Survey*, 2nd ed. Oxford, UK: Elsevier Inc., 2006.

[4] C. M. Hartman and J. Y. Harrington, “Radiative impacts on the growth of drops within simulated marine stratocumulus. Part II: solar zenith angle variations,” *J. Atmos. Sci.*, vol. 62, no. 7, pp. 2339–2351, Jul. 2005.

[5] C. M. Hartman and J. Y. Harrington, “Radiative impacts on the growth of drops within simulated marine stratocumulus. Part I: maximum solar heating,” *J. Atmos. Sci.*, vol. 62, no. 7, pp. 2323–2338, Jul. 2005.

[6] J. Marquis and J. Y. Harrington, “Radiative influences on drop and cloud condensation nuclei equilibrium in stratocumulus,” *J. Geophys. Res. D Atmos.*, vol. 110, no. 10, pp. 1–13, 2005.

[7] J. Y. Harrington, G. Feingold, and W. R. Cotton, “Radiative impacts on the growth of a population of drops within simulated summertime arctic stratus,” *J. Atmos. Sci.*, vol. 57, no. 5, pp. 766–785, 2000.

[8] O. Reynolds, “On the manner in which raindrops and hailstones are formed,” vol. 3, no. 6, pp. 48–60, 1877.

[9] N. A. Fuchs, “Evaporation and droplet growth in gaseous media.,” *Pergamon Press*, p. 72, 1959.

[10] W. T. Roach, “On the effect of radiative exchange on the growth by condensation of a cloud or fog droplet,” *Q. J. R. Meteorol. Soc.*, vol. 102, no. 432, pp. 361–372, 1976.

[11] B. R. Barkstrom, “Some effects of 8–12 μm radiant energy transfer on the mass and heat budgets of cloud droplets,” *J. Atmos. Sci.*, vol. 35, no. 4, pp. 665–673, Apr. 1978.

[12] T. Elperin *et al.*, “Acceleration of raindrop formation due to the tangling-clustering instability in a turbulent stratified atmosphere,” *Phys. Rev. E*, vol. 92, no. 1, p. 013012, Jul. 2015.

[13] M. Q. Brewster, “Evaporation and condensation of water mist/cloud droplets with thermal radiation,” *Int. J. Heat Mass Transf.*, vol. 88, pp. 695–712, 2015.

[14] R. Guzzi and R. Rizzi, “The effect of radiative exchange on the growth of a population of droplets.,” *Contrib. Atmos. Phys.*, vol. 53, pp. 351–365, 1980.

[15] P. H. Austin, S. Siems, and Y. Wang, “Constraints on droplet growth in radiatively cooled stratocumulus clouds,” *J. Geophys. Res.*, vol. 100, no. D7, p. 14231, Jul. 1995.

[16] K. K. Roman, “Radiative impacts on water mist/cloud droplet condensative growth,” University of Illinois at Urbana-Champaign, 2018.

[17] E. O. McNichols, “Water droplet growth enhancement through thermal radiation,” Univerisity of Illinois at Urbana-Champaign, 2017.

[18] C. Rodes, T. Smith, R. Crouse, and G. Ramachandran, “Measurements of the size distribution of aerosols produced by ultrasonic humidification,” *Aerosol Sci. Technol.*, vol. 13, no. 2, pp. 220–229, 1990.

[19] Malvern Instruments Ltd., “Spraytec installation manual,” no. 1. 1999.

[20] S. A. Klein, “Development and integration of an equation-solving program for engineering thermodynamics courses,” *Comput. Appl. Eng. Educ.*, vol. 1, no. 3, pp. 265–275, Jan. 1993.

[21] R. C. Flagan and J. H. Seinfeld, *Fundamentals of Air Pollution Engineering*. Englewood Cliffs, New Jersey: Prentice-Hall, Inc., 1988.

APPENDIX A: EXPERIMENT PROCEDURES

1. Take noise measurement using Malvern software. Save file for record. Turn on laser.
2. Check optical windows for debris; clean if needed.
3. Open "Corrected light scattering" window, click "start" and check laser alignment. If the first signal bar is above 1,300 unit, the alignment is good and the experiment can proceed; if not, the system needs to be realigned. Refer to Spraytec Manual for instructions on alignment.
4. Make sure LN_2 is filled.
5. Check water level in the mist generator; add water with the squeeze bottle if needed.
6. Check annular air supply at the desired flowrate (1.5 l/s for experiments in the thesis).
7. Check thermocouples and make sure they function well.
8. Start lab air supply and tune to desired flow rate (AF1).
9. Check humidifier water level. Add hot water to the bath tank. Keep checking the water bath temperature throughout the experiment, and replace hot water if needed (around every 30 min).
10. 30-60 min after laser is on, check background reading until it stabilizes. Save file.
11. Turn on mist generator. Turn on heat guns.
12. Take "before" reading using Flash Mode 20 min after the mist is on. Turn off heat guns for the measurements and turn them back on afterwards. Take note of T, D_{43}, Cv and make sure they are within reasonable ranges. Save files.
13. Add LN_2 till desired temperature. While maintaining the temperature, turn on annular air flow, take readings 5 min after temperature is reached, and proceed only when a consistent size distribution is achieved. Save files.
14. Allow tube to warm up. Repeat step 13 at different temperatures if needed.
15. After the measurements are done, turn off: annular air supply, mist generator, heat guns, lab air supply, and laser.

*all readings are by default 30 s unless otherwise stated.

APPENDIX B: ENGINEERING EQUATION SOLVER (EES) MODEL

```
"Numerical model, 04/29"
"Programed with Engineering Equation Solver (EES) Academic Professional V10.488"
"by Xinchang Li"

//subscripts:
"a / 2: air"
"v: water vapor"
"e: environment, = a + v"
"l: liquid water"
"w / 1: water the substance"

//initial state properties
V0 = 1*(convert(cm, m))^3                                   "total measuring volume"
Cv0 = 60e-6                                                 "volume concentration of droplets. (value taken as an estimated average from 0426 --> 0-2 to 7 measurements, actual avg = 59.0ppm)"
Te0 = 20 [C]                                                "initial temperature of environment (e) far away from droplets"
Ts0 = 20 [C]                                                "initial temperature of droplets, assume equal to the temperature of vapor directly adjacent to the surface of the droplets (s) (?)"
Twall = -20 [C]                                             "sink temperature, actual average (0426 > 0-2 to 7) = -20.7C"
P = 101 [kPa]
phi_0 = 1.002 [-] "using this to calc mv0"                  "initial relative humidity"
rho_l0 = density(Water, T=Ts0, P=P)
Pv0 = phi_0 * p_sat(Water,T=Te0)
Pa0 = P - Pv0
ma = Pa0*V0 / (Ra*converttemp(C, K, Te0))                   "Initial mass of air (stays constant throughout)"
mv0 = Pv0*V0 / (Rw*converttemp(C, K, Te0))                  "Initial mass of water vapor"
Vl0 = sum(Vi[i], i = 1, 37)                                 "initial volumn of liquid water"
ml0 = Vl0 * rho_l0                                          "initial mass of lilquid water"

//constants
MW_a = 28.97 [kg/kmol]                                      "molar weight of air"
MW_w = 18.02 [kg/kmol]                                      "molar weight of water"
Ra = R#/MW_a
Rw = R#/MW_w
D_12 = 2.44E-05 [m^2/s]"need to update as T changes"        "mass diffusivity of water (1) in air (2)"
ke = 2.66E-02 [W/m-K] "need to update as T changes"         "thermal conductivity of the environment (e). Taken from Psat2Dqs, Sheet 1, D8"
K_a = 1/(4.3e-6)                                            "average absorption coeff. suggested by Roach (1976)"
Nuss_d = 2 [-]                                              "Nusselt number at conduction limit"
Sher_d = 2 [-]                                              "Sherwood number at conduction limit"

//stop criteria
d_min = 1e-7 [m]                                            "minimum droplet size. To prevent d goes below zero.
m``_max = 0.01

//time
time = 40 [s]                                               "residence time"
```

```
step = 0.0001 [s]                                   "time step"

//properties that update with time
Re = R#/MW_e
MW_e = MW_a*y_a + MW_w*y_v                          "molar weight of (a) & (v) mixture = (e)"
y_v = (m1e/MW_w) / (m1e/MW_w + (1-m1e)/MW_a)        "y_v: mole fraction of (v), = n_v / ntot"
y_a = 1 - y_v                                       "y_a: mole fraction of (a), = n_a / ntot"
rho_e = P / (Re*converttemp(C, K, Te)) "[kg/m^3]"   "density of mixture (a) + (v)"
Cpa = cp(Air,T=Te) "using ideal gas property. Real fluids?"
Cpv = cp(H2O,T=Te) "using ideal gas property. Real fluids?"
V_l = sum(V_li[i], i = 1, 37)                       "total liquid water volume"
ml = sum(mli[i], i = 1, 37)                         "total liquid water mass"
V_v * rho_e = ma + mv
V = V_l+V_v
Cv = V_l / V

//mass conservation check
mw0 = mv0 + ml0                                     "initial mass of water (vapor and liquid)"
mw = mv + ml                                        "final mass of water (vapor and liquid) at time =
x"
DELTA_mv = mv - mv0                                 "change in mass of water vapor (final - initial)"
DELTA_ml = ml - ml0                                 "change in mass of liquid water (final - initial)"
DELTA_mw = mw - mw0                                 "change in total mass of water; should be as
close to zero as possible"

//size bins & distributions
    //size bins
di[1..37] = [0.2685e-6, 0.3085e-6, 0.354e-6, 0.4065e-6, 0.467e-6, 0.536e-6, 0.6155e-6, 0.7065e-6,
0.811e-6, 0.9315e-6, 1.068e-6, 1.225e-6, 1.41e-6, 1.62e-6, 1.86e-6, 2.135e-6,2.45e-6, 2.815e-6, 3.235e-
6, 3.715e-6, 4.265e-6, 4.895e-6, 5.62e-6, 6.455e-6, 7.41e-6, 8.51e-6, 9.77e-6, 11.215e-6, 12.88e-6,
14.79e-6, 16.985e-6, 19.505e-6, 22.395e-6, 25.715e-6, 29.525e-6, 33.9e-6, 38.925e-6] "normalized"
    //volume faction distr. vi%:
vi%[1..37] = [0.00000, 0.00000, 0.00000, 0.00000, 0.00000, 0.00000, 0.00391, 0.01189, 0.01025,
0.02209, 0.02020, 0.01879, 0.02355, 0.02955, 0.03053, 0.03456, 0.04364, 0.04921, 0.05655, 0.05877,
0.05691, 0.07195, 0.07085, 0.07518, 0.07658, 0.06999, 0.06010, 0.04985, 0.03117, 0.01551, 0.00570,
0.00195, 0.00060, 0.00012, 0.00003, 0.00000, 0.00000] "0426, 0-2 to 7 average, original normalized"


Duplicate i = 1, 37

    //volume distr. Vi (initial):
Vi[i] = vi%[i] * V0 * Cv0
    //number distr. Ni (keeps constant for each i):
Ni[i]*(1/6)*pi*(di[i]^3) = Vi[i]
    //volume distr. changing as d changes / liquid water volume for each bin, V_li:
V_li[i] = Ni[i]*(1/6)*pi*(d[i]^3)
    //volume faction distr. changing as d changes, v%:
v%[i] = V_li[i] / V_l
    //liquid water mass for each bin, mli:
mli[i] = V_li[i] * rho_l[i]

//vapor phase (1/2): e (environment) = a (air) + v (water vapor)
    //mass:
m`i[i] = m``[i] * pi*d[i]^2 * Ni[i]                 "m`: m_dot"
m``_check[i] = hm[i] * rho_e * (m1e - m1s[i])       "m``: m_dot_prim prim"
```

```
hm[i] = Sher_d * D_12 / d[i]                                    "hm: mass transfer coeff. equivalent in form to heat transfer coeff."
m``[i] = if(abs(m``_check[i]),m``_max,m``_check[i],0,0)         "From Ezra's code line 172."
{m``[i] = hm[i] * rho_e * (m1e - m1s[i])}

m1s[i] = Pv_s[i] / (1.61*P - 0.61*Pv_s[i])                      "m1s: mass fraction of water vapor (1) at (s); needs to upgrade to an array variable"
Pv_s0[i] = p_sat(Water, T=Ts[i])
exppower[i] = (4*18*(0.000000144*(374-6-Ts[i])/(18/1000000)^(2/3))/8.314/(Ts[i]+273.15))/(d[i]*1e6)
Pv_s[i] = Pv_s0[i] * exp(exppower[i])                           "from Psat2Dqs, col. J"

    //energy:
q_cs[i] = hc[i] * (Te - Ts[i]) * convert(W, kW)
hc[i] = Nuss_d * ke / d[i]                                      "hc: heat transfer coeff."

//droplets, (s) = surface of droplets, temperature = Ts
    //mass:
dddt[i] = 2 * m``[i] / rho_l[i]
rho_l[i] = density(Water,T=Ts[i],P=P)
d_check[i] = di[i] + integral(dddt[i],x,0,time,step)
d[i] = if(d_check[i], d_min, d_min, d_min, d_check[i])          "IF(A, B, X, Y, Z): If A<B, the function will return a value equal to the value supplied for X;  if A=B, the function will return the value of Y;   if A>B, the function will return the value of Z."

    //energy:
0 = q_cs[i] - q_r[i] * Qa[i] + m``[i]*h_fg[i]
q_r[i] = -sigma# * ((converttemp(C, K, Twall))^4 - (converttemp(C, K, Ts[i]))^4) * convert(W, kW)
Qa[i] = 1 - (2/tau[i]^2) * (1 - (1+tau[i]) * exp(-tau[i]))      "Qa: volumetric absorption efficiency. IJHMT (24)"
tau[i] = K_a * d[i]                                             "tau: optical depth of a single droplet"
h_fg[i] = enthalpy_vaporization(Water,T=Ts[i])

End


//vapor phase (2/2)
    //mass:
m` = sum(m`i[i], i = 1, 37)                                     "total mass transfer rate, sum of m_dot"
dmvdt = -m`                                                     "Psat2Dqs, col. X"
mv = mv0 + integral(dmvdt, x, 0, time, step)                    "F = INTEGRAL(Integrand, VarName, LowerLimit, UpperLimit, StepSize)"
m1e = Pv_e / (1.61*P - 0.61*Pv_e); Pv_e = phi * Pv_e0           "m1e: mass fraction of water vapor (1) at (e)"
phi * (Pv_e0 * (1 + (MW_w/MW_a)*(ma/mv))) = P
Pv_e0 =  p_sat(Water,T=Te)

    //energy:
Q_cs = sum(q_cs[i] * Ni[i] * pi * d[i]^2, i = 1, 37)
dTedt = (-Q_cs) / (ma*Cpa + mv*Cpv)                             "Psat2Dqs, col. B"
Te = Te0 + integral(dTedt, x, 0, time, step)


$integraltable x:0.01 phi Te DELTA_mw DELTA_mv DELTA_ml mw mv ml m` V Cv d[1..37]
{$ShowWindow Plot}
```

APPENDIX C: MATLAB MODEL

```
%The following code is written by M. Quinn Brewster and Xinchang Li.

tstepmax = 8001;        %total steps
deltat = 0.01;
tstep = 1:tstepmax;     %time step index
nmax = 31;
nmin = 1;
n = nmin:nmax;          %droplet diameter bin index
t(1,tstep) = 0:deltat:(tstepmax-1)*deltat; %time, s
Rw = 0.4615;        %kJ/kg-K
sigma = 5.67e-8;    %W/m^2K^4
sigma_s = 7.19e-2;  %N/m, 7.49 at 5C
D12 = 2.48e-05;     %m^2/s
T0 = -20+273.15;    %K, initial temp
Tm = -20+273.15;    %K, average of T0 and T_final (-12C)
Tr = -20+273.15;    %K, radiative sink temp
Kapm = 0.52;        %1/m, Planck mean absorption coefficient for
droplets
CV = 3.5e-6;        %total droplet volume concentration
k = 2.66E-02;       %W/m-K, e-state thermal conductivity
rho = 1.2;          %kg/m*3, e-state density
rho_l = 1000;       %kg/m^3, liquid water density
Cp = 1000;          %J/kg-K, e-state specific heat
Psem = 0.6571e3;    %Pa, saturation pressure
hfgm = 2499;        %kJ/kg
Hm = hfgm./(Rw.*Tm.^2);   %1/K
PSIm = k.*Rw.*Tm./(D12.*hfgm.*Psem); %1/K
hrm = sigma.*(Tm^2+Tr.^2).*(Tm+Tr); %W*m^-2*K^-1
trm = rho.*Cp./(4.*hrm*Kapm); %s
trcm = trm.*(1 + Hm./PSIm); %s, HEFAT Eq 38

thetam = exp(-t./trcm);%analytic integral; HEFAT Eq 37

%Tempm = thetam.*(T0-Tr)+Tr; %K
Dc = 4.*sigma_s./(rho_l.*(Rw.*1000).*Tm); %m
D0 = [0.6155e-6, 0.7065e-6, 0.811e-6, 0.9315e-6, 1.068e-6, 1.225e-6,
1.41e-6, 1.62e-6, 1.86e-6, 2.135e-6,2.45e-6, 2.815e-6, 3.235e-6,
3.715e-6, 4.265e-6, 4.895e-6, 5.62e-6, 6.455e-6, 7.41e-6, 8.51e-6,
9.77e-6, 11.215e-6, 12.88e-6, 14.79e-6, 16.985e-6, 19.505e-6, 22.395e-
6, 25.715e-6, 29.525e-6, 33.9e-6, 38.925e-6]; %m
D0 = D0';
fv0 =
[0.00391,0.01189,0.01025,0.02209,0.02020,0.01879,0.02355,0.02955,0.030
53,0.03456,0.04364,0.04921,0.05655,0.05877,0.05691,0.07195,0.07085,0.0
7518,0.07658,0.06999,0.06010,0.04985,0.03117,0.01551,0.00570,0.00195,0
.00060,0.00012,0.00003,0.00000,0.00000];
fv0 = fv0'.*CV;
```

```
fv0sum = sum(fv0);
No0 = fv0./(pi./6.*D0.^3); %m^-3N
No0sum = sum(No0);
%s0 = Dc*sum(fv0./D0.^3)/sum(fv0./D0.^2); %initial supersaturation
Ka = 1/(4.3e-6); %1/m
tau0 = Ka.*D0;
Qa0 = 1.*( 1 - (2./tau0./tau0) .* (1 - (1+tau0) .* exp(-tau0)));
Kap0 = sum(Qa0.*(pi./4).*D0.^2.*No0); %m^-1
D430 = sum(No0.*D0.^4)/sum(No0.*D0.^3);

slope = zeros(nmax,1);
Deltatheta = zeros(nmax,1);
thetaold = ones(nmax,1);
thetanew = zeros(nmax,tstepmax);

slopeD = zeros(nmax,1);
DeltaD = zeros(nmax,1);
Dold = D0;
Dnew = zeros(nmax,tstepmax);
s = zeros(1,tstepmax);

Dmin_threshold = .1e-7;

for i = 1:tstepmax      %main loop marching through time

    if Dold(nmin) < Dmin_threshold
        nminold = nmin;
        nmin = nminold+1;
        n = nmin:nmax;
    else
    end

    tau(n,1) = Ka.*Dold(n);
    Qa(n,1) = 1.*(1 - (2./tau(n).^2).* (1 - (1+tau(n)) .* exp(-
tau(n))));
    Kap = sum(Qa(n).*(pi./4).*Dold(n).^2.*No0(n));

    Temp(n,1) = thetaold(n).*(T0-Tr)+Tr; %K
    TC(n,1) = Temp(n) - 273.15; %C
    hr(n,1) = sigma.*(Temp(n).^2+Tr.^2).*(Temp(n)+Tr); %W*m^-2*K^-1
    tr(n,1) = T0./Temp(n).*rho.*Cp./(4.*hr(n).*Kap); %s
    hfg(n,1) = 2501-(4.2-1.86).*TC(n); %kJ/kg
    H(n,1) = hfg(n)./(Rw.*Temp(n).^2);   %1/K
    Pse(n,1) = (.61138+4.4053e-2.*TC(n)+1.4594e-3.*TC(n).^2+2.6092e-
5.*TC(n).^3+2.8332e-7.*TC(n).^4+2.7316e-9.*TC(n).^5).*1000; %Pa
    PSI(n,1) = k.*Rw.*Temp(n)./(D12.*hfg(n).*Pse(n)); %1/K
    trc(n,1) = tr(n).*(1 + H(n)./PSI(n)); %s
    slope(n,1) = -thetaold(n)./trc(n);
    Deltatheta(n,1) = slope(n).*deltat;

    thetanew(n,i) = thetaold(n) + Deltatheta(n);
    thetaold(n) = thetanew(n,i);
```

```
    Gamma(n,1) = 8.*k./rho_l./hfg(n)./1000; %m^2/s/K
    fv(n,1) = No0(n).*(pi./6).*Dold(n).^3;
    s(1,i) = Dc*sum(No0(n))/sum(No0(n).*Dold(n));
    slopeD(n,1) = Gamma(n)./(H(n)+PSI(n))./(2.*Dold(n)).*(s(1,i)-
Dc./Dold(n)+(hr(n).*(Temp(n)-Tr).*Qa(n).*H(n).*Dold(n)./(2.*k)));
    DeltaD(n,1) = slopeD(n).*deltat;

    Dnew(n,i) = Dold(n) + DeltaD(n);
    Dold(n) = Dnew(n,i);

end

Kapfold = 0;
D43numold = 0;
D43denold = 0;
for i = nmin:nmax  % this one excludes unwanted first few elements
    Kapfnew = Kapfold + Qa(i)*(pi/4)*Dold(i)^2*No0(i);
    Kapfold = Kapfnew;
    D43num = D43numold + No0(i)*Dold(i)^4;
    D43numold = D43num;
    D43den = D43denold + No0(i)*Dold(i)^3;
    D43denold = D43den;
end
D43 = D43num/D43den;
Kapf = sum(Qa.*(pi./4).*Dold.^2.*No0); %m^-1 this one includes
unwanted first few elements
fvfsum = sum(fv);

figure
plot(t(1,tstep),thetanew(nmax,tstep),'b',t(1,tstep),thetam(1,tstep),'r
')
legend("theta Num","theta Ana",'Location','northeast')

figure
semilogx(D0,fv0./fv0sum,'r',Dnew(n,tstepmax),fv(n)./fvfsum,'b')
legend("rel fv initial","final",'Location','northeast')

x = zeros(1,tstepmax);
x(tstep) = t(1,tstep);

figure
plot(t(1,tstep),Dnew(5,tstep).*1e6,'-',...
        t(1,tstep),Dnew(7,tstep).*1e6,'--',...
        t(1,tstep),Dnew(9,tstep).*1e6,'-.',...
        t(1,tstep),Dnew(11,tstep).*1e6,':k',...
        t(1,tstep),Dnew(13,tstep).*1e6,'-',...
        x(1:5000:tstepmax),Dnew(15,1:5000:tstepmax).*1e6,'-^',...
        x(1:5000:tstepmax),Dnew(20,1:5000:tstepmax).*1e6,'-s',...
        x(1:5000:tstepmax),Dnew(25,1:5000:tstepmax).*1e6,'-x',...
        x(1:5000:tstepmax),Dnew(31,1:5000:tstepmax).*1e6,'-
d','LineWidth',1.5)
```

```
xlim([0 600])
ylim([0 50])
legend("bin 5","bin 7","bin 9","bin 11","bin 13","bin 15","bin
20","bin 25","bin 31",'Location','northeast')
xlabel("Time [s]")
ylabel("Diameter [\mum]")

fh = findall(0,'Type','Figure');
txt_obj = findall(fh,'Type','text');
set(txt_obj,'FontName','Times New Roman','FontSize',10.5);
```

APPENDIX D: VARIABLE INFORMATION FOR EES MODEL

Variable	Guess	Lower	Upper	Units
Cpa	1.000E+00	-infinity	infinity	kJ/kg-K
Cpv	1.000E+00	-infinity	infinity	kJ/kg-K
Cv	3.000E-05	-infinity	infinity	-
Cv0	6.000E-05	-infinity	infinity	-
d[1]	1.000E-07	-infinity	infinity	m
dddt[1]	-1.000E-08	-infinity	infinity	m/s
DELTA_ml	5.000E-08	-infinity	infinity	kg
DELTA_mv	5.000E-08	-infinity	infinity	kg
DELTA_mw	1.000E-11	-infinity	infinity	kg
di[1]	2.685E-07	-infinity	infinity	m
dmvdt	-1.000E-11	-infinity	infinity	kg/s
dTedt	-1.000E+00	-infinity	infinity	C/s
D_12	2.440E-05	-infinity	infinity	m^2/s
d_check[1]	1.000E-07	-infinity	infinity	m
d_min	1.000E-07	-infinity	infinity	m
exppower[1]	1.000E-05	-infinity	infinity	-
hc[1]	1E+03	-infinity	infinity	W/m^2-K
hm[1]	1E+00	-infinity	infinity	m/s
h_fg[1]	2E+03	-infinity	infinity	kJ/kg
ke	2.660E-02	-infinity	infinity	W/m-K
K_a	2.326E+05	-infinity	infinity	1/m
m1e	1.000E-02	-infinity	infinity	-
m1s[1]	1.000E-02	-infinity	infinity	-
ma	-9.999E+03	-infinity	infinity	kg
ml	5.000E-07	-infinity	infinity	kg
ml0	-9.999E+03	-infinity	infinity	kg
mli[1]	1.000E-09	-infinity	infinity	kg
mv	1.000E-08	-infinity	infinity	kg
mv0	-9.999E+03	-infinity	infinity	kg
mw	5.000E-08	-infinity	infinity	kg
mw0	-9.999E+03	-infinity	infinity	kg
MW_a	2.897E+01	-infinity	infinity	kg/kmol
MW_e	1.000E+00	-infinity	infinity	kg/kmol
MW_w	1.802E+01	-infinity	infinity	kg/kmol
m`	1.000E-10	-infinity	infinity	kg/s
m`i[1]	1.000E-10	-infinity	infinity	kg/s
m``[1]	1.000E-05	-infinity	infinity	kg/m^2-s
m``_check[1]	1.000E-05	-infinity	infinity	kg/m^2-s
m``_max	1.000E-02	-infinity	infinity	kg/m^2-s
Ni[1]	0.000E+00	-infinity	infinity	-
Nuss_d	2.000E+00	-infinity	infinity	-
P	1E+02	-infinity	infinity	kPa
Pa0	9E+01	-infinity	infinity	kPa
phi	1.00000	0.0000E+00	infinity	-
phi_0	1E+00	-infinity	infinity	-
Pv0	2E+00	-infinity	infinity	kPa
Pv_e	1E+00	-infinity	infinity	kPa

Variable	Guess	Lower	Upper	Units
Pv_e0	1E+00	-infinity	infinity	kPa
Pv_s[1]	1E+00	0.0000E+00	infinity	kPa
Pv_s0[1]	1E+00	0.0000E+00	infinity	kPa
Qa[1]	1.0E+00	-infinity	infinity	-
Q_cs	1.0E-01	-infinity	infinity	kW
q_cs[1]	1.0E-01	-infinity	infinity	kW/m^2
q_r[1]	1.0E-01	-infinity	infinity	kW/m^2
Ra	2.870E-01	-infinity	infinity	kJ/kg-K
Re	1.000E+00	-infinity	infinity	kJ/kg-K
rho_e	1.000E+00	-infinity	infinity	kg/m^3
rho_l0	9.982E+02	-infinity	infinity	kg/m^3
rho_l[1]	1.000E+00	-infinity	infinity	kg/m^3
Rw	4.614E-01	-infinity	infinity	kJ/kg-K
Sher_d	2.000E+00	-infinity	infinity	-
step	1.000E-04	0.0000E+00	infinity	s
tau[1]	6.0E+00	0.0000E+00	infinity	-
Te	1.7E+01	-infinity	infinity	C
Te0	2.0E+01	-infinity	infinity	C
time	4.0E+01	-infinity	infinity	s
Ts0	2.0E+01	-infinity	infinity	C
Ts[1]	1.7E+01	-infinity	infinity	C
Twall	-2.0E+01	-infinity	infinity	C
V	1.000E-06	-infinity	infinity	m^3
v%[1]	1.000E+00	-infinity	infinity	-
V0	1.000E-06	-infinity	infinity	m^3
Vi[1]	0.000E+00	-infinity	infinity	m^3
vi%[1]	0.000E+00	-infinity	infinity	-
Vl0	-9.999E+03	-infinity	infinity	m^3
V_l	1.000E-10	-infinity	infinity	m^3
V_li[1]	1.000E-11	-infinity	infinity	m^3
V_v	1.000E-05	-infinity	infinity	m^3
x	-9.999E+03	-infinity	infinity	
y_a	9.900E-01	-infinity	infinity	-
y_v	1.000E-02	-infinity	infinity	-